THESIS

ADVANCED SPECTRAL PROCESSING FOR DUAL POLARIZATION WEATHER RADARS

Submitted by

Amit Dutta

Department of Electrical & Computer Engineering

In partial fulfillment of the requirements

For the Degree of Master of Science

Colorado State University

Fort Collins, Colorado

Summer 2020

Master's Committee:

Advisor: V. Chandrasekar

Margaret Cheney
Thomas Siller

ABSTRACT

ADVANCED SPECTRAL PROCESSING FOR DUAL POLARIZATION WEATHER RADARS

This thesis focuses on the importance of spectral-domain processing and analysis in weather radar applications such as sea-clutter mitigation and the study of rain-hail mixtures in severe storms. An advanced spectral filtering technique has been proposed that helps in obtaining precipitation spectrum thus helping us to filter sea clutter and also carefully study the spectrum of different rain and hail cases in severe storms.

Traditionally, time-domain auto-correlation techniques are used for the estimation of dual-polarization radar moments from the time series data. With the advent of low cost high-speed modern signal processors, frequency-domain processing techniques are feasible to be implemented in real-time. Hence spectral processing can be used for radar moments estimation. Previously, researchers have concluded that spectral filtering has improved the calculation of dual-polarization radar moments. Many algorithms have been implemented in real-time for clutter mitigation and data quality control. In this thesis, various existing frequency and time domain algorithms, such as standard notch filters, Gaussian Model Adaptive Processing (GMAP), and Parametric Time-Domain Method (PTDM) have been used for sea clutter mitigation, and their performances are studied. Spectral Signal Quality Index (SSQI), which is dependent on the auto-correlation spectral density of the signals, has been used to threshold noisy spectrum to obtain a clean precipitation spectrum. Next, using the results from PTDM along with the SSQI thresholding technique, the Polarimetric Spectral Filter for Adaptive Clutter and Noise Suppression [1] has been implemented. The combination of these spectral filtering techniques is regarded as Advanced Spectral Filter (ASF). The algorithms are applied to the observations recorded by the CSU-SEAPOL (Colorado State University - Sea-Going Polarimetric) radar data to identify and filter sea clutter. The ASF has been observed to perform better in terms of sea clutter suppression and identification.

In general, spectral analysis of radar time-series data reveals various characteristics of different hydrometeors. Incorporating Doppler information along with polarimetric measurements in dual-polarization weather radar can unveil various microphysical properties in relation to the dynamics of storms in a radar resolution volume. This study is regarded as Spectral Polarimetry. Spectral analysis has been done on observations that were collected during the RELAMPAGO (Remote Sensing Of Electrification, Lightning, And Mesoscale/Microscale Processes With Adaptive Ground Observations) campaign in Argentina by the CSU-CHIVO (Colorado State University-C-band Hydro-meteorological Instrument for Volumetric Observation) radar. Spectral polarimetry revealed various spectral features such as bi-modal power spectrum, slopes in the spectral differential reflectivity, lowering of co-pol correlation spectrum, etc. from the observations. These features essentially helped to characterize and determine the microphysical properties of different storms. Thus the main goal of this thesis is to show the importance of spectral domain processing and analysis in relation to clutter mitigation and micro-physical study of storms.

ACKNOWLEDGEMENTS

I would like to thank all the members of the CSU RADAR group who helped me during this project. I would like to thank my advisor, Dr. V. Chandrasekar for mentoring me and for his endless support, patience, guidance, and encouragement.

The research on sea clutter analysis is supported by the National Science Foundation. The CSU's SEAPOL radar collected the data during the SPURS 2 campaign. I would like to thank Jim George for providing the data and for his inputs in time series analysis.

I would like to thank my colleague Dr. Ashish Roy who has helped me in spectral processing and the research on advanced spectral analysis. The research on spectral polarimetry is supported by the National Science Foundation and the RELAMPAGO project. The data were collected by the CSU's CHIVO radar. I would like to thank Dr.Francesc Junyent and my colleague Ivan Arias for providing the data to me.

DEDICATION

I would like to dedicate this thesis to my brother (dadabhai), mother (maa) and father (papa).

TABLE OF CONTENTS

LIST OF TABLES

LIST OF FIGURES

Chapter 1

Introduction

1.1 Background and Motivation

Doppler weather radar has been a part of the atmospheric science and remote sensing community for a long time. The operational radars produce primary products such as reflectivity, velocity, and spectral width that are used by the National Weather Services for forecasting purposes. With the advent of dual-polarization, more products like differential reflectivity, differential phase, and co-pol correlation have been added. Special derived products like rainfall rate, specific differential phase, and hydrometer classification have been essential and are used by hydrologists for modeling purposes and by meteorologists for forecasting. In weather radar research, the particle shape, orientation, velocity, and distribution of hydrometeors which are derived from the received radar signals are used to understand the microphysical processes.

Spectral analysis unveils Doppler information of the radar time-series signals, thus giving knowledge about the properties of received echoes from clutter, interference, and precipitation. It also gives us information about the motion and dynamics of a storm event in a radar resolution volume. The characterization of different storm microphysics and the study of their dynamics from the dual-pol Doppler spectra is regarded as spectral polarimetry. Hence there is a necessity to analyze the Doppler spectra of the radar signals. The study of Doppler power spectra has helped researches in various applications. One of the important aspects is clutter mitigation. Siggia et al. [4] have proposed a spectral filtering technique to suppress stationary ground clutter by using a model-based approach. Moisseev et al. [1] proposed an adaptive polarimetric spectral filter that identifies the precipitation and clutter. It creates a mask that helps in retaining only the precipitation spectra, thus filtering out clutter and noise. The other important aspect is the study of microphysical properties of the hydrometeors and dynamics of an event in a particular radar resolution volume, as done by Wang et al. [5] and Pfitzenmaier et al. [6]. Hence the Doppler spectral analysis and polarimetry

help us to carry out the above-mentioned goals. Once all the analysis and filtering are done, the radar moments are to be estimated. Since we are in the Fourier domain, the estimation of radar moments can be done either by going back to the time domain and perform the traditional pulse-pair processing or directly estimate the moments from the dual-pol spectra. The later procedure is known as spectral processing.

1.2 Thesis outline

This thesis addresses the importance of spectral-domain processing and analysis in fast scanning dual-polarization Doppler weather radars. The thesis focuses on two major problems. The first problem is on mitigation of sea clutter by estimating radar moments from the filtered spectra using spectral processing. The second problem involves characterizing intensive convective storms with rain and hail mixtures using spectral polarimetry.

This research consists of the following:

- Algorithm development - A sea clutter filtering technique has been developed here. Firstly, existing time and spectral domain clutter filters like standard notch filter, GMAP (Gaussian Model Adaptive Processing), and PTDM (Parametric Time-Domain Method) for sea clutter mitigation are applied. Next, applying the results from PTDM [7] and Polarimetric Spectral Filter for Adaptive Clutter and Noise Suppression [8] along with the SSQI (Spectral Signal Quality Index) thresholding method, the Advanced Spectral Filter (ASF) has been developed. Radar moments and dual-pol variables using spectral processing are computed, and the performances of the sea clutter mitigation algorithms are evaluated.

- Spectral analysis - General spectral properties of rain from a stratiform storm case have been studied. This is followed by the study of spectral properties of rain and hail mixtures from intense a convective storm case using spectral polarimetry.

Chapter 1 presents the main research idea of the thesis. It discusses the background and motivation of spectral processing and advanced spectral analysis, the problem statement of the thesis, objectives, and the flow of work.

Chapter 2 discusses the basics of polarimetric weather radar, derivation of radar moments from raw radar IQ data using pulse-pair processing and spectral processing.

In Chapter 3, the properties of the CSU-SEAPOL radar are discussed. The chapter focuses on the implementation of existing spectral and time-domain filters, including the standard notch filters, the Gaussian Adaptive Processing algorithm, and the Parametric Time Domain method for sea-clutter mitigation.

In Chapter 4, Spectral Signal Quality Index, which is a new spectral thresholding parameter, has been introduced. Its performance is tested with the co-pol correlation spectrum, which is traditionally used for spectral thresholding. After that, results from PTDM along with the SSQI thresholding method are used in fuzzy classification for the identification of precipitation and clutter spectra. A precipitation mask is generated from the classification, which is used for the estimation of radar moments and dual-pol variables using spectral processing. Finally, the performances of all the spectral filtering algorithms are discussed.

Chapter 5 focuses on the study of various precipitation spectra from both stratiform and convective storms. The main goal is to study and characterize different dual-pol spectra of rain and hail associated with the various micro-physical phenomena that occur in a particular radar resolution volume.

Chapter 6 finally summarizes the entire research work, provides concluding remarks and future scope of the work.

Chapter 2

Dual-polarization Radar time series and signal processing

2.1 Basics of Doppler Weather radar operations and dual polarization radar products

Dual Polarization Doppler weather radars are used to study the orientation, size, shape, distribution, and velocity of the scatterers at a particular radar resolution volume from the echo of transmitted dual-polarized electromagnetic wave. The basic components of a weather radar include the following:

- Transmitter & Receiver - The transmitter generates an output waveform centered or with an offset at the radar's intermediate frequency. It has analog filters that can up-convert the generated signal to RF and then transmit it after amplification. Since these are pulse-Doppler radars, the transmitter aims to produce short-duration high-power pulses of energy. The radar data sets used in this thesis are from the CSU-SEAPOL and the CSU-CHIVO radar, both of which use the RVP900 system. Transmitters are generally solid-state or vacuum tubes. Both the CSU-SEAPOL and CSU-CHIVO uses coaxial magnetron coupled to a solid-state modulator. The receiver detects, amplifies, and demodulates the received RF signals. The RVP900 has a simultaneous transmitter and receiver functionality. The Intermediate Frequency Digital Receiver (IFDR) unit digitizes the received signal into I (In-phase) and Q (Quadrature-phase) samples. The RVP901 IF Digital Receiver (IFDR) which is in the RVP900 architecture has the transmitter, receiver, and the IF detector. Also, for transmission, a pulse compressed waveform is used since a solid-state transmitter has been used in the radars mentioned above.

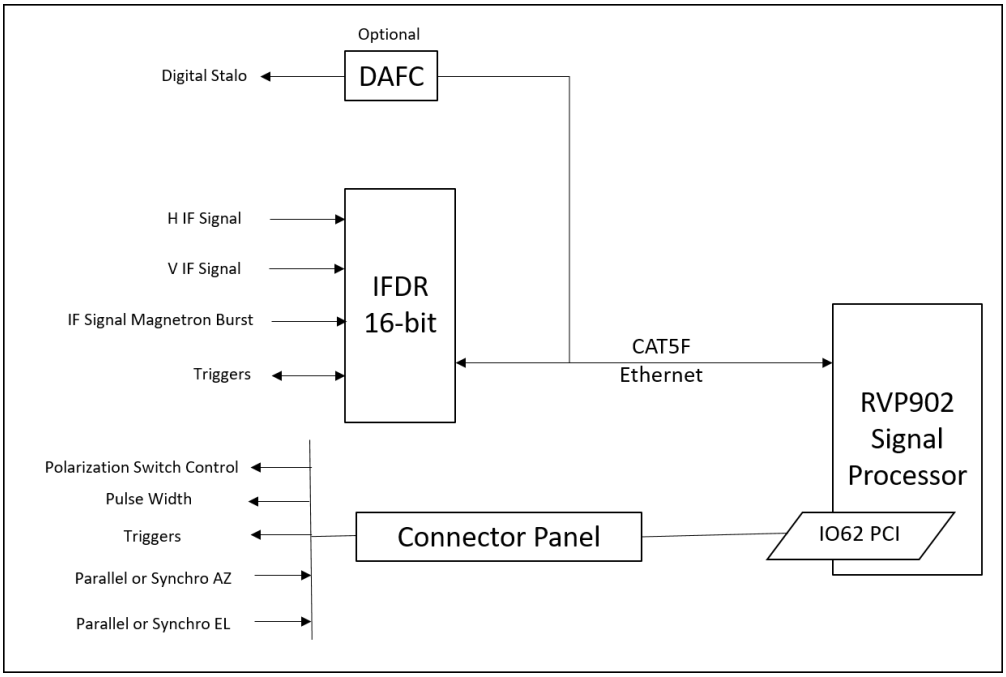

Figure 2.1: Magnetron system for dual-polarization in RVP900 [9].

- Antenna - Generally, a parabolic reflector is used. It acts as a coupling device between free space propagation and waveguides from the transmitter. The antenna system mainly consists of pedestal and reflector, rotatory joints, slip rings, waveguide, feedhorn, dual-polarization system with dual-polarization switch, and finally the antenna control unit, servo motors, and angle detector. The signals generated by the transmitter is fed into the antenna by the feedhorn. The antenna then generates small beams by focusing the transmitted power. It also collects the reflected waves from targets. The feedhorn helps in directing the received wave into the receiver. Data collected by the CSU-SEAPOL radar has been used for the sea clutter mitigation problem. The radar antenna has a gain of 44.5 dBi operating at a range of 5.4 to 5.75 GHz with a symmetric pencil beam of 1° beam-width and -27 dB antenna side-lobe. For the study of different storms using spectral polarimetry, observations from CSU-CHIVO radar have been used. The radar uses a center-fed parabolic type reflector with a gain of 45 dBi, beam-width less than 1°, and side-lobes less than -29 dB.

- Radome - Both the radars mentioned above use quasi-random bee-hive structures made of fiberglass. It is also known as Radar Dome and serves as protection to the antenna from severe weather.

- Signal Processor - A RVP902 Signal Processor is used in the RVP900 architecture. The I and Q data generated by the IFDR is transmitted to the signal processor over a Gigabit Ethernet to produce the final radar products. The signal processor is equipped with clutter filtering ability, auto-correlation computation, clutter micro-suppression, and range averaging, moments computation, speckle filtering, and threshold calculating capabilities.

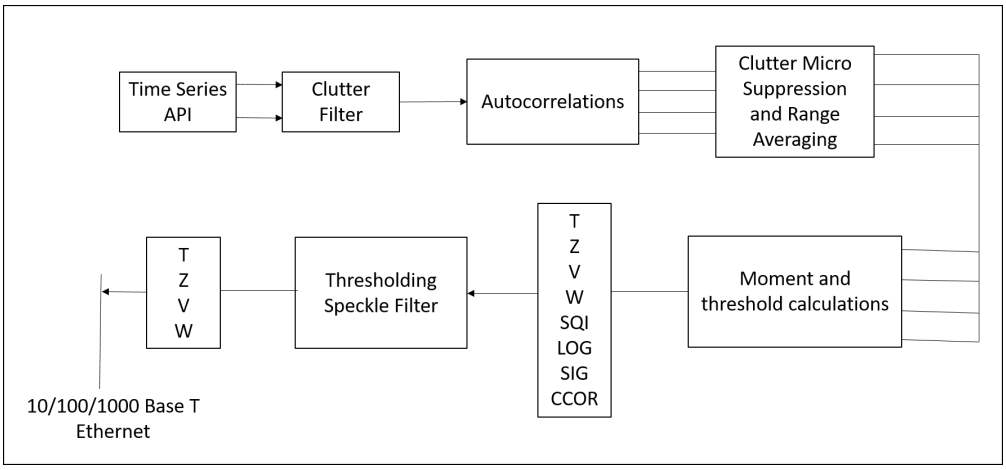

Figure 2.2: Radar moments generation process from the raw IQ data in RVP900 signal processor taken from [9].

After the IQ data is generated, it is fed into the signal processor in which the radar moments are calculated. Typically, a auto-correlation based method for computing radar moments known as pulse-pair processing is used. In pulse-pair processing generally, the IQ data is recorded and saved in digital memory as time-series data from both the horizontal (H) and vertical (V) polarization channels at specific elevation and azimuth angles. The pulse-pair estimation has become standard radar processing algorithms that operate on the time series samples directly in the time domain. It has been shown that the pulse-pair processing provides the least amount of bias and low variance

in the generated radar moments [10] and it approaches the Cramer-Rao lower bound of minimum bias-variance performance as shown by Doviak et al. [11].

The standard pulse-pair processing algorithms from Bringi and Chandrasekar [10] are discussed here. The auto-correlation function at 0^{th} lag from the H-pol raw time-series samples is given as

$$\hat{R}_{0hh} = \frac{1}{N}\sum_{n=1}^{N} H(n)H^*(n) \tag{2.1}$$

where n is the sample index and N is the length of the sequence. At a range gate r km away from the radar and along k^{th} elevation or azimuth depending if the scan mode is RHI or PPI, the $\hat{R}_{0h}$ quantity gives the raw power of the signal.

It is also essential to calculate the auto-correlation functions at 1^{st} and 2^{nd} lags from the H-pol raw time-series samples and are given as

$$\hat{R}_{1hh} = \frac{1}{N+1}\sum_{n=1}^{N} H(n)H^*(n+1) \tag{2.2}$$

$$\hat{R}_{2hh} = \frac{1}{N+2}\sum_{n=1}^{N} H(n)H^*(n+2) \tag{2.3}$$

Also the cross-correlation function at 0^{th} lag is given as

$$\hat{R}_{hh,vv} = \frac{1}{N}\sum_{n=1}^{N} H(n)V^*(n) \tag{2.4}$$

Once all the auto-correlation functions are calculated, now the processor is ready to compute the final moments. The three basic single-polarization moments are Reflectivity, Velocity, and Spectral width. These are known as moments because they are the 0^{th}, 1^{st}, and 2^{nd} order moments of the Doppler power spectrum, respectively.

H-pol Reflectivity of a radar with a radar constant C is given as

$$Z_h = 10 \times log_{10}[\hat{R}_{0hh}] + 20 \times log_{10}(r) + C \tag{2.5}$$

For a radar operating with a wavelength λ and sampling time period T_s which is the Pulse Repetition Time (PRT), the Doppler velocity is derived from the argument or the phase of the 1^{st} lag auto-correlation function and is given by

$$V_h = \frac{\lambda}{4\pi T_s} arg[\hat{R}_{1hh}] \tag{2.6}$$

The spectral width, which is a measure of sheer and turbulence within a particular radar resolution volume, can be computed in two different ways. The R_0, R_1 algorithm which is applicable for $SNR >> 10$ dB is computed as following

$$W_{01} = \sqrt{\frac{2ln[\frac{\hat{R}_{0hh}}{|\hat{R}_{1hh}|}]}{\pi}} \tag{2.7}$$

R_0, R_1, R_2 is the other spectral width algorithm which involves auto-correlation functions at all the 3 lags and is an extension for weak signals with $SNR >> 0...5$ dB and is given by

$$W_{12} = \sqrt{\frac{\frac{2}{3}ln[\frac{\hat{R}_{1hh}}{|\hat{R}_{2hh}|}]}{\pi}} \tag{2.8}$$

The dual-polarization variables are obtained as follows:

Differential Reflectivity which is defined as the difference between the horizontal and vertical reflectivity in dB

$$Z_{dr} = 10 \times log_{10}[\frac{Z_h}{Z_v}] \tag{2.9}$$

The correlation coefficient gives the similarity or the consistency of the return power from both the H and V channels. In general, it compares the phase and power of both channels. If a radar resolution has the same type of particle, then the phase and power changes in both the horizontal

and vertical polarization channels are similar; hence, the co-polar correlation coefficient is higher, i.e. close to 1. It is computed as following

$$\rho_{hv} = \frac{|\hat{R}_{hh,vv}|}{\sqrt{\hat{R}_{0hh}\hat{R}_{0vv}}} \tag{2.10}$$

The differential phase is obtained from the argument of co-polar correlation.

$$\phi_{dp} = arg[\rho_{hv}] \tag{2.11}$$

Another important variable is the Signal Quality Index (SQI), which gives us high values (close to 1) for echoes containing good quantity of signal. This can be both from precipitation or clutter echoes.

$$SQI = \frac{|\hat{R}_{1hh}|}{\hat{R}_{0hh}} \tag{2.12}$$

2.2 Spectral processing for weather radars

2.2.1 Doppler power spectrum estimation

As mentioned earlier, pulse -pair processing produces moments with lower bias and variance, but spectral processing has inherent advantages where the unwanted echoes such as ground clutter, human-made RFI and anomalous echoes can easily be identified, and robust filtering techniques can be implemented to eliminate those. To obtain spectral processing estimates, auto-correlations at different lags and cross-correlation functions must be estimated. The standard spectral processing algorithms that are discussed here are taken from Bringi and Chandrasekar [10] and Moisseev et al. [8]. The auto-correlation function $\hat{R}_{hh}$ at m^{th} lag computed from the length N H-pol time-series samples with n sample index can be expressed as

$$\hat{R}_{hh}(m) = \frac{1}{N}\sum_{n=0}^{N-1} H(n+m)H^*(n) \tag{2.13}$$

Next at a particular range gate r, the Doppler power spectrum is obtained by Discrete Fourier Transform (DFT) of the auto-correlation function and is expressed as

$$\hat{S}_{hh}(r,k) = \sum_{n=-L}^{L} \hat{R}_{hh}(n) e^{\frac{-j2\pi nk}{N}} \tag{2.14}$$

where hh represents horizontal transmission and reception. Here $k = 0, 1, 2, ..., N-1$ are the DFT sample indices and total number of DFT samples is $L \leq N$. Since $\hat{S}_{hh}$ is generated from DFT of auto-correlation hence it is known as auto-spectra. Similarly, the cross-spectra is obtained from the DFT of cross-correlation between the H and V data samples. The cross-correlation spectra is computed as

$$\hat{R}_{hv}(m) = \frac{1}{N} \sum_{n=0}^{N-1} H(n+m) V^*(n) \tag{2.15}$$

The cross spectra is given by,

$$\hat{S}_{hv}(r,k) = \sum_{n=-L}^{L} \hat{R}_{hv}(n) e^{\frac{-j2\pi nk}{N}} \tag{2.16}$$

2.2.2 Range Doppler spectral decomposition of dual-polarization radar parameters

The range-Doppler spectral decomposition of a ray along a particular azimuth (for PPI scans) and elevation (for RHI scans), essentially adds the Doppler information to the ray. A ray is generated by pulse-par processing done over all the pulses. Adding the Doppler information helps us study the precipitation signal and clutter properties and draw conclusions about the micro-physical process taking place in the resolution volumes. The study of dual-polarization spectral properties and characterizing the micro-physics of various events is also regarded as Spectral Polarimetry. The spectral decomposition of reflectivity spectrum $S(Z_h)$ is obtained from the power spectrum as the following

$$S(Z_h(r,k)) = 10 \times log_{10}[\hat{S}_{hh}(r,k)] + 20 \times log_{10}(r) + C \tag{2.17}$$

Spectral decomposition of Differential Reflectivity is given by

$$S(Z_{dr}(r,k)) = \frac{\hat{S}_{hh}(r,k)}{\hat{S}_{vv}(r,k)} \tag{2.18}$$

Spectral decomposition of Co-pol Correlation is given by

$$S(\rho_{hv}(r,k)) = \frac{|\hat{S}_{hv}(r,k)|}{\sqrt{\hat{S}_{hh}(r,k)\hat{S}_{vv}(r,k)}} \tag{2.19}$$

and the spectral decomposition of Differential Phase is obtained as

$$S(\phi_{dp}(r,k)) = arg[\rho_{hv}(r,k)] \tag{2.20}$$

2.2.3 Retrieval of Dual-polarization moments from Doppler power spectrum

After the generation of the dual-polarization spectral parameters, various filtering algorithms are implemented to remove different clutters, various interferences, unwanted artifacts, and suppress noise in the spectral domain. Next, the radars moments and dual-polarization variables are obtained back from the power spectral densities. The basic three radar moments which are reflectivity ($\hat{Z}_h$) , Doppler velocity ($\hat{v}$) and spectral width ($\hat{\sigma}^2$) are obtained as follows

$$\hat{Z}_h(r) = 10 \times log_{10}[\sum_{k=0}^{N-1} \hat{S}_{hh}(r,k)] + 20 \times log_{10}(r) + C \tag{2.21}$$

$$\hat{v}(r) = \frac{\sum_{k=0}^{N-1} v_k \hat{S}_{hh}(r,k)}{\sum_{k=0}^{N-1} \hat{S}_{hh}(r,k)} \tag{2.22}$$

$$\hat{\sigma}^2(r) = \frac{\sum_{k=0}^{N-1}[v_k - \hat{v}(r)]^2 \hat{S}_{hh}(r,k)}{\sum_{k=0}^{N-1} \hat{S}_{hh}(r.k)} \tag{2.23}$$

The other polarimetric variables like differential reflectivity ($\hat{Z}_{dr}$), copolar correlation coefficient ($\hat{\rho}_{hv}$) and the differential phase ($\hat{\phi}_{dp}$), are obtained as:

$$\hat{Z}_{dr}(r) = 10 \times log_{10}[\frac{\sum_{k=0}^{N-1} \hat{S}_{hh}(r,k)}{\sum_{k=0}^{N-1} \hat{S}_{vv}(r,k)}] \tag{2.24}$$

$$\hat{\rho}_{hv}(r) = \frac{\sum_{k=0}^{N-1} |\hat{S}_{hv}(r,k)|}{\sqrt{\sum_{k=0}^{N-1} \hat{S}_{hh}(r,k) \sum_{k=0}^{N-1} \hat{S}_{vv}(r,k)}} \tag{2.25}$$

$$\hat{\phi}_{dp}(r) = arg[\sum_{k=0}^{N-1} \hat{S}_{hv}(r,k)] \tag{2.26}$$

The spectral decomposition of the dual-polarization parameters play an important role in clutter and precipitation identification. It helps in designing different spectral filters for clutter mitigation and noise suppression. It also helps in identifying different precipitation features and how it varies along the range. Overall, spectral decomposition gives us a magnified view of a ray in a PPI or RHI scan.

Chapter 3

Sea clutter mitigation using time and spectral domain processing

This chapter presents an overview of time and spectral processing techniques for sea clutter mitigation. Spectral processing is essentially an estimation problem that firstly involves spectral estimation followed by moments estimation, which is governed by some underlying equations. Spectral processing is an already established work, and the equations are taken from [10], [8]. This chapter investigates the performance of different existing algorithms in the context of sea clutter mitigation.

3.1 Introduction

Clutter mitigation is a challenging task in the area of weather radar signal processing. When clutter echoes are present in radar observations, it produces highly biased estimates in radar moments such as reflectivity, Doppler velocity, and spectral width. For weather radars, nonmeteorological targets are the source of clutter echoes, whereas the meteorological targets are the signals of interest. Echoes from stationary targets often found close to the radar are known as ground clutter. They comprise high rise buildings, tall structures, and trees. Similarly unwanted echoes from the sea or ocean surface appear as sea clutter on weather radar observations. In this chapter, we investigate various techniques for mitigation of sea clutter in operational weather radars. In the next section, the origin and characteristics of sea clutter, along with its existing mitigation methods, have been discussed.

3.2 Sea clutter

A brief explanation of sea clutter characteristics and its origin has been discussed here. Sea clutter can be seen in marine radars that are usually installed on ships or near the coast. When a

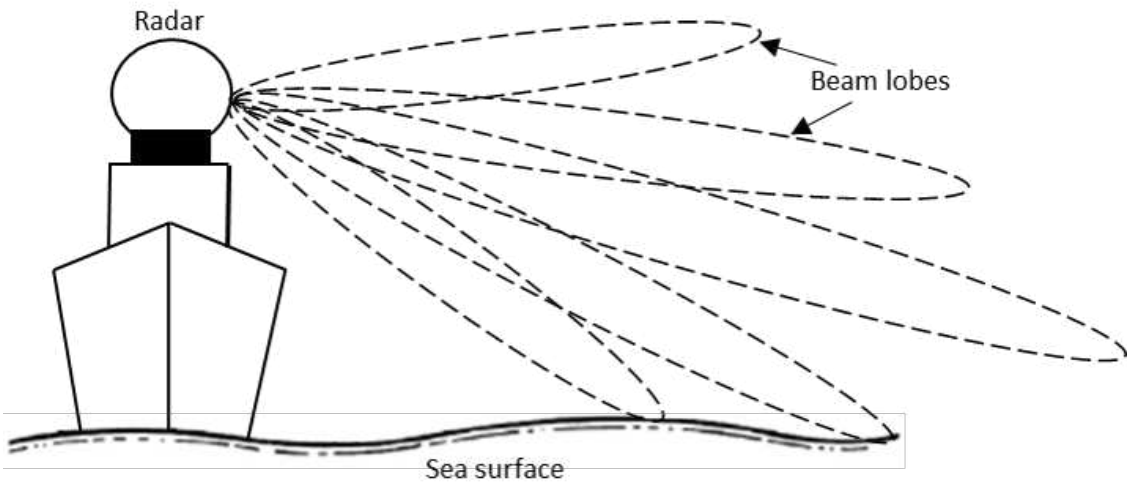

Figure 3.1: The figure shows source of sea clutter in a shipborne radar adapted from [12].

radar scans at low elevations, the echoes from the sea surface appear as sea clutter in the observations. Turbulent conditions in the ocean can cause high waves, which can also appear in radar scans as sea clutter. Fig. 3.1 shows how a shipborne radar scans at low elevations and observes the echoes returned from the sea surface. It has been established by Skolnik [13] that sea clutter properties are impacted by polarization state, radar frequency, and look angle of radar relative to the direction of the wind, grazing angle, sea state, wave velocities, and types of surface waves present.

Various researchers have modeled sea clutter using different distributions like K, log-normal, and Weibull distributions. Sea clutter has both Gaussian and non-Gaussian processes involved. According to Watts et al. [14], the small-scale waves having a large number of scattering centers that decorrelate very fast, also known as speckles, follow Gaussian distribution. The large scale waves that modulate the speckles, also known as texture, can be explained by Gamma distribution. The sea clutter can be represented as a product of a gamma process and a Gaussian/Rayleigh process. The K distributed sea clutter model has been successful in describing its non-Gaussian characteristics [15]. Sometimes the radar resolution may not be high enough to resolve the small-scale structure of the sea surface. In that case, a Compound Gaussian (CG) model proposed by Haykin et al. [16] is used to describe the sea clutter characteristics, assuming that the speckle only stays for

few milliseconds while the textures remain for a longer time. Thus sea clutter mainly originates due to two processes- speckle and texture [17]. Ward et al. [15], [18] and Walker et al. [19], [20] have explained origin and characteristics of sea clutter through electromagnetic scattering and mathematical modeling [14].

Sea clutter present in weather observations may lead to wrong decisions by forecasters and meteorologists. There could be substantial data loss if the clutter affected range bins are ignored; hence different time and spectral domain filtering techniques have been developed for sea clutter mitigation. Chanthavong et al. [21] used a fuzzy logic approach for sea clutter identification and used spatial interpolation techniques for sea clutter suppression. Hannesen et al. [22] proposed a probability-based fuzzy logic approach to identify sea clutter using textures of reflectivity, differential reflectivity, differential phase, and co-pol correlation and used standard Doppler filter to mitigate sea clutter from the identified range bins. In this chapter, we focus on applying existing real-time clutters filters like the standard notch and the Gaussian Model Adaptive Processing (GMAP) filter [4] which were originally developed for ground clutter mitigation have been implemented here to check their performances in the context of sea clutter mitigation. Parametric Time-Domain Method (PTDM) [7], a renowned time-domain filter that simultaneously identifies signal and clutter spectral parameters, has also been adapted for the sea clutter mitigation problem. Time-series data collected by the CSU-SEAPOL radar has been used for filter performance evaluation.

3.3 The CSU SEAPOL radar

The sea going polarimetric radar or the Seapol has been a part of NASA's SPURS-2 (Salinity Processes in the Upper-ocean Regional Study) campaign in the year 2016. The campaign took place in the Eastern Tropical Pacific region. The Seapol is a C-band radar which has been designed to operate at 5.65 GHz. The radar uses a pulse width of $0.4 - 2\mu s$ and works with both uniform and dual Pulse Repeating Frequency (PRF) in the range 300-1800 Hz.

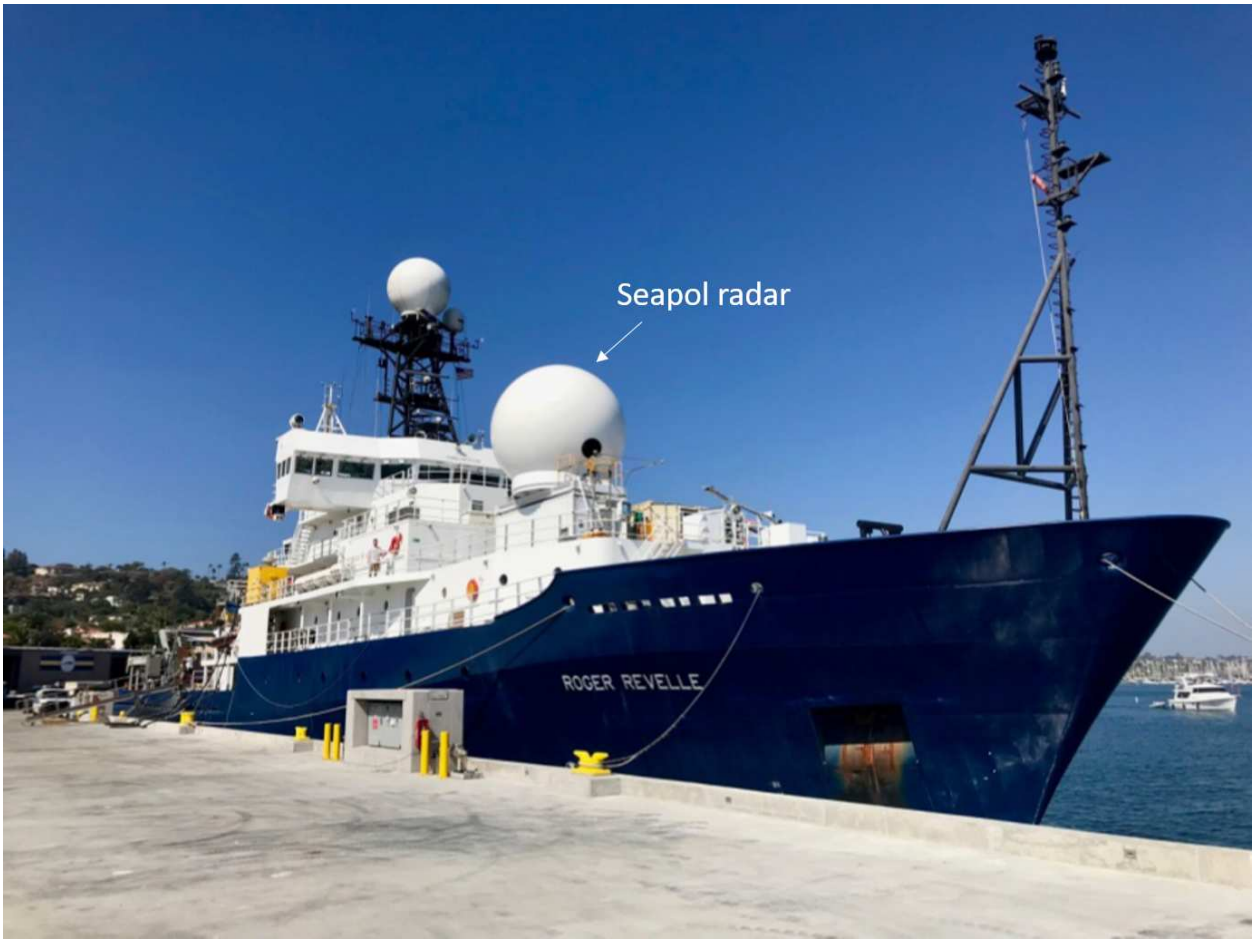

Figure 3.2: The CSU Sea-Pol mounted on the R/V Revelle. The radar is placed on the forward 02 deck of the ship [23].

The Seapol radar is equipped with both Horizontal and Vertical Polarization channels. The mode of operation used during the campaign was simultaneous-transmit, simultaneous-receive (STSR) mode. George et al. [23] have mentioned a comprehensive description of the radar hardware and signal processing used in the Seapol radar. Before the deployment in the sea, the Seapol radar was calibrated using the CSU-CHILL radar. Fig. 3.2 shows the radar onboard the Global-class research vessel in the US research fleet, R/V Revelle. The radar can scan in both azimuth and elevation with a maximum range of 120 km and a range resolution of 100 m. The radar only does a sector sweep of 240-degree when operating in PPI mode. Rutledge et al. [24] have documented the goals and motivation of the SPURS2 campaign, as well as the deployment of SEAPOL radar.

3.3.1 Data collection, observations and data interpretation

The data were recorded in the eastern Pacific Ocean, where different precipitation events were captured over the sea surface. Radar reflectivity (Z) and velocity (V) along with various dual-polarization moments such as differential reflectivity (Z_{dr}), differential phase (ϕ_{DP}) and co-pol correlation (ρ_{HV}) were processed from the time series data. Fig. 3.3 and Fig. 3.4 shows the dual-polarization radar products for a particular event containing weather and sea-clutter. The main aim is to identify sea clutter in the presence of precipitation, study its characteristics in both time and spectral domain, and provide clutter mitigation solutions. Ryzhkov et al. [25] proposed a fuzzy logic approach for discriminating sea clutter and precipitation using textures of differential phase and signal power. Moisseev et al. [1] showed that it is possible to identify ground clutter mixed with precipitation using textures of spectral differential reflectivity and spectral differential phase. In this paper, co-pol correlation, textures of differential phase, and differential reflectivity are used for classification. Spectral decomposition of Z, Z_{DR}, ϕ_{DP}, and ρ_{HV} along a particular azimuth are computed. The range-azimuth spectrographs helped in observing the characteristics of both precipitation and sea clutter echoes.

Fig.3.3a and 3.3b show the reflectivity and differential reflectivity respectively from the data collected from a precipitation event on 9th November 2017 over the East Pacific ocean. The observations show stratiform echoes with mixtures of heavy and light rain. Various dual-polarization moments are also shown here. The Z field shows that the region is having a mixture of moderate to heavy rain. The Z_{DR} field shows the occurrence of a mixture of large and small drops. The larger drops contribute to the high positive value reaching a maximum value of around 2 dB. However, the smaller drops are almost circular and hence contribute to lower values close to almost zero. There is a possible beam blockage from 205° to 215° azimuth. As seen in the PPI scan plot, some appreciable amount of precipitation is seen from 40 Km to 90 Km range. Fluctuations of the parameters seen in the first 15 km range show the possibility of sea clutter. After 15 km appreciable amount of precipitation is observed. The co-pol correlation (ρ_{HV}) field in Fig. 3.4b shows the outline of the precipitation event. The regions with values of ρ_{HV} very close to 1 shows the uniform

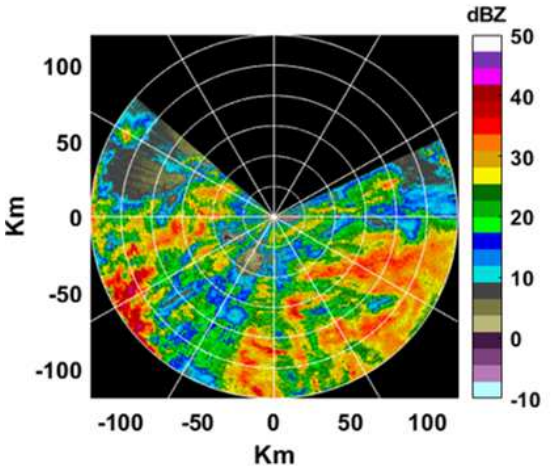

(a) Reflectivity

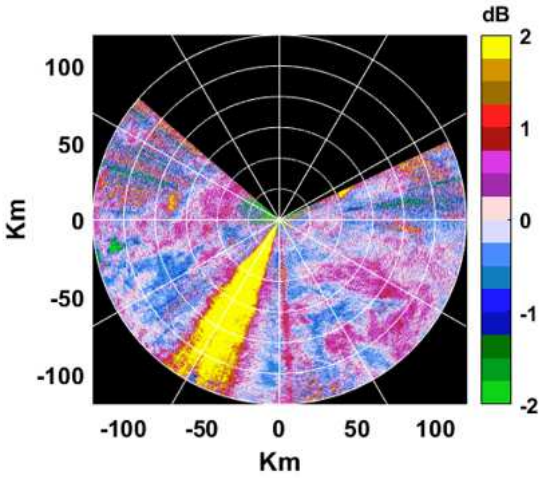

(b) Differential reflectivity

Figure 3.3: PPI plots of reflectivity (Z) and differential reflectivity (Z_{DR}) from 9^{th} November 2017 data recorded at 19:30:00 UTC at $0.5°$ elevation.

size and shape distribution of hydrometeors, whereas the regions with a value slightly less than 1 show more hydrometeor diversity.

The Fig.3.4a and 3.4b shows the differential phase and co-pol correlation fields receptively. It can be seen that the ρ_{HV} is constant and almost equal to 1 throughout the range bins corresponding to precipitation. In the first 15 km, there is a high variation of the parameters, which is due to the presence of sea clutter. The differential phase (ϕ_{DP}) is seen to propagate along the range bins containing precipitation from 15km to 70km. Also, there are minimal fluctuations in the

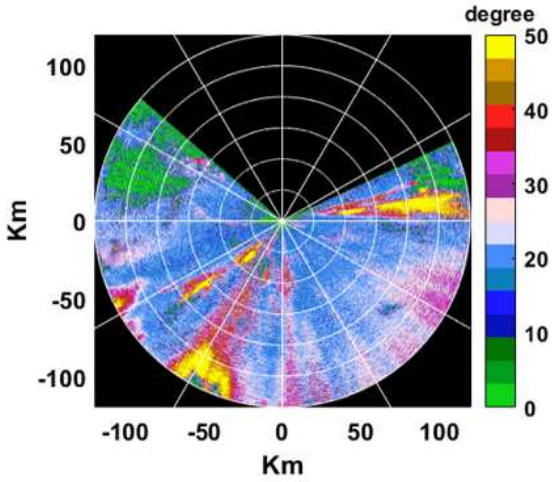

(a) Differential Phase

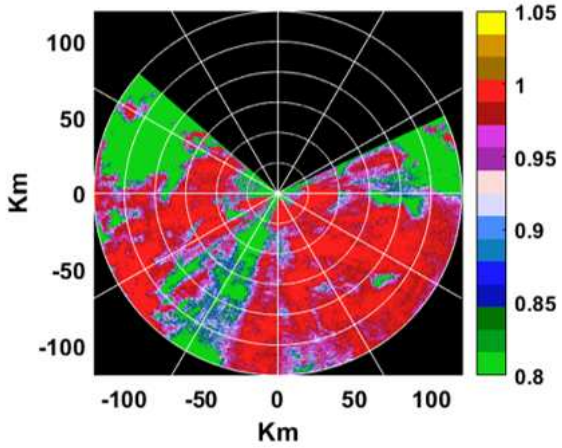

(b) Co-pol Correlation

Figure 3.4: PPI plots of Differential Phase (ϕ_{DP}) and Co-pol Correlation (ρ_{HV}) from 9^{th} November 2017 data recorded at 19:30:00 UTC at 0.5° elevation.

ϕ_{DP} values; i.e., it is stable throughout the regions where there is very high ρ_{HV}. This follows the properties of the dual-polarization parameters. All the fields shown are without applying any thresholds. Generally, these thresholds are done based on inputs from the Co-pol correlation and signal quality index field. The threshold level for co-pol correlation is taken to be around 0.8-0.9 and 0.1 -0.3 for the SQI field. Since the range gates containing both precipitation and clutter may have low co-pol correlation, such thresholding has not been applied to ensure that none of the precipitation data is removed due to thresholding. Sea clutter is generally observed within 30 km range from radar. If such a threshold is applied, then data in the first 30 km range will be lost.

To correctly identify sea clutter, it is essential to have the entire data set of precipitation in the presence of noise and clutter.

3.4 Performance evaluation for sea clutter mitigation algorithms

For the evaluation of the sea clutter filter, the following methodology has been adopted.

- Reflectivity of the original scan, $Z_{unfiltered}$, which has sea clutter contaminated data and reflectivity field after clutter filtering, $Z_{filtered}$ is considered. In general, the residue field contains sea clutter, but due to error in clutter filtering, which occurs when some precipitation data is also filtered, this error in precipitation is also present in the residue field along with other contamination. The residue field can be expressed as

$$Z_{residue} = Z_{unfiltered} - Z_{filtered} \tag{3.1}$$

  Now the residue mostly contains how much sea clutter has been suppressed. Ideally, this residue is an estimate of sea clutter. Hence $Z_{residue}$ is considered as the estimated sea clutter. Since we do not have a sea clutter map, this is considered as an approximation to the sea clutter. Theoretically, the filtered precipitation field will contain values from precipitation only. Since a ground truth is not available; thus, $Z_{filtered}$ is considered as the estimated signal. All the quantities - $Z_{residue}$, $Z_{unfiltered}$ and $Z_{filtered}$ are in dB scale. Taking anti-log on both the sides in Eq. 3.1, the residue field is a ratio between unfiltered and filtered in the linear scale. Hence we can now define a Clutter Suppression Ratio (CSR) metric in the dB scale as the following

$$CSR = Z_{residue} \tag{3.2}$$

- The residue field also provides information about the range bins that the filter has identified as sea clutter and has performed mitigation. Clutter identification performance is measured

by estimating the empirical Receiver Operating Characteristic (ROC) curves which are dependent on the probability of false alarm (P_{FA}) and the probability of detection (P_D), defined as follows

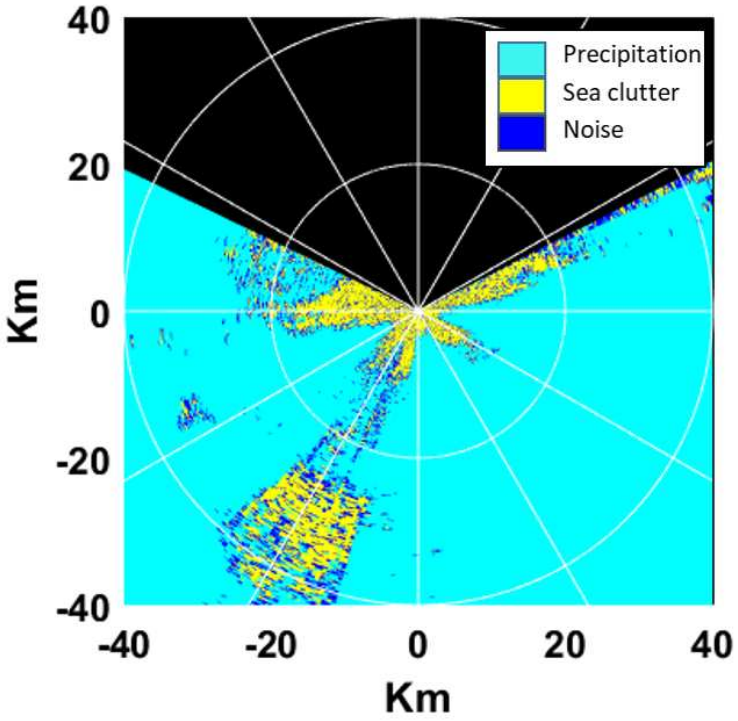

Figure 3.5: Fuzzy logic classification output is shown based on the PPI scan at 0.5° elevation recorded during 9^{th} Nov. 2017 at 19:30:00 UTC. This is set as the sea clutter map for comparing the performances of sea clutter filters.

$$P_{FA} = \frac{N_{FF}}{N_F} \tag{3.3}$$

$$P_D = \frac{N_{DD}}{N_D} \tag{3.4}$$

In Eq. 3.3, N_{FF} is the number of range bins that are falsely detected as sea clutter, and N_F is the total number of non-clutter bins. Similarly, in eq. 3.4, N_{DD} is the number of range bins that are correctly identified as sea clutter. The bins in the $Z_{residue}$ field that are not zero,

which fall in the clutter flagged bins in the clutter map, are the bins correctly identified as sea clutter. N_D is the total number of sea clutter bins.

For this generally, a clutter map is fixed based on which the variables in Eq. 3.3 and 3.4 are computed. However, since a fixed sea clutter map cannot be obtained due to its random nature hence a clutter map has been constructed from the scan under consideration using fuzzy logic inferences based on [25] and [26]. Fig. 3.5 shows the sea clutter map generated after using fuzzy logic. This classification is done on the PPI scan data. This clutter map, along with the clutter residues, has been used for computing the variables in Eq. 3.3 and 3.4.

3.5 Sea clutter mitigation using existing time and spectral processing algorithms

In this chapter, different spectral-domain filtering techniques are implemented, and their performances are analyzed. The various filtering methods discussed in this chapter are listed below:

1. Notch Filter
2. Gaussian model adaptive processing (GMAP)
3. Parametric Time Domain Method (PTDM) Filter

In many operational radars, a notch filter is used for ground clutter mitigation, a classical filtering technique. This filter has been used in real-time radar systems for a few decades. The advantage of this technique is that the clutter suppression in entirely in the designer's hand; thus, the clutter suppression level and clutter notch width can be programmed. GMAP uses a Gaussian clutter model to remove clutter around the zero Doppler velocity. It is a spectral domain approach initially used for ground clutter suppression. GMAP works only in the range bins where clutter to signal ratio is appreciably high. The other advantage of this technique is that in the case where the clutter and precipitation spectrum overlap, it uses a Gaussian weather model to interpolate over the clutter removed Doppler bins. In this way, the original weather spectrum is approximately

retained. Next, the Parametric Time Domain Method (PTDM) method is used to estimate the spectral parameters of the clutter and precipitation signals. A log-likelihood function that consists of the covariance matrix parameterized by the spectral parameters is minimized to derive the final precipitation and clutter spectral parameters' values. PTDM helps in simultaneously finding the mean power, spectral width, and Doppler velocity of the spectrum. Once this is found, it is possible to separate precipitation and sea clutter spectra. Next, going back to the time domain, the moments are calculated by pulse-pair processing.

3.5.1 Filtering with Notch Filter used in WSR-88D

In this section, a zero Doppler notch filter is implemented to check its performance in the sea clutter mitigation problem. This filtering methodology has been used in the WSR-88D weather radar systems for ground clutter mitigation. It uses 5^{th} order elliptic filters with three different suppression levels: low, medium, and high. The general transfer function for the filter is expressed as following.

$$H_(z) = \frac{b_0 + b_1 z^{-1} + b_2 z^{-1} + b_3 z^{-1} + b_4 z^{-1} + b_5 z^{-1}}{a_0 + a_1 z^{-1} + a_2 z^{-1} + a_3 z^{-1} + a_4 z^{-1} + a_5 z^{-1}} \tag{3.5}$$

the co-efficient a_i's and b_i's are obtained from [27]. Although the users can control the filter suppression at the same time, the filter length may increase. More the filter length more will be the filter coefficients; hence it will require more memory blocks.

Fig.3.6 shows the frequency responses of the notch filters designed for mitigating sea clutter. The sampling frequency of the SEAPOL radar is 1.2 kHz. Therefore the Nyquist frequency or the f_{max} in the figure is 600 Hz. The stopband of the filter is 0-25 Hz. The passband is 50-600 Hz, and it provides a 40-60 dB suppression. Now, this filter is implemented on the 9^{th} November data. The azimuth profile at 268.4° is chosen for observing the filter performance. Since sea clutter depends on the sea surface condition, hence the clutter spectrum may or may not appear around the zero Doppler, unlike ground clutter. This is also a reason why a fixed clutter map cannot be used for sea clutter mitigation.

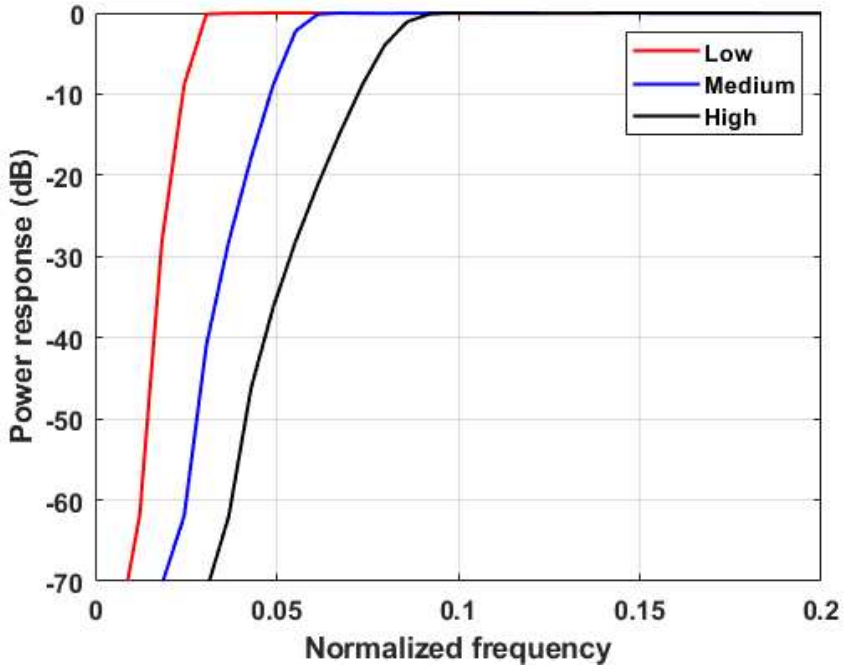

Figure 3.6: Frequency responses of low, medium, and high suppression level notch filter shown in red, blue and black respectively.

Table 3.1: Selection of suppression levels of notch filter

$\hat{\sigma_{ts}}$ range	suppression level	Notch width provided
$(0-1.8]$	Low	2.36
$(1.8-2.54]$	Medium	3.12
$(2.54-6]$	High	5.06

Since the notch filter is centered at zero frequency or zero Doppler, hence a wider notch width filter can filter the clutter spectrum occurring close to zero Doppler. The disadvantage here is that this can filter out relevant signals as well. A fixed clutter map is used for ground clutter filtering case. The ground clutter is stationary and does not change significantly from scan to scan; hence the fixed clutter map is convenient. The notch filter only filters the range bins included within the map. But since the nature of sea clutter changes from scan to scan hence a fixed clutter map cannot be constructed for all the scans. Therefore we construct a clutter map for every individual scan

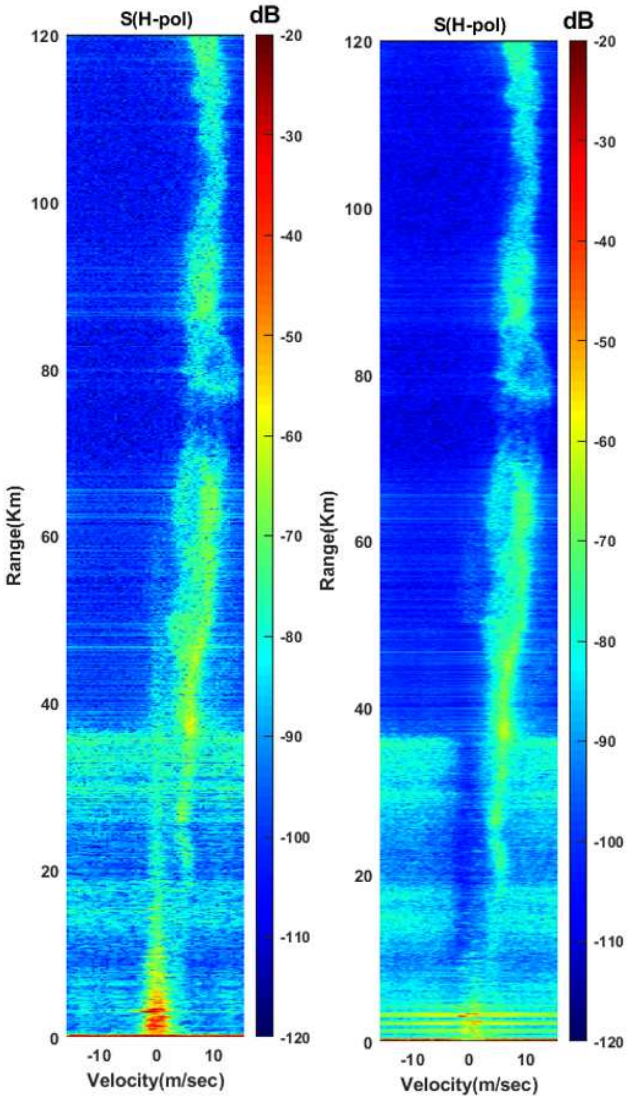

Figure 3.7: Original range-Doppler spectrograph containing sea clutter and precipitation is shown in (A). Notch filtered spectrograph is shown in (B). The spectrographs are computed along 268° azimuth based on the 9^{th} Nov. 2017 recorded at 19:30:00 UTC data.

as described in 3.4. The notch filter is applied based on the range bins identified as sea clutter, as shown in Fig.3.5.

From Fig. 3.7a it can be seen that the sea clutter spectrum has a wide spectral width in the range between 15-20 km and tapers to a much narrower spectrum after 20 km. Therefore the 'High' suppression notch filter has been used in the first 20 km, whereas a 'Medium' suppression level has been used after 20km. Fig. 3.8a and Fig. 3.8b show original and filtered spectra located

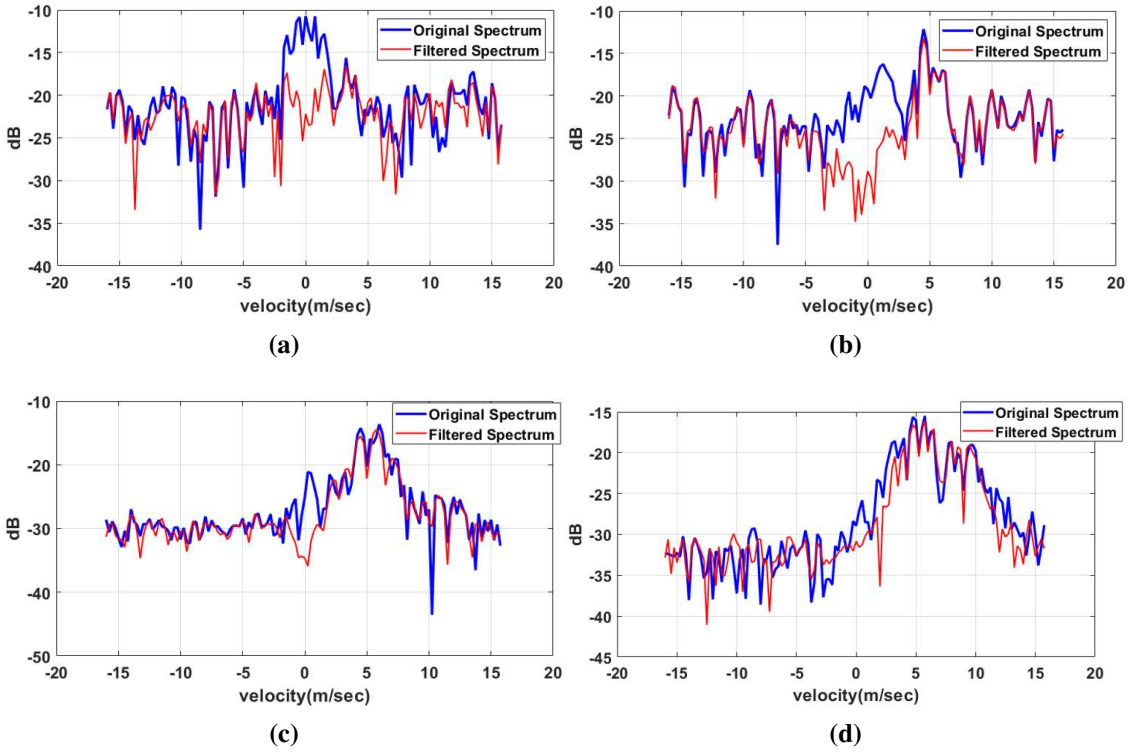

Figure 3.8: Notch filter output applied on the time-series data along 268° azimuth from the 9^{th} Nov. 2017 recorded at 19:30:00 UTC data set. Original (blue) and notch filtered (red) spectrums are shown. (A) and (B) correspond to the spectrums at 6.5 km and 19 km respectively while (C) and (D) correspond to spectrums at 40.5 km and 50 km respectively..

at 6.5 km and 19 km respectively along 286° azimuth using 'High' suppression level. Fig. 3.8c and Fig. 3.8d show original and filtered spectra located at 40.5 km and 50 km, respectively, using 'Medium' clutter suppression level. Fig. 3.9b shows the filtered PPI field obtained after using the notch filter at the range bins, which are identified as sea clutter in the clutter map. Fig. 3.9c shows the residue of the Reflectivity field Z_h after implementing the notch filter.

Fig. 3.9c shows the residue after clutter suppression. Ideally, this field shows the estimated sea clutter, but the error in estimating precipitation and other contamination is also present here. Comparing the residue fields with the clutter map, we see that the notch filter has removed appreciable amount of sea clutter from the clutter flagged range bins. As seen from Fig.3.10 the filter notches out quite a good amount of sea clutter. The 'High' suppression level uses higher stopband edge frequency. Consequently, it provides suppression over a larger velocity range; thus, the notch

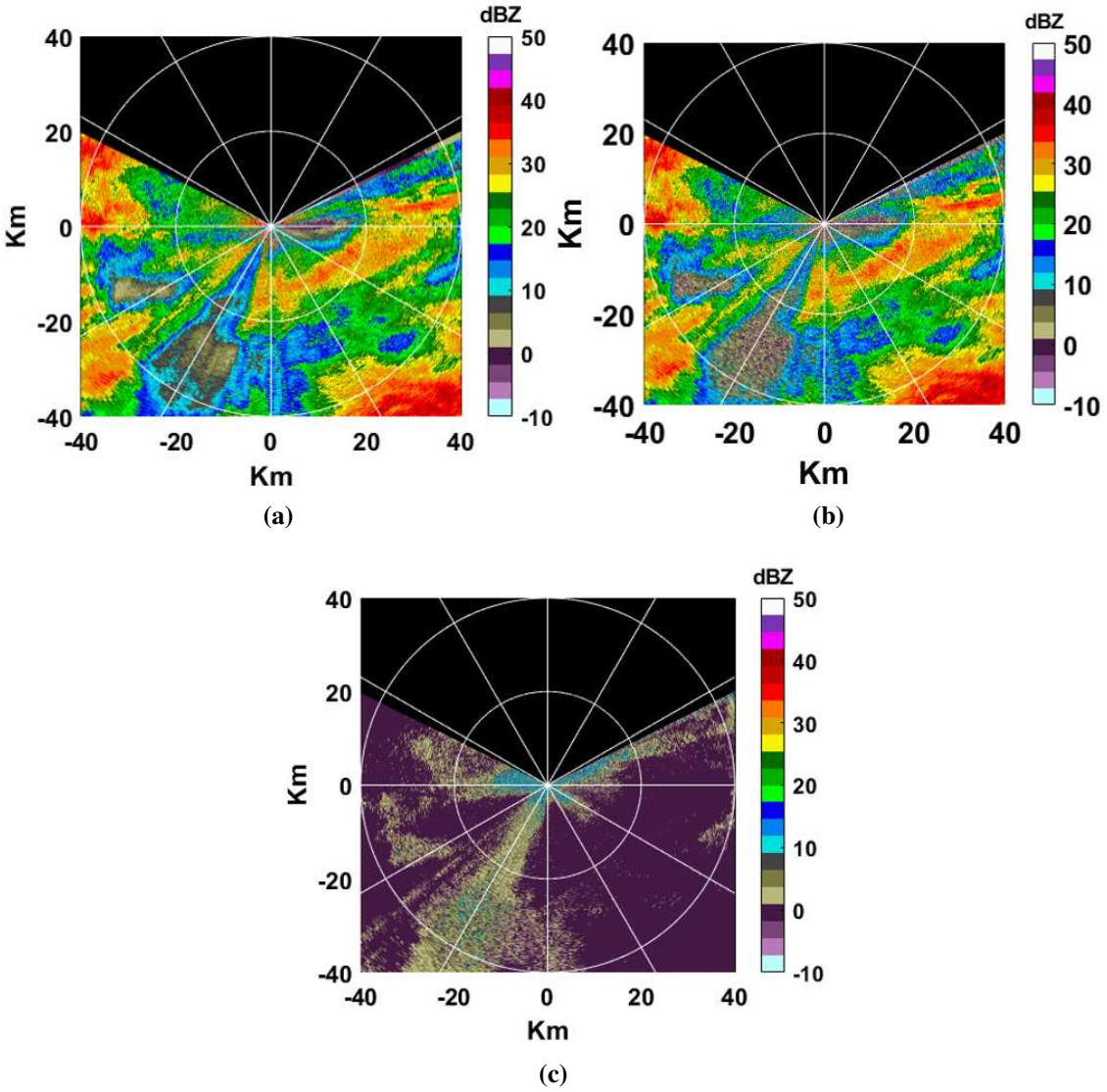

Figure 3.9: Sea clutter filtered PPI Reflectivity field computed by spectral processing is shown in (B) using the notch filter. The original unfiltered reflectivity field is shown (A). The residue field is shown in (C). The data is recorded during 9^{th} November 2017 at 19:30:00 UTC at 0.5° elevation.

width that it provides is larger, helping in removing the clutter that occurs close to the zero Doppler. The suppression level provided is around 20-30 dB. Fig. 3.10a shows the histogram of CSR. The occurrence of $CSR = 0$ is the highest because it represents the regions where $Z_{original} = Z_{filtered}$ and since it covers most of the PPI scan, hence its probability of occurrence is more. The other values in the histogram correspond to the clutter suppression provided by the notch filter. The maximum suppression provided is 24.7 dB.

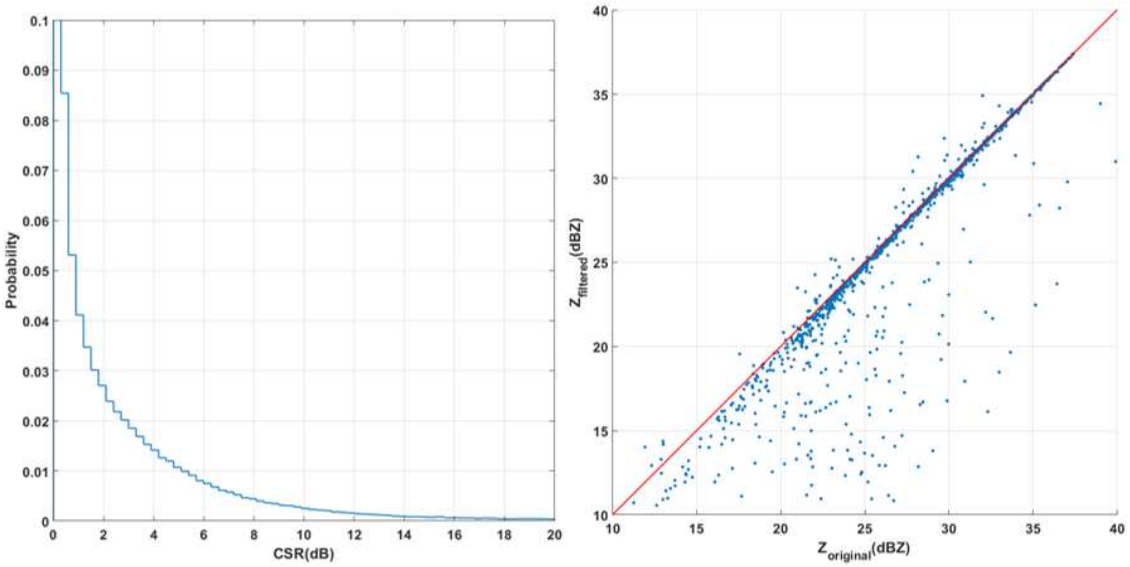

Figure 3.10: Clutter suppression ratio distribution is shown in (A). The comparison between $Z_{original}$ and $Z_{filtered}$ is shown in the scatter plot in (B) for standard notch filter.

Fig. 3.10b shows the scatter plot between the filtered and original reflectivity field. The red line corresponds to the one to one correspondence where both the field have equal values, i.e., these points represent the regions where the filter was not applied.

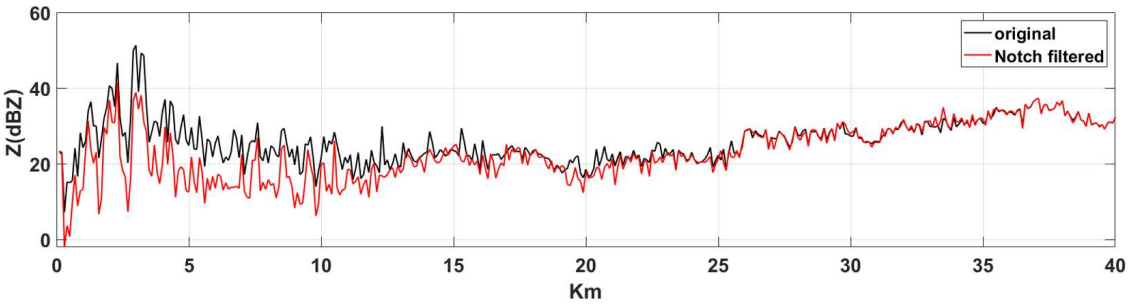

Figure 3.11: Original reflectivity profile (black) and notch filtered profile (red) are shown along the range at 268°.

Hence these are regions free from sea clutter and contain either precipitation, noise, or other contaminations. The points below the one to one line correspond to the regions where the notch filter has been applied. Since after filtering, the overall calculated reflectivity is lower than the original reflectivity; hence they occur below the line. There are range gates where the calculated

reflectivity is higher than the original field after the filter is applied. These points occur above the one to one correspondence line, as shown in the figure. Fig. 3.11 shows the original (black) and filtered (red) reflectivity range profile along the 268° azimuth. The filtered profile shows some amount of suppression provided by the notch filter. The main drawback is that if there is an overlap between weather and sea clutter spectra, then the notch filter suppresses the weather spectra around zero Doppler. Hence it creates an additional bias in these cases.

3.5.2 Filtering using GMAP

The GMAP filtering was initially developed for ground clutter using adaptive techniques. The main advantage is that it is only applied to the range gates with high clutter to signal ratio, i.e., at the locations where clutter is present. Also, when there is overlap between weather and clutter, it uses the Gaussian model of weather to retrieve weather spectra in the Doppler bins from which data was removed due to the presence of clutter. Hence, GMAP can be successfully used to overcome a few of the drawbacks posed by the notch filter. The algorithm is actively running in many operational radar systems. The RVP-900 processors in the Vaisala radars use GMAP as the principle algorithm for ground clutter filtering. According to Raynal et al. [28], sea clutter has a Gaussian spectrum and occurs at zero or near-zero Doppler velocity, hence GMAP can be used to mitigate the sea clutter. In cases where sea clutter occurs at non-zero Doppler velocity, the notch cannot be applied at the zero velocity Doppler bin, as it will give unexpected results for clutter suppression. In such cases, a wider notch is applied to eliminate the Doppler bins containing sea clutter.

The existing GMAP algorithm may still work with the use of increased clutter spectral width. Increasing the clutter spectral width will help in removing more non zero Doppler spectral points. Hence when sea clutter is present at non-zero Doppler velocity bins, the increased clutter spectral width may remove the clutter points and interpolate through them. However, this might not be applicable if the sea clutter spectrum is at a significantly higher non-zero Doppler velocity. Fig. 3.12a and 3.12b shows original and the filtered range-Doppler spectrograph after using GMAP respectively. Due to interpolation, as seen in Fig.3.12b, the sea clutter has been suppressed, but

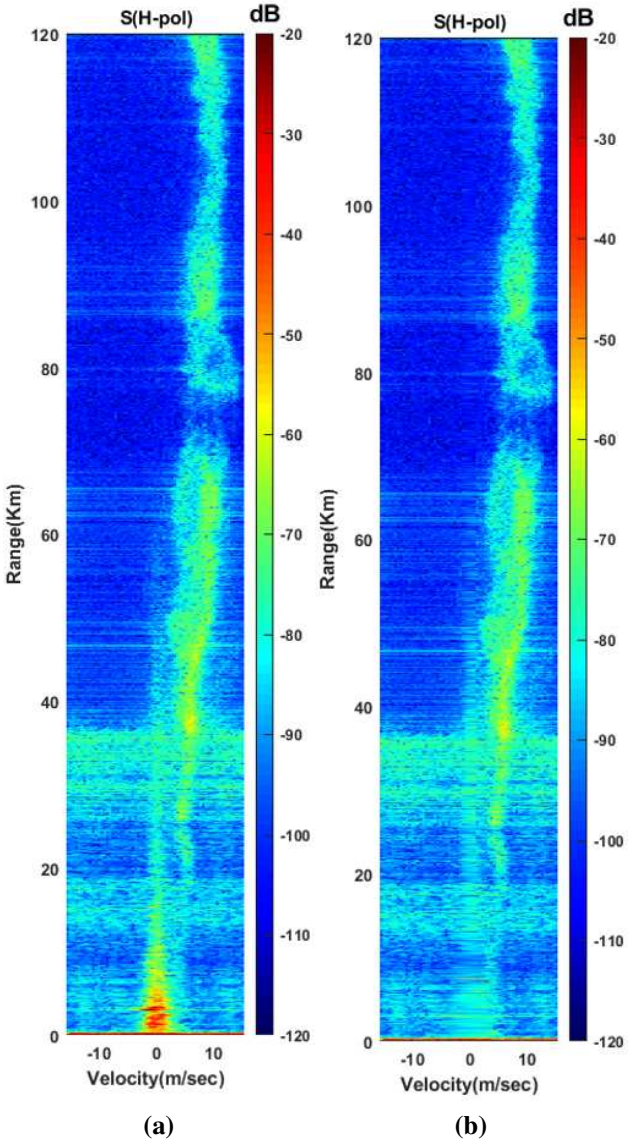

Figure 3.12: Original unfiltered spectrograph is shown in (A) and the GMAP filtered spectrograph used on 268.4° showed in (B) from the 9^{th} November 2017 data at 0.5° elevation.

the effect of interpolation is seen in the filtered spectrograph. Fig.3.13a shows the result of GMAP filter applied at the 5 km range bin containing sea clutter along 268.4° azimuth. Fig. 3.13b shows the GMAP filter applied on the spectrum at the 35 km range bin containing both sea clutter and precipitation. Although this solution has achieved the original aim, it cannot be regarded as an optimum solution. The main advantage of using GMAP is that the filter is applied only to the clutter spectrum or in cases where overlapping of weather and clutter spectrum is present.

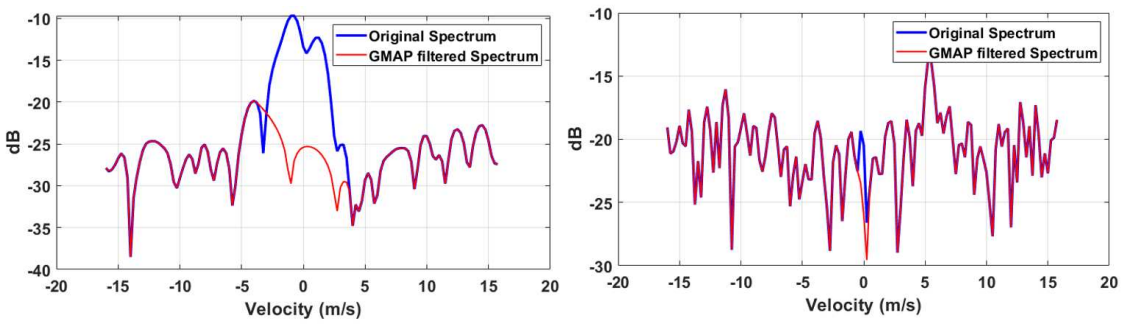

Figure 3.13: Spectra at 5 km (A) and 35 km (B) along 268.4° azimuth is shown here. The original spectrum is shown in blue. The filtered spectrum after using GMAP is shown in red. The spectra are computed from from the 9^{th} November 2017 data at 0.5° elevation.

Fig. 3.14b shows the filtered PPI field obtained after using the GMAP filter. Fig. 3.14c shows the residue of the Reflectivity field Z_h after implementing GMAP filter.

Fig. 3.14c shows the residue or the clutter suppression field. Theoretically, this represents the estimated sea clutter field, but in this case, it also contains errors in estimated precipitation and other contamination.

Comparing the residue fields with the clutter map, we see that the GMAP filter has taken out an appreciable quantity of sea clutter. As seen from Fig.3.13, the filter provides a good amount of clutter suppression. GMAP also takes out the sea clutter that occurs close to the zero Doppler velocity. The suppression level provided is around 20-30 dB. Fig. 3.15a shows the histogram of CSR. The occurrence of $CSR = 0$ is the highest because it represents the regions where $Z_{original} = Z_{filtered}$ and as it covers most of the PPI scan; hence its probability of occurrence is higher. The other values in the histogram correspond to the clutter suppression provided by the GMAP filter. The maximum suppression provided is 28 dB. Fig. 3.15b shows the scatter plot between the filtered and original reflectivity field. The red line corresponds to the one to one correspondence where both the fields have equal values, i.e., these points represent the regions where no filter has been used. These regions are free of sea clutter containing either precipitation or noise. The points below the one to one line correspond to the regions where the GMAP filter has been applied. Since after filtering, the overall calculated reflectivity is lower than the original reflectivity; hence they

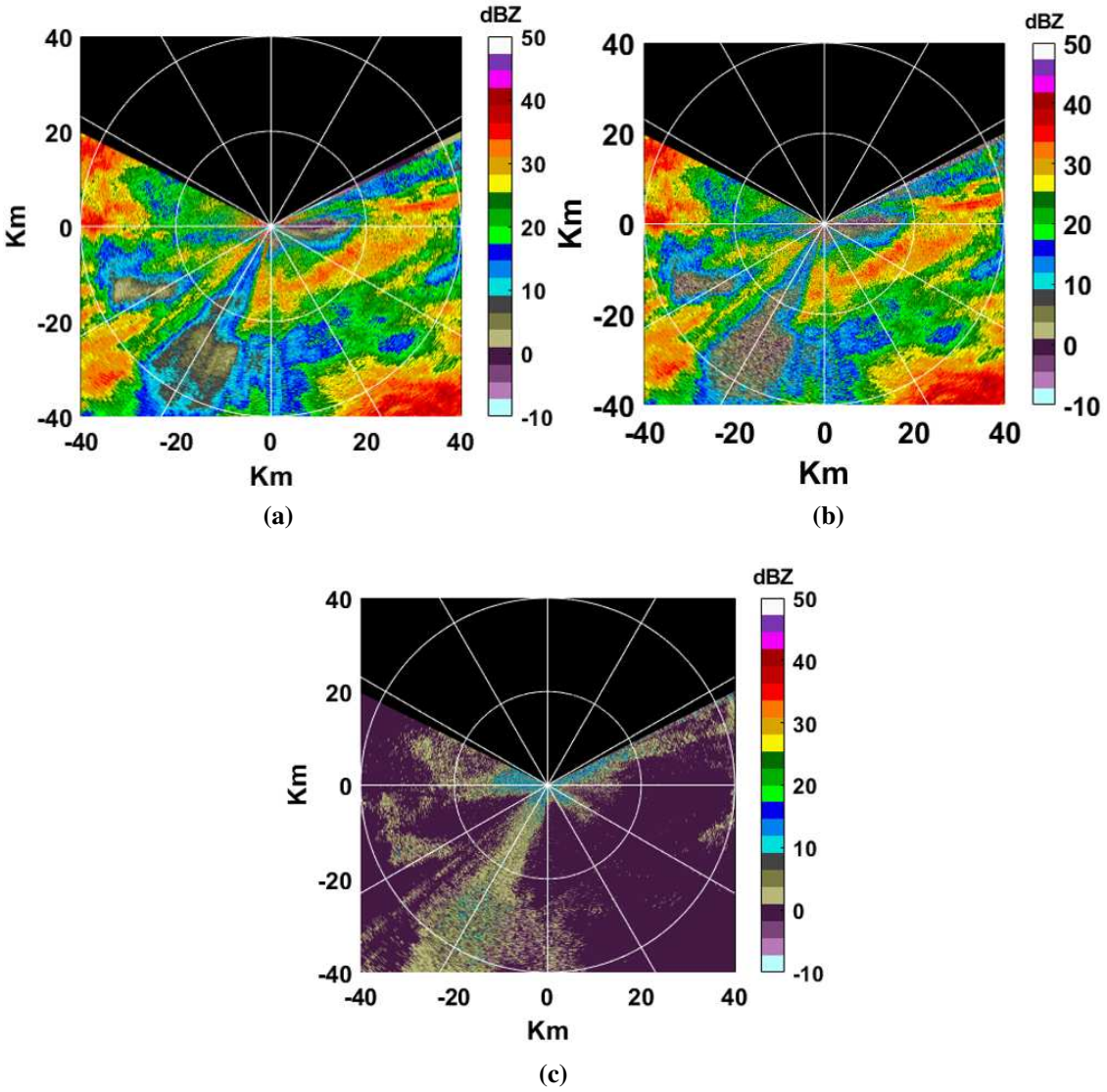

Figure 3.14: Clutter filtered PPI field using GMAP is shown in (B). The residue or the amount of clutter suppressed with other contamination in the field is shown (C) from the 9^{th} November 2017 data at $0.5°$ elevation. The original reflectivity field with both sea clutter and precipitation is shown in (A)

occur below the line. There are range gates where the estimated reflectivity is biased after the filter is applied due to errors in filtering. These points have a higher reflectivity than the original field and thus occur above the one to one correspondence line, as shown in the figure. Fig. 3.16 shows the original (black) and filtered (red) reflectivity range profiles along the $268°$ azimuth. The suppression provided by the GMAP filter is observed here.The main disadvantage of using GMAP

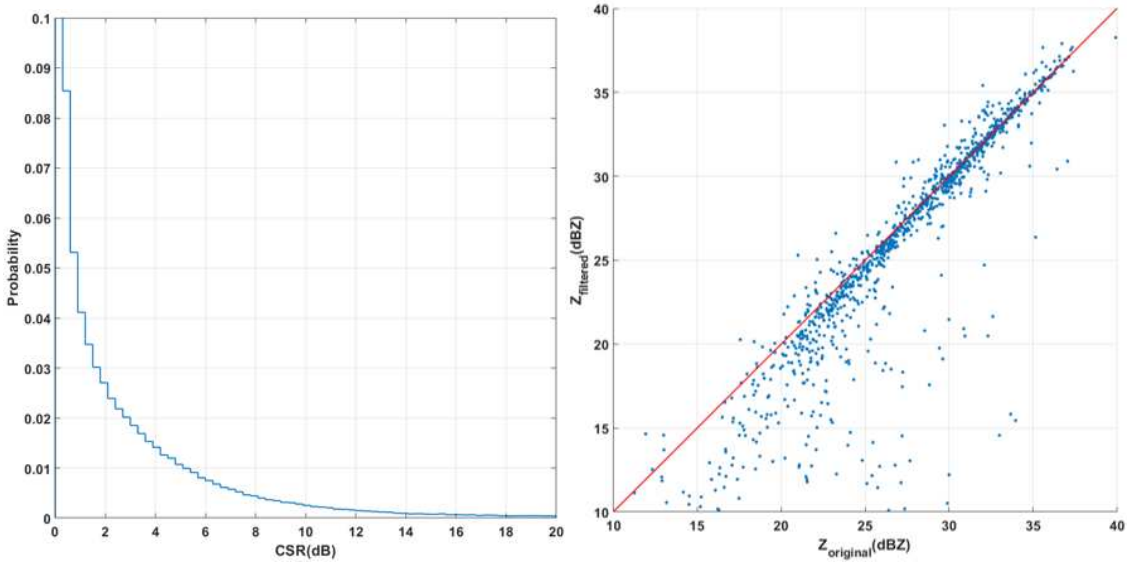

Figure 3.15: Clutter suppression ratio distribution is shown in (A). The comparison between $Z_{original}$ and $Z_{filtered}$ is shown in the scatter plot in (B) for GMAP.

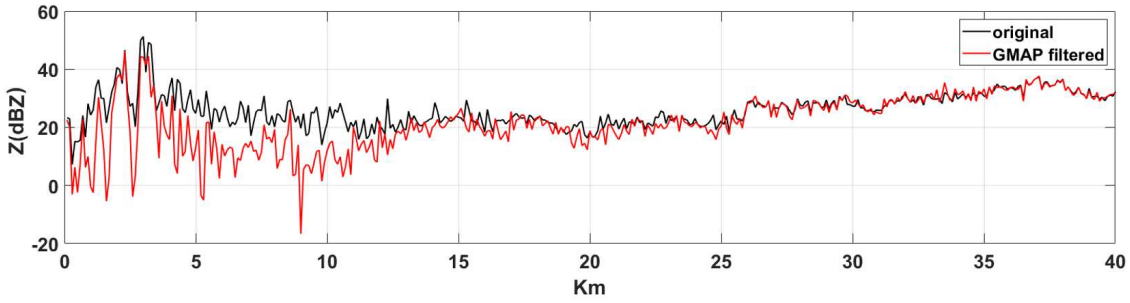

Figure 3.16: Original reflectivity profile (black) and GMAP filtered profile (red) are shown along the range at 268°

is that, due to incorrect computation of CSR or errors in interpolation the resulting reflectivity can be biased.

3.5.3 Parametric Time Domain Method (PTDM) filtering

Nguyen et al. [7] have proposed a Parametric Time Domain Method (PTDM) for clutter mitigation and precipitation signal estimation for dual-polarization weather radars. The PTDM algorithm simultaneously estimates stationary clutter and precipitation signal properties. The advantage of this algorithm is that it helps in accurately estimating the spectral moments of precipitation signals

in the presence of clutter. It is a minimum likelihood estimation problem that estimates the total power, mean Doppler velocity, and spectral width of the echoes. Here it is used for determining the properties of precipitation and sea clutter signals. PTDM sets an initial guess of the properties of the signal, clutter, and noise floor, which is followed by a more refined estimation using the minimum likelihood estimation problem. Here the properties of the signals are estimated using pulse pair estimates as initial feed to a log-likelihood optimization function. Next, the presence of two echoes are tested using two different parameters, and accordingly, the algorithm progresses. If there are two echoes, a new likelihood optimization function is solved to separate the two echoes' properties. Here it is assumed that the signals have an initial power level difference of 10dB.

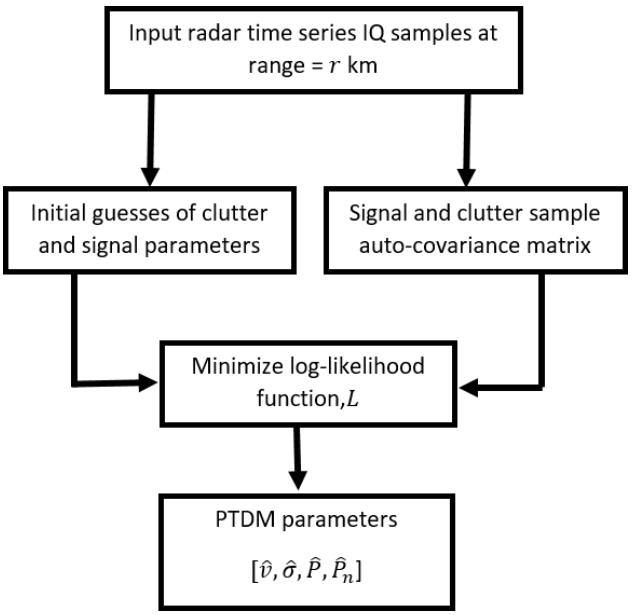

Figure 3.17: Flow chart showing the Parametric Time Domain Model algorithm for estimating spectral parameters by [7]

The motivation for using this filtering method in case of sea clutter mitigation is that PTDM can simultaneously separate two different echoes present in a signal. Since the sea clutter may not be present at the zero Doppler; hence, it can be treated as a second signal echo in the presence of a general precipitation signal echo. Here a general precipitation signal is one with a Gaussian spectrum and unimodal i.e., having only a single peak. Hence, the original PTDM algorithm can

be used as a 2 echo estimation problem where we skip the stationary clutter property estimation and directly estimate the signal properties followed by the 2 echo test. In this way, if the sea clutter is present, then PTDM performs 2 echo test and separates both precipitation and sea clutter echoes. Thus, even if the sea clutter spectra is present at zero or non-zero Doppler velocity, in both cases, the algorithm will treat it as one of the two echoes. The algorithm has been described in the flow chart, as shown in Fig.3.18. The procedure for estimating the signal spectral parameter estimation is described in detail below.

- *Step 1* : Estimation of signal sample co variance matrices.

$$\hat{R}_{sx} = \frac{1}{r_s} \sum_{n=1}^{r_s} h_{ts}^n h_{ts}^{n\,T} \tag{3.6}$$

  where h_{ts} is the H-pol time series signal. In this case the SEAPOL data has $m = 64$ sample data length. h_{ts}^n has length m_1 and $r_s = \lfloor \frac{m-m_1}{d_1} + 1 \rfloor$ where $\lfloor . \rfloor$ is the floor function. $\hat{R}_{sx} \in \mathbb{C}^{m_1}$ is the averaged signal co variance matrix. d_1 is the lag applied for covariance matrix computation from the time series signal.

- *Step 2*: Estimate system noise and guess initial signal power and noise floor.

$$\hat{P}_s = \frac{1}{m} \sum_{k=1}^{m} |h_{ts}(k)|^2 \tag{3.7}$$

  where $\hat{P}_s$ is the total signal power

  Next, we estimate the Doppler power spectral density of the time-series signal.

$$P_{psd}(k) = \frac{1}{m} \sum_{n=0}^{2L-1} W(n) \Big[\sum_{z=0}^{m-n-1} h_{ts}(z+n) h_{ts}^*(z) \Big] e^{(\frac{-j2\pi nk}{m})} \tag{3.8}$$

  where P_{psd} is the signal power spectral density. W is the windowing function that is used to smooth the spectrum and reduce spectral leakage. The signal autocorrelation function is presented within $\big[. \big]$. The minimum power of P_{psd} is considered to be the estimated noise-

floor denoted by $\hat{P_{sys}}$. The system noise is determined by power spectral density arranged in ascending order and taking the mean of first 25% of the arranged spectrum and is denoted by P_n.

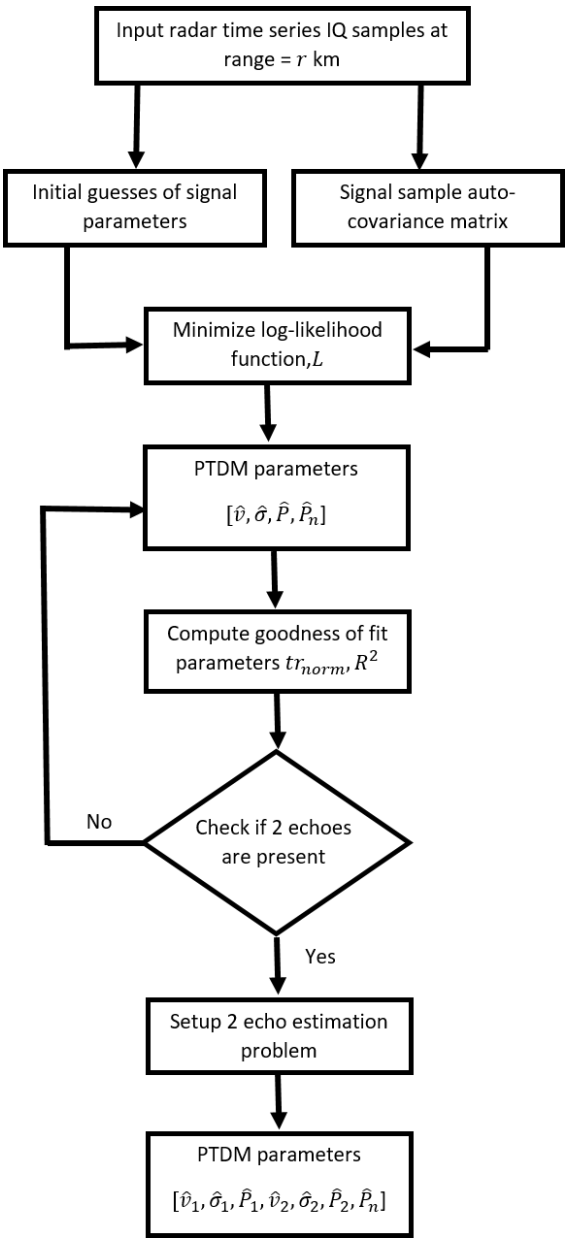

Figure 3.18: Flow chart showing the Parametric Time Domain Model algorithm for estimating spectral parameters of sea clutter and precipitation by [7]

- *Step 3*: Use MLE to find an accurate signal estimate.

According to [10] the complex radar voltage at the receiver follows a multivariate probability density function given by

$$f(X) = \frac{1}{\pi^N |R_x|} exp(-X^H R_x^{-1} X) = \frac{1}{\pi^N |R_x|} exp(-tr(R_x^{-1} \hat{R}_x)) \tag{3.9}$$

where X is the vector of the received signal samples: $R_x = E(XX^H)$ is the covariance matrix and $\hat{R}_x$ is the sample covariance matrix. The $|.|$ is the determinant operator. The covariance matrix depends on several parameters that follow the assumption that the Doppler spectrum of clutter and precipitation has Gaussian shape.

The covariance matrix is parameterized by the signal parameters and is denoted as $R_x(\mu)$. Using Eq.3.9 the negative log-likelihood function can be expressed as

$$L(\mu) = log(|R_x(\mu)|) + tr\left[R_x^{-1}(\mu)\hat{R}_x\right] \tag{3.10}$$

where μ is the unknown parameter vector and $tr(.)$ is the trace operator. $\hat{\mu}$ is obtained by solving the minimization problem

$$\hat{\mu} = \arg\min_x(L(\mu)) \tag{3.11}$$

For signal estimation $\hat{R}_x = \hat{R}_{sx}$. The final parameter vector after solving the MLE is set as the following

$$\hat{\mu} = [\hat{v}, \hat{\sigma}, \hat{P}, \hat{P_n}] \tag{3.12}$$

- *Step 4* : Test for 2 echoes

  Next we compute the ***R-squared*** and the *normalized trace* parameters. These two parameters measure the wellness of the fit by the PTDM algorithm and are a test for the presence of 2

Table 3.2: Signal echo classification using goodness of fit parameters

	$tr_{norm} < 0.7$	$0.7 < tr_{norm} < 1.4$	$tr_{norm} > 1.4$
$R^2 > 0.9$	2 echoes-fit both	bad fit	bad fit
$R^2 > 0.9$	1 echo-good fit	2 echoes- fit stronger echo	2 echoes-fit stronger echo

echoes. Nguyen et al. [7] have termed this as *goodness of fit* parameters. The normalized trace is computed as the trace of the product matrix between the sample covariance matrix and the model covariance matrix and can be expressed as

$$tr_{norm} = tr[R^{-1}(\hat{\mu})\hat{R}_x] \tag{3.13}$$

The R^2 is the measure of the fraction of the variance that the model can explain as is expressed as the following

$$R^2 = 1 - \frac{\sum_{k=1}^{m} |Im[R_{\hat{\mu}}(k,1)] - Im[R(\hat{k},1)]|^2}{\frac{1}{m}\sum_{k=1}^{m} |Im[\hat{R}(k,1)] - \langle Im[R(\hat{k},1)]\rangle|^2} \tag{3.14}$$

where m is the number of lags.

The goodness of fit parameters is used to determine the presence of 2 echoes in signals. Table 3.2 shows the values of the goodness of fit parameters to infer the number of echoes from the signal.

- *Step 5* : If 2 echoes are inferred, then signal parameters are initialized, and the MLE is solved to determine the individual parameters of the 2 echoes present in the signal. Hence in the final parameter vector

$$\hat{\mu} = [\hat{v_1}, \hat{\sigma_1}, \hat{P}_1, \hat{v_2}, \hat{\sigma_2}, \hat{P}_2, \hat{P}_n] \tag{3.15}$$

where $\hat{v_1}, \hat{\sigma_1}, \hat{P_1}$ are echo 1 precipitation parameters and $\hat{v_2}, \hat{\sigma_2}, \hat{P_2}$ are echo 2 clutter parameters.

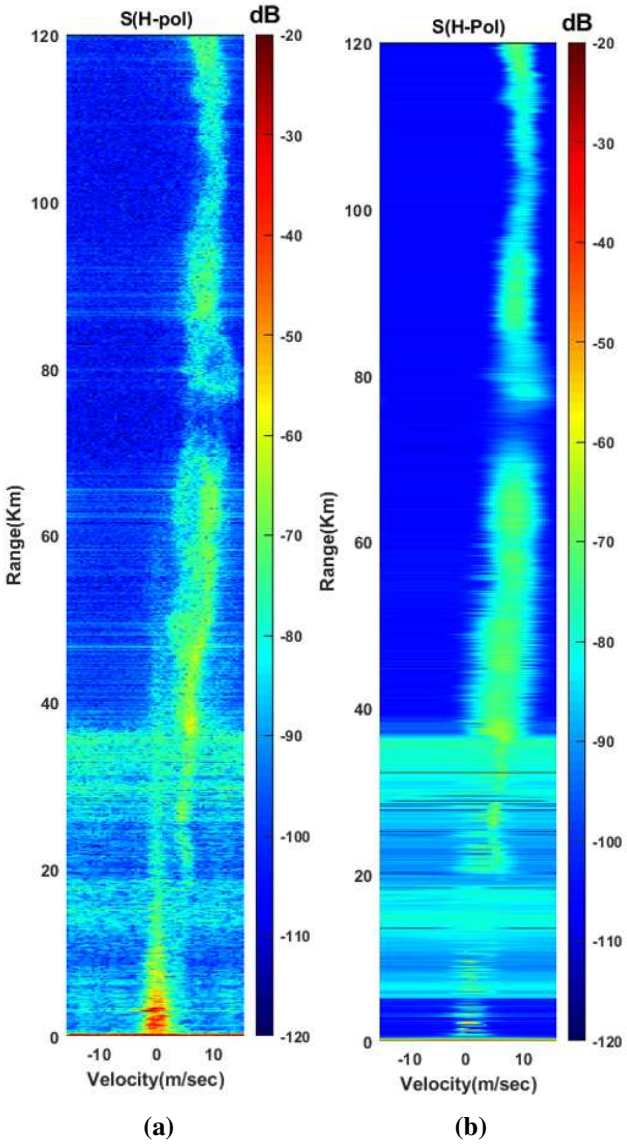

(a) **(b)**

Figure 3.19: Original spectrograph is shown in (A) and the spectrograph of precipitation saperated from sea clutter using PTDM shown in (B) computed along 268.4° azimuth from the 9^{th} November 2017 data

Fig.3.19b shows the Range-Doppler spectrograph of the estimated power spectral density of precipitation after using PTDM. As seen from Fig.3.19a, which shows the Range-Doppler spectrograph of original power spectral density, the noise floor in the first 40 km is significantly higher

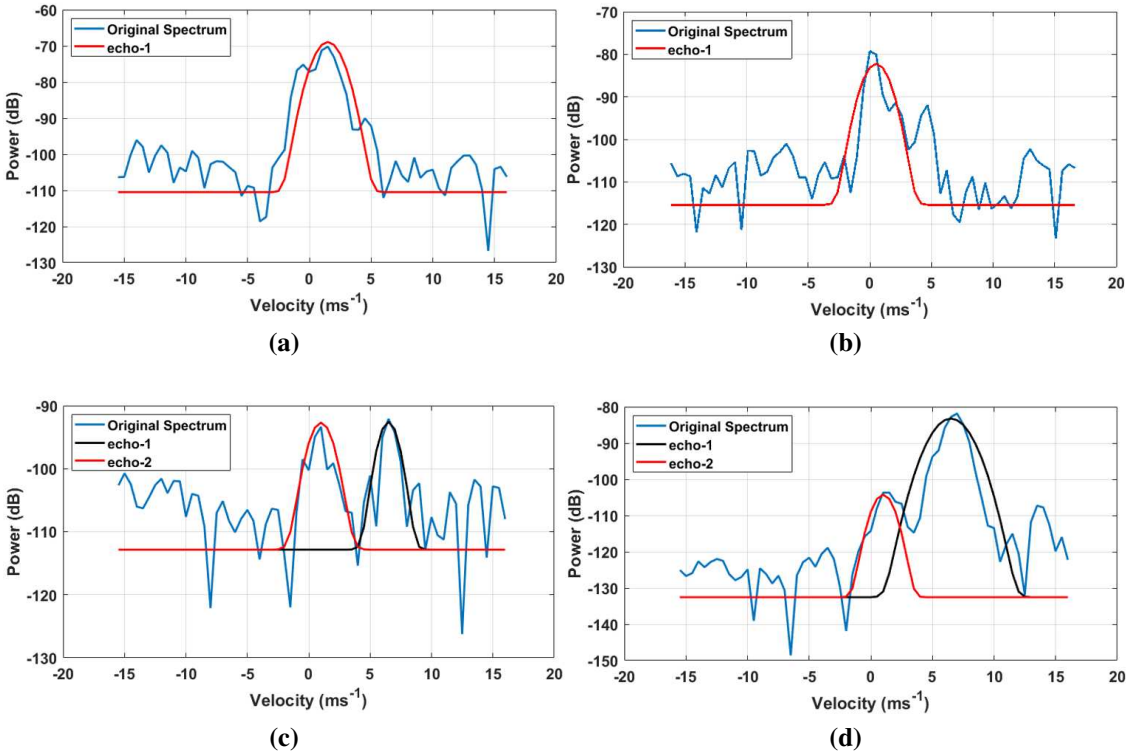

Figure 3.20: Sea clutter estimated as a single echo estimated at 5 km (A) and 10 km (B) respectively. Both precipitation and sea clutter echo detected by PTDM algorithm at 20 km (C) and 43 km (D) respectively from the 9^{th} November 2017 data at 0.5° elevation.

than the other regions. Hence the estimated noise floor by the PTDM is also higher. Fig. 3.20a and Fig. 3.20b shows that the PTDM has successfully been able to estimate the sea clutter spectra at 5 km and 10 km range bins, respectively. Fig. 3.20c and Fig. 3.20d shows that the PTDM has successfully been able to estimate both the sea clutter and precipitation spectra at 20 km and 43 km range bins, respectively. Fig. 3.21b shows the filtered PPI field obtained after using PTDM. Fig. 3.21c shows the residue of the reflectivity field Z_h after implementing PTDM.

Ideally, the residue field represents the estimated sea clutter values. However, in this case, errors in precipitation and clutter estimation with other contaminations are present here. After comparing the residue fields with the clutter map, we observe that after using PTDM, an appreciable sea clutter has been filtered. Fig.3.21b shows that the filter takes out quite a good amount of sea clutter. The suppression level provided is around 30 dB. Fig. 3.22a shows the histogram of CSR. The occurrence of $CSR = 0$ is the highest because it represents the regions where

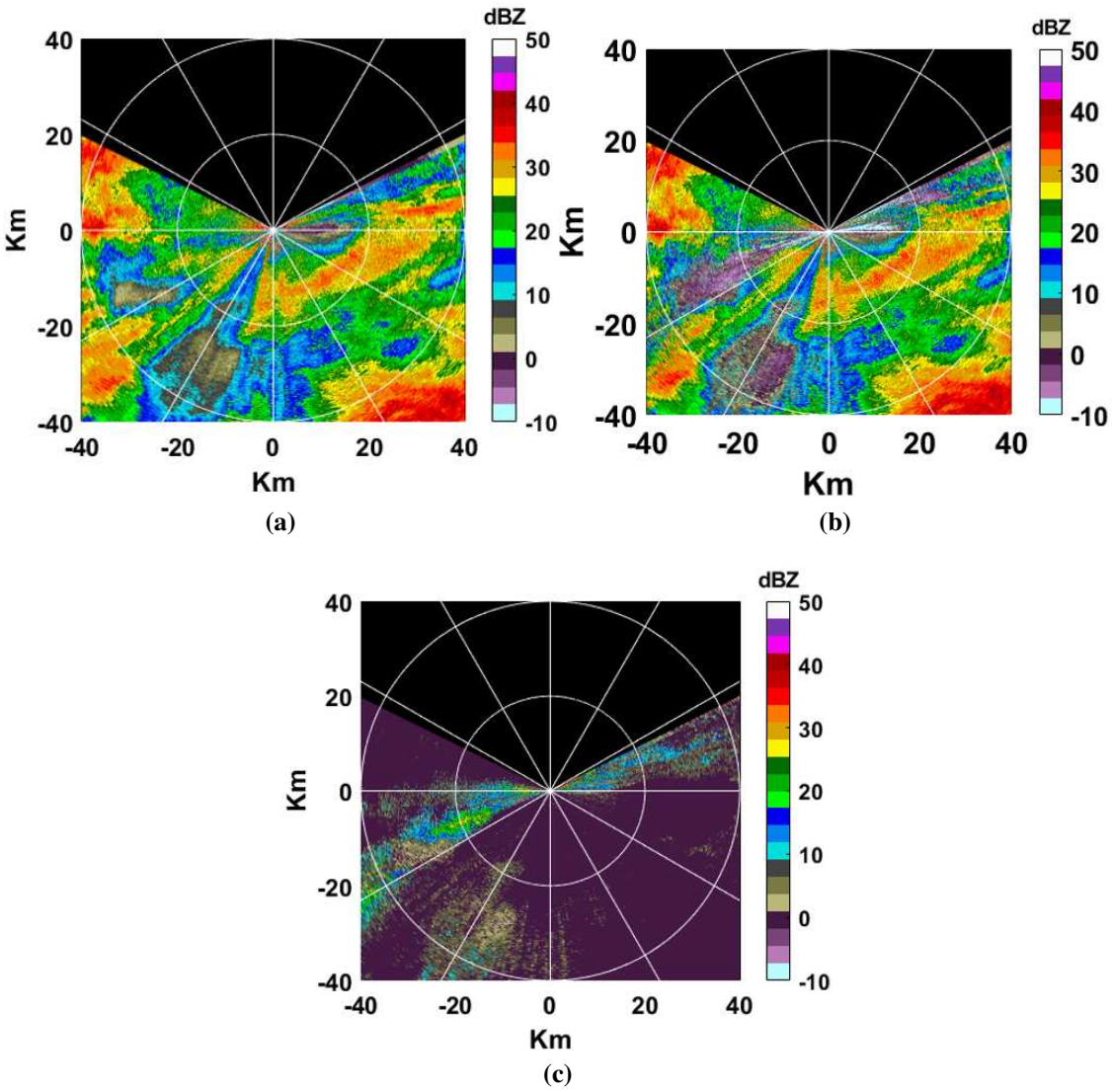

Figure 3.21: Clutter filtered PPI field using PTDM is shown in (B) using PTDM. The residue or the amount of clutter suppressed in the field is shown (C). The original unfiltered field containing both sea clutter clutter and precipitation is shown in (A).

$Z_{original} = Z_{filtered}$ and as it covers most of the PPI scan, hence its probability of occurrence is higher. The other values in the histogram correspond to the clutter suppression provided by PTDM.

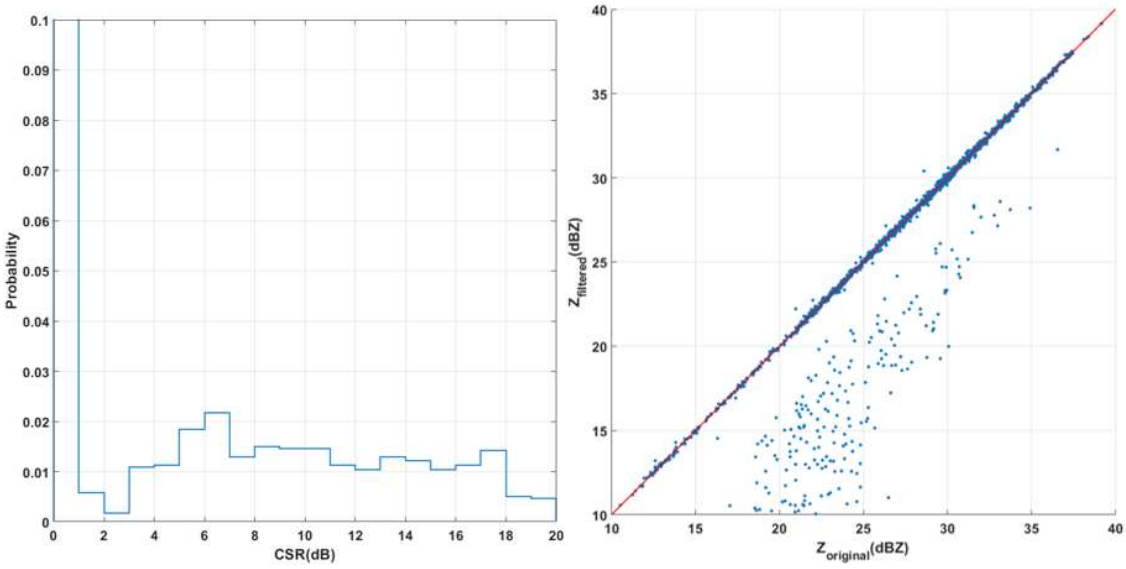

(a) (b)

Figure 3.22: Clutter suppression ratio distribution is shown in (A). The comparison between $Z_{original}$ and $Z_{filtered}$ is shown in the scatter plot in (B).

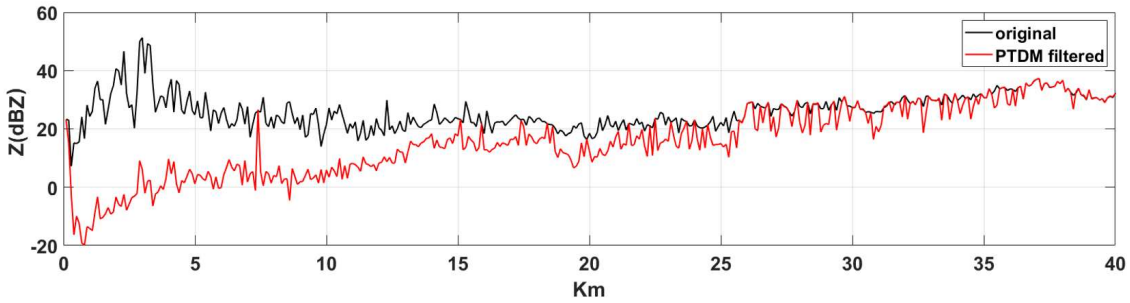

Figure 3.23: Original reflectivity profile (black) and weather profile (red) estimated from PTDM are shown along the range at 268° azimuth

Chapter 4

Sea clutter mitigation using advanced spectral processing

Spectral analysis often requires spectral noise reduction or a clear demarcation between the weather spectrum, noise, and other unwanted artifacts or clutter. Spectral thresholding can be used in this case. Spectral co-pol correlation is considered a classical thresholding parameter as it only retains the portion of the spectrum with higher coherence. Since weather signals are consistent or coherent; hence the signals received at the H and V channels are coherent. Therefore the co-pol correlation spectrum takes higher values, mostly in the range of 0.9 to 1. However, sometimes due to many phenomena like hail formation, strong vertical or horizontal motions, or presence of multiple hydrometeors, the coherency of the signals is lost, and the resulting spectrum is very broad and noisy. In such cases, the co-pol correlation spectrum cannot be used as a thresholding parameter. Thus a different thresholding parameter is required to overcome these problems.

4.1 Introduction

In Chapter 3, we explored and implemented three filtering methodologies, namely the Notch filter, GMAP, and the PTDM algorithm, to mitigate sea clutter in the SEAPOL radar data. In this chapter, we explore the method adopted by Moisseev et al. [1], incorporate results from PTDM, and include a thresholding strategy that will help in cleaning up the range-Doppler spectrograph and also help in separating the sea-clutter and precipitation spectra. This combined filtering technique is named as Advanced Spectral Filter (ASF). The thresholding parameter is named as Spectral Signal Quality Index (SSQI), which helps in suppressing noise and other unwanted interference in the spectra. As mentioned earlier, since sea clutter does not occur at zero Doppler, the existing ground clutter mitigation algorithms will not work. Chapter 3 showed the implementation of these filters. We used PTDM to separate the precipitation and the sea clutter spectra whose performance

is better than the notch and GMAP filters. In this chapter, we use the PTDM to estimate the exact location of occurrence of the sea clutter spectra and use the estimated parameters to generate the inference weights, which are used in the fuzzy logic classification to discriminate between sea clutter, precipitation, and noise. A spectral mask is generated from the classified field, which is used in spectral moment estimation. At the end of the chapter, we compare the performances of the algorithms and show that Advanced Spectral Filter (ASF) has better performance among all the filtering algorithms considered.

4.1.1 Sea clutter mitigation using Advanced Spectral Filter (ASF)

Spectral-domain analysis of dual-polarization weather radar signals is a relatively new area of research. Previous researches by Unal [29] and Yin et al. [30] show that it is possible to extract the weather signatures from the power spectrum of the back-scattered signals. In the spectral domain, the features of meteorological signals can be identified against possible clutter and background noise contamination. The standard radar processing algorithms like pulse-pair estimation operate on the time series samples in the time domain. It has been shown that the pulse-pair processing provides the least amount of bias and low variance in the generation of radar moments by Bringi and Chandrasekar [10] and it approaches the Cramer-Rao lower bound of minimum bias-variance performance.

Nevertheless, spectral processing has inherent advantages where ground clutter, unwanted echoes such as human-made RFI, and anomalous propagation can be easily identified, and robust filtering techniques can be developed to eliminate them. Spectral filters are already popular in the weather radar community. Siggia et al. [4], Moisseev et al. [1] and Yin et al. [30] have designed spectral filters that serve the purpose of mitigating unwanted echoes. Fig. 4.1 shows a complete procedure of detection and filtering of clutter in the form of a flowchart. It is to be noted that this method was used by Moisseev et al. [1] for ground clutter filtering. This chapter aims to investigate how this same methodology can be used in the case of sea clutter filtering. The working

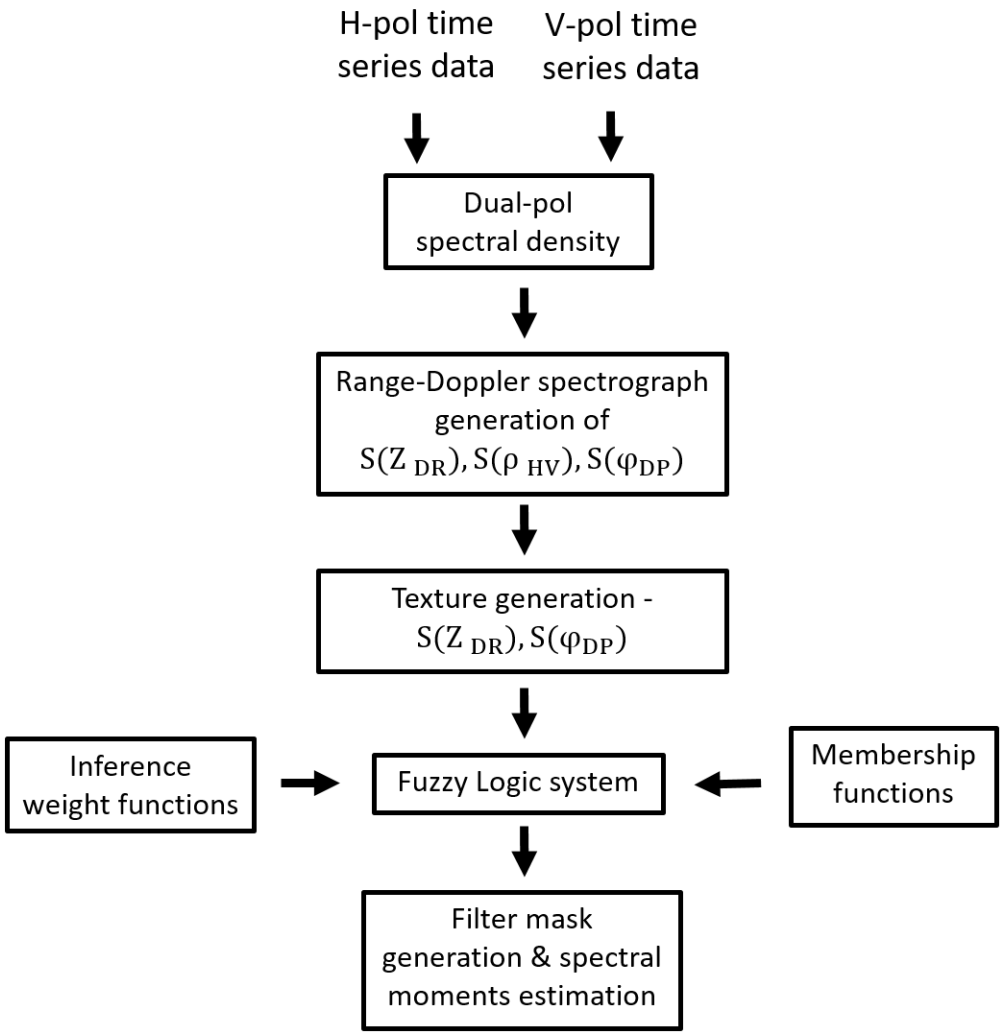

Figure 4.1: Flow chart showing the algorithm for adaptive polarimetric spectral filter by [1]

principle behind the spectral domain filtering algorithm is to utilize the distinct spectral properties for identifying and filtering the sea clutter components.

Range-Doppler spectrograph - Spectral decomposition of dual-polarization radar radar signals

The spectral processing approach starts from the recording of the received radar time-series samples from the horizontal and vertical polarization channels, H, and V, respectively, at specific elevation and azimuth angles.

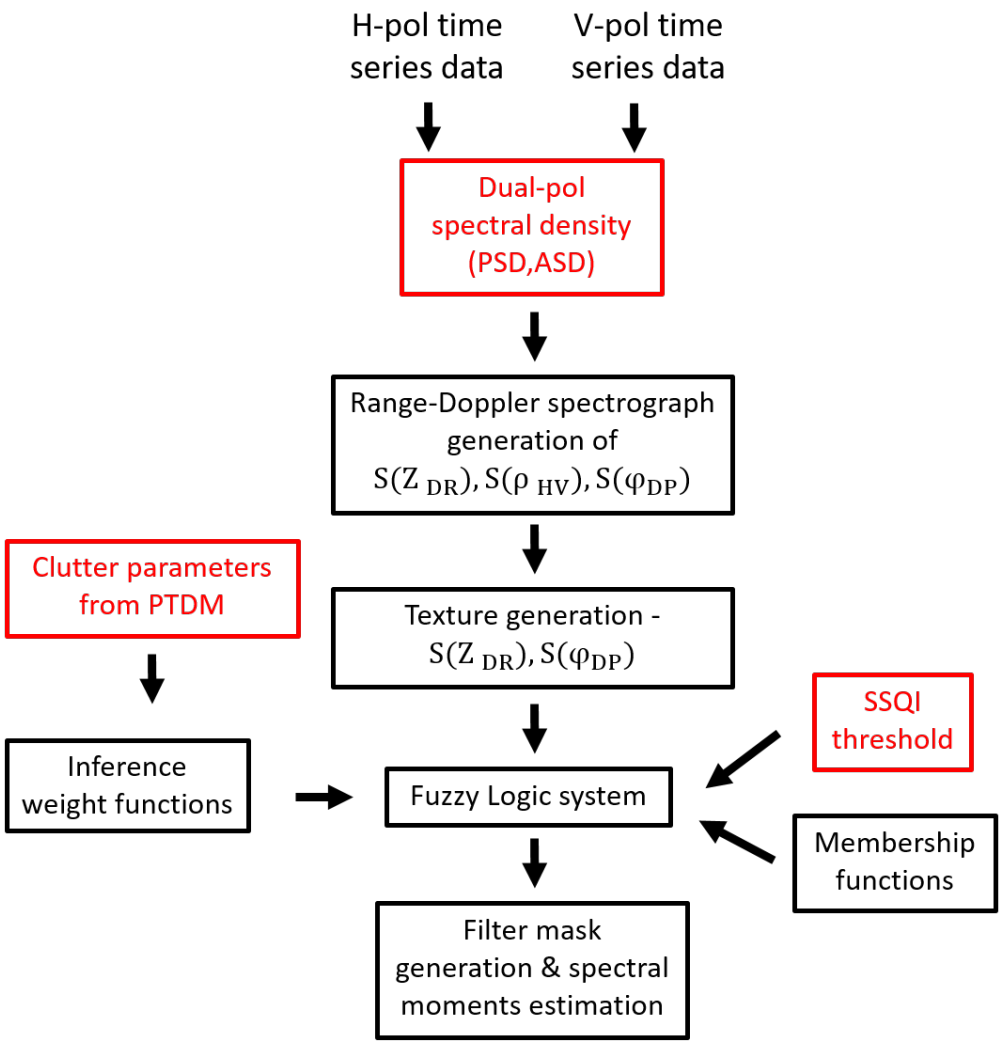

Figure 4.2: Flow chart showing the algorithm for Advanced Spectral Filter (ASF)

The spectrum estimation procedure, spectral decomposition of dual-polarization variables, and estimation of radar moments using spectral processing have been discussed in Chapter 2.

Texture generation

Spectral decompositions of dual-polarization radar data along a particular azimuth or elevation are done using Eqs. 2.17, 2.18 and 2.18 from Chapter 2. In general, researchers and engineers use the spatial variability of dual-polarization parameters to check for clutter contamination in weather observations.

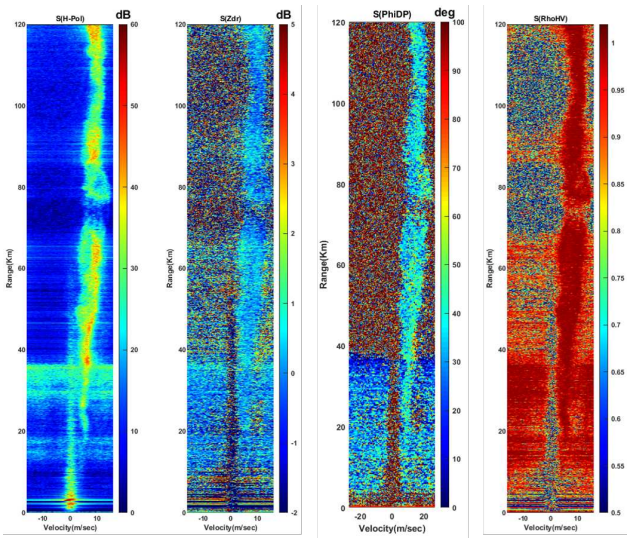

Figure 4.3: Range–Doppler spectrographs of $S(Z_h)$, $S(Z_{dr})$,$S(\phi_{dp})$, $S(\rho_{hv})$. The spectrographs are calculated from the SEAPOL observations collected on 9^{th} Nov 2017 along the azimuth of 268.4 deg.at an elevation angle of 0.5

A two-dimensional standard deviation is used as a measure of spatial variability where a 3×3 sliding window is used for the standard deviation computation. Textures of differential reflectivity and differential phase are computed and denoted as $SD[Z_{dr}]$ and $SD[\phi_{dp}]$, respectively. Moisseev et al. [1] have simulated the textures of noise for S-band and are observed to overlap with the distributions of ground clutter and precipitation. Similar behavior can be seen for C-band observations for sea clutter and precipitation, as shown by Alku et al. [31].

Fuzzy logic for clutter identification

Ryzhkov et al. [25] showed that it is possible to classify the radar data based on fuzzy logic to identify sea clutter, precipitation, and cloud. Moisseev et al. [1] showed that spectral-domain information could be used as inputs to a fuzzy logic module that can carry out the weather data classification where the outputs from the membership functions were weighed so as to identify ground clutter, precipitation, and noise correctly.

Since the ground clutter spectrum is centered at zero velocity and has a normal distribution, it is possible to simulate a set of weights and use those on the output of membership functions to get more accurate results. In the case of sea clutter, the clutter spectrum location may not be centered

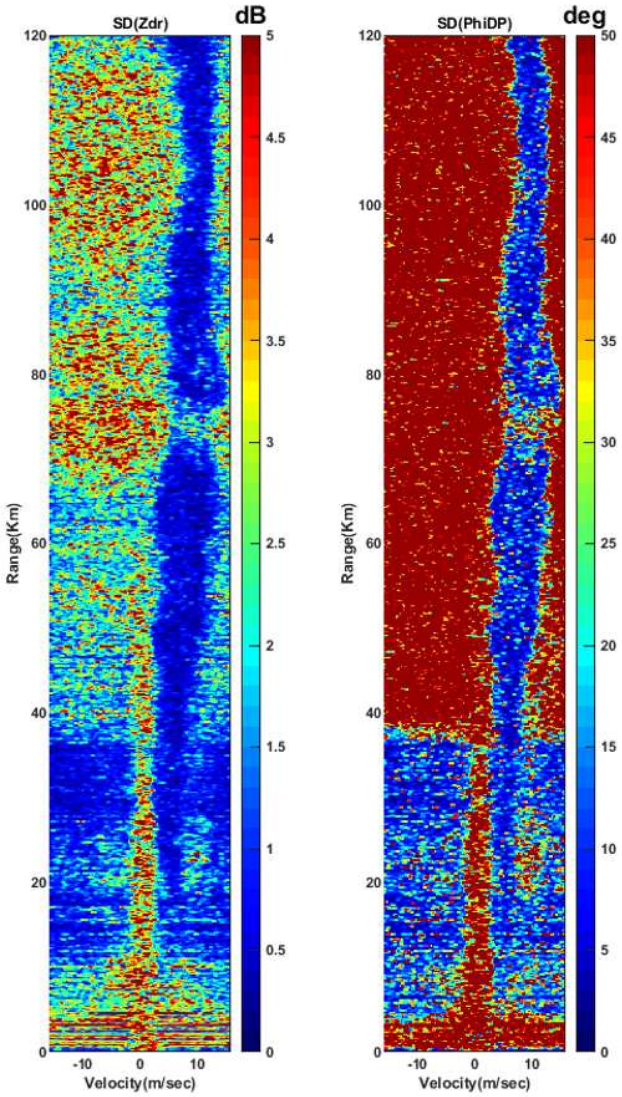

Figure 4.4: Range–velocity spectrographs of textures of (left) differential reflectivity $Z_{dr}(v)$ and (right) differential phase $\phi_{dp}(v)$. The spectrographs are computed from the same data as in Fig.4.3

at the zero Doppler and can vary since it depends on the random nature of the sea surface. Hence the simulated weights used for ground clutter identification cannot be used in case of sea clutter identification. A possible solution is to estimate the location of the sea clutter spectra and then design the set of weights accordingly.

Membership and Inference weight functions with clutter parameters from PTDM

The fuzzy logic classification scheme for sea clutter identification, implemented here, is similar to the one described by Moisseev et al. [1]. A beta membership function is used for defining

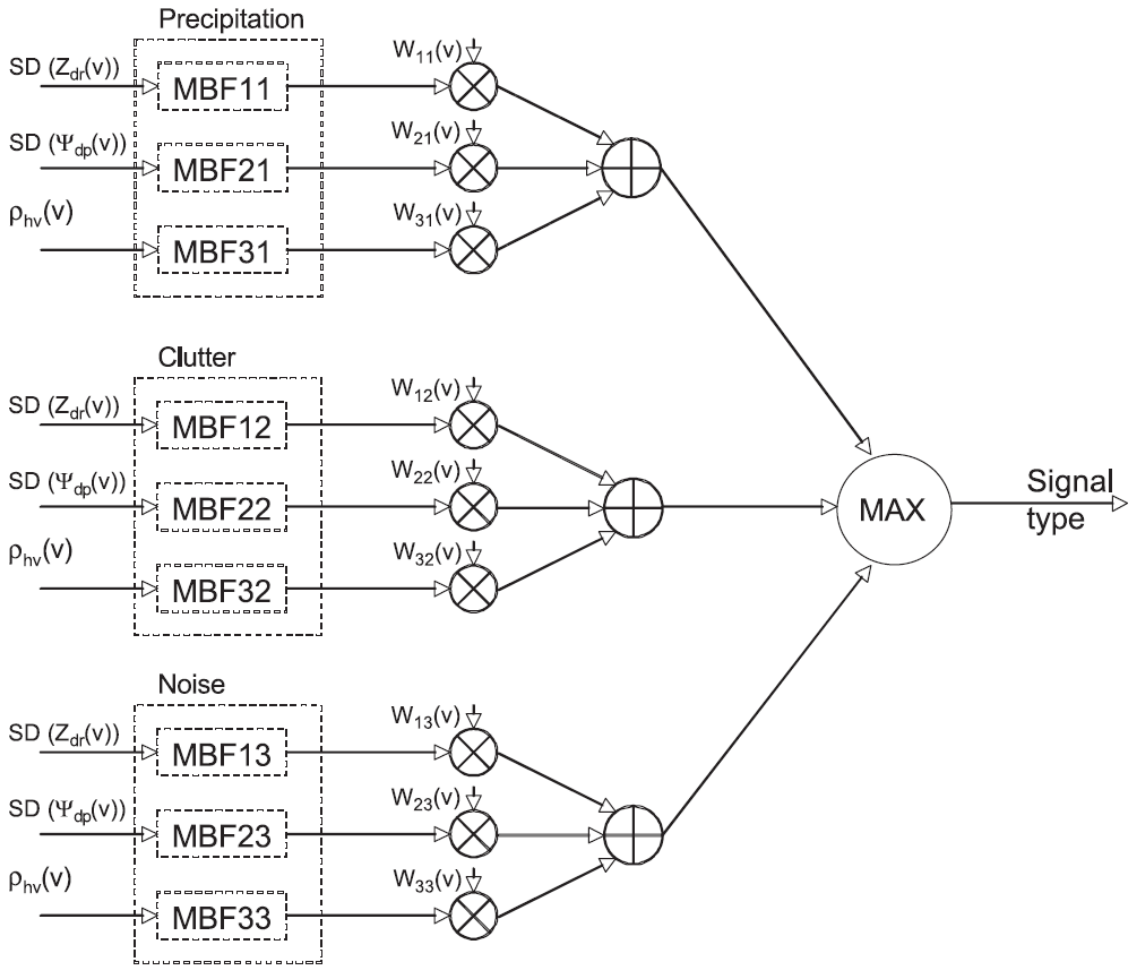

Figure 4.5: The fuzzy logic structure for classification of precipitation, clutter and noise as done by [1]

the respective classes of signals viz. sea clutter, precipitation, and noise. The parameters of the membership functions are deduced from the distributions shown in Fig. 4.6 and also following the values given by Alku et al. [31] and by Moisseev et al. [1] for sea clutter, precipitation and noise. The parameters of the membership function used here are shown in Table 4.1. The inference rule in the fuzzification process uses a summation and weighting of the respective classes to provide strength to a given class of input and follows Eq. 18 mentioned in [1]. The histogram of the textures of sea clutter and precipitation are shown in Fig. 4.6. It is seen that for precipitation, the majority of occurrence of values of the texture of $S(\hat{Z}_{dr})$ are less than 2 dB, whereas it is noisy and higher than 2 dB in case of sea clutter. The values of the texture of $S(\hat{\phi}_{dp})$ for precipitation are lesser than 15 dB, but for sea clutter, the values are much higher and have a broader distribution of

values. The values of $S(\hat{\rho}_{HV})$ for precipitation are greater than 0.9, while sea clutter shows a wide distribution of values of $S(\hat{\rho}_{HV})$ and has values lesser than 0.8.

Table 4.1: Parameters of the membership functions for the three different classes

	Sea Clutter	Precipitation	Noise
$SD(S(Z_{dr}))$	[1,25,3.1]	[1.3,10.8,0]	[0.86,21.5,1.4]
$SD(S(\phi_{dp}))$	[45,450,85.25]	[36.5,61,15]	[47,78,99]
$S(\rho_{hv})$	[0.115,2.881, 0.0153]	[0.17,17.5,0.9]	[0.46,17.9,0]

The proposed classification procedure uses three inputs: $SD(S(Z_{dr}))$, $SD(S(\phi_{dp}))$, and $S(\rho_{hv})$, and produces three classes: precipitation, noise, and clutter. Similar to Liu et al. [32] and Lim et al. [33], the transformation of the spectral decompositions of radar measurements into fuzzy sets is carried out by using membership functions of the beta functional form given as,

$$f(x, a, b, c) = \frac{1}{1 + |\frac{x-c}{a}|^{2b}} \tag{4.1}$$

where (a, b, c) for different inputs and classes are given in the Table 4.1.

The parameters of the membership functions are defined using observed distributions given in Fig.4.6. The observed distributions of $SD(S(Z_{dr}))$, $SD(S(\phi_{dp}))$ are calculated from 9^{th} November 2017 observations. High reflectivity weather echoes dominate these measurements. To include lower SNR cases, the precipitation membership functions are extended over a greater range of values. In Fig.4.7 proposed membership functions are shown.

The inference process architecture is shown in Fig. 4.5. The weighting factor is related to the Doppler velocity. Introducing the weighting factor when the Doppler velocity is close to zero can slightly push the reasoning process to the clutter class. The weighting function is chosen so that inference can be imposed on the confusing categories when the rules of different categories are similar in strength and do not overwhelm the process. The weight functions used in [1] has been shown in Fig.4.8, The clutter spectrum has been assumed to be Gaussian centered at the zero Doppler with a narrow spectral width. The weight function used is defined as the following

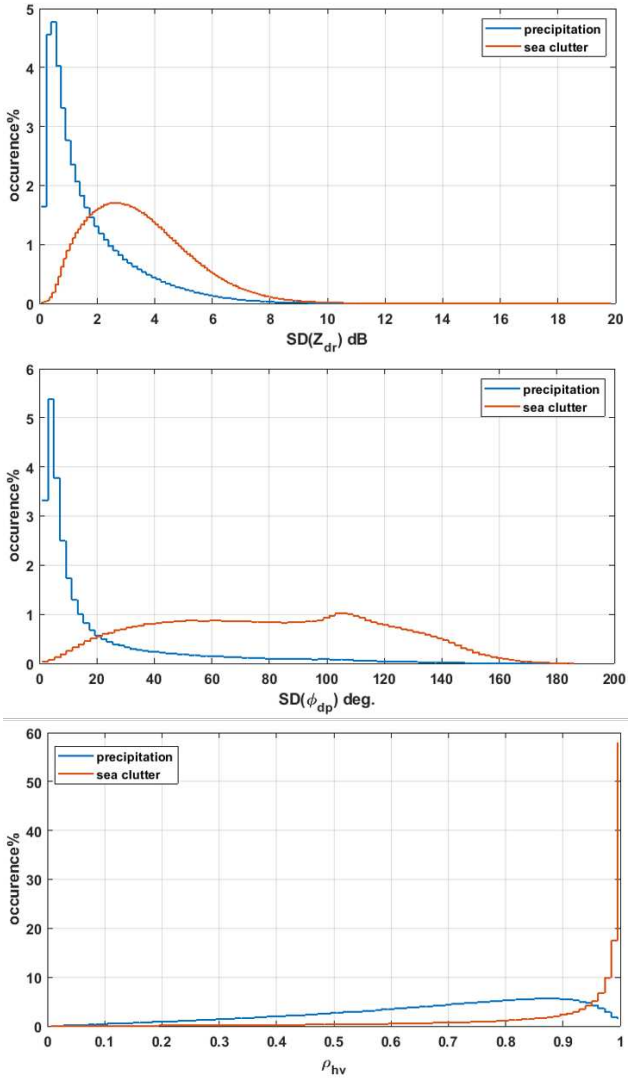

Figure 4.6: Histograms of the parameters for the fuzzy logic shown for precipitation and sea clutter

$$w = 0.4 + \frac{1}{\sigma\sqrt{2\pi}} exp(-\frac{v^2}{2\sigma^2}) \tag{4.2}$$

where $\sigma = 0.4$ ms^{-1}

The weight function for noise and precipitation classes is independent of Doppler velocity and fixed at the weight value of 0.5. Since sea clutter has different mean Doppler velocity and spectral width hence the above model for ground clutter identification cannot be used. We use the PTDM algorithm to estimate the central clutter velocity and spectral width to mimic the sea clutter spectrum shape.

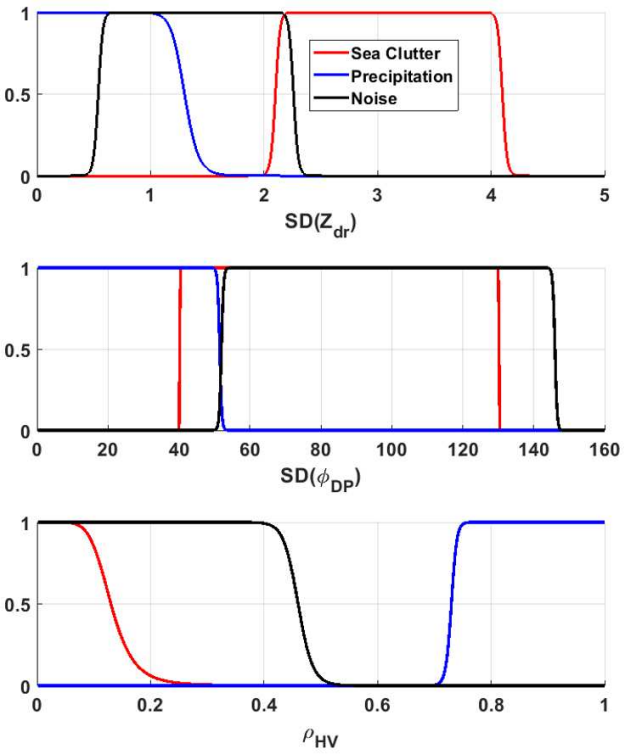

Figure 4.7: Membership functions used in fuzzy logic classification showing the beta functions for $SD(Z_{dr})$, $SD(\phi_{dp})$ and ρ_{hv} related to sea clutter, precipitation and noise

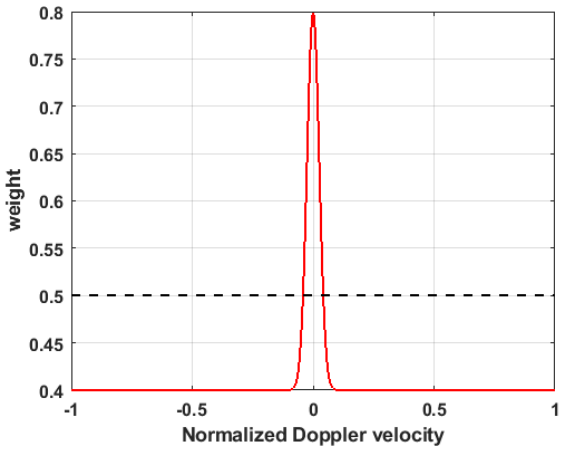

Figure 4.8: Inference weights associated with ground clutter shown in red and for noise and precipitation shown in dotted black line as used by [1]

$$w = 0.4 + \frac{1}{\hat{\sigma}_P\sqrt{2\pi}} exp(-\frac{(v-\hat{v}_P)^2}{2\hat{\sigma}_P^2}) \tag{4.3}$$

$\hat{v}_P$ & $\hat{\sigma}_P$ are the parameters obtained from PTDM algorithm. Fig. 4.8 shows the inference weight for clutter, precipitation and noise as used by [1] for identifying ground clutter. As mentioned earlier as sea clutter may occur at non-zero Doppler velocities hence Eq. 4.3 is used.

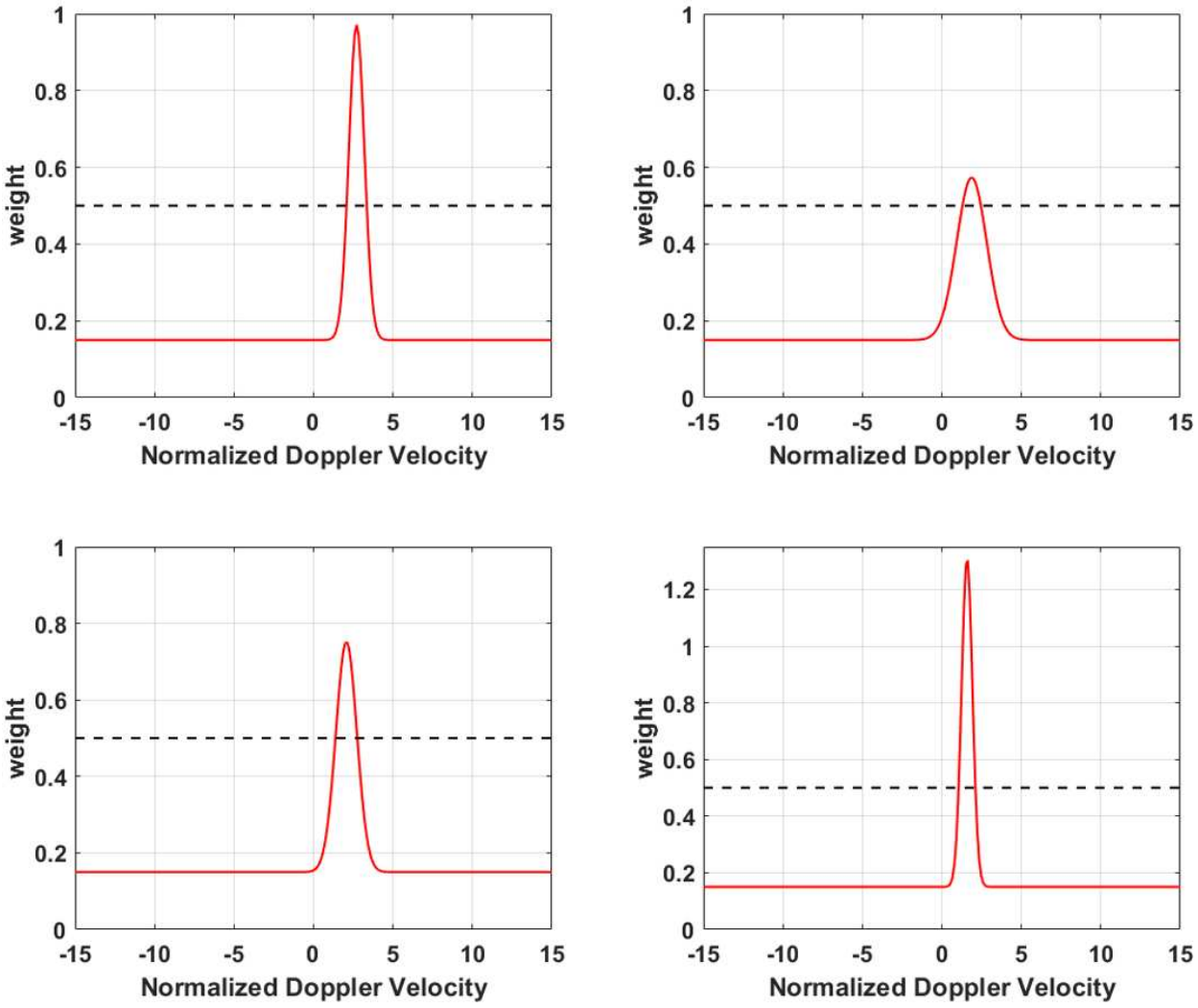

Figure 4.9: Inference weights associated with sea clutter shown in red and for noise and precipitation shown in dotted black line used in this research.

Spectral Signal Quality Index (SSQI) thresholding

Spectral-domain filtering techniques can be used to filter out different unwanted features in a signal. Spectral analysis often requires spectral noise reduction or a clear demarcation between the weather spectrum, noise, and other unwanted artifacts or clutter. As a solution to this problem

generally, the co-pol correlation spectrum is considered for thresholding the spectrum, where it only retains the portion of the spectrum with higher coherency. Since weather signals are consistent or coherent, hence the signals received at the H and V channels are also coherent, so the co-pol correlation spectrum takes higher values, mostly in the range of 0.9 to 1.

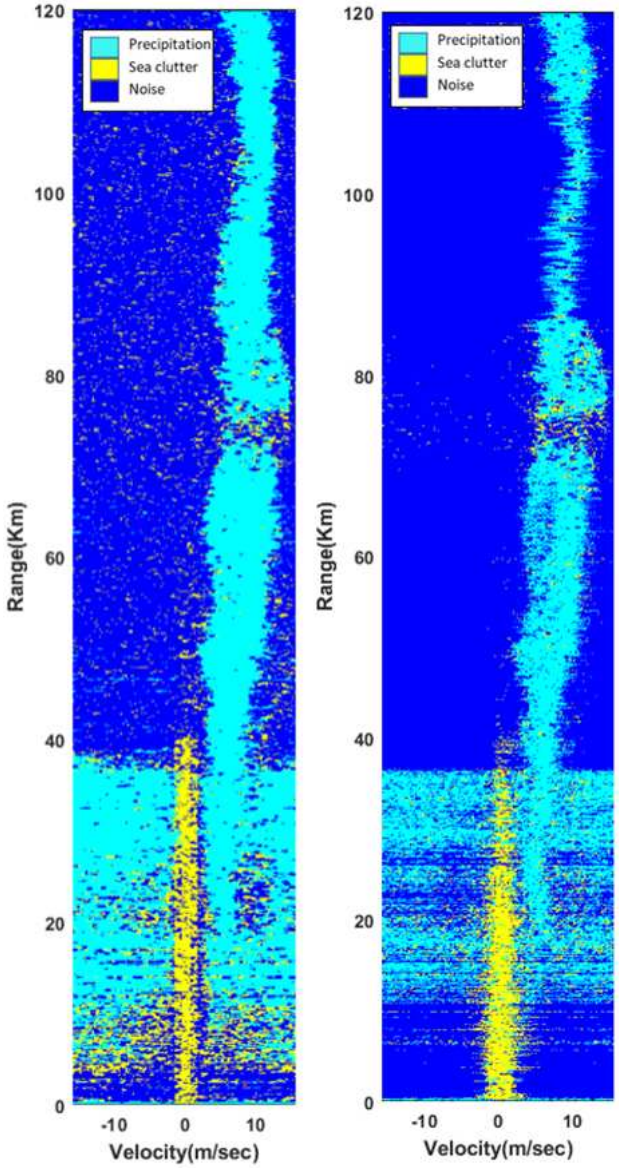

Figure 4.10: The fuzzy classification results shown after using the algorithm proposed by Moisseev et al. [1] (left) and the classification spectrograph shown in right is done using the ASF framework

However, sometimes due to various phenomena like hail formation, strong vertical or horizontal motions, or presence of multiple hydrometeors, the coherency of the signals is lost, and the resulting spectrum is very broad and noisy with very high variance. In such cases, co-pol correlation spectrum can not be used as a thresholding parameter. In many cases, such as clutter, other interferences, particle mixtures, or melting hail, the signal coherency is not observed, i.e., the coherency values are low sometimes as low as 0.8. Hence, if a threshold of 0.9 is used, these regions will be excluded, although they are valid signals with a high Signal to Noise Ratio. In pulse pair processing Co-pol Correlation (ρ_{HV}) and Signal Quality Index (SQI) are used for thresholding to get clean products. In this chapter, Spectral Signal Quality Index (SSQI) has been proposed as a thresholding parameter. Spectral-domain thresholding using SSQI can be used to clean up the data, get better dual-polarization products, and overcome the low coherency problem. The moments retrieved from the filtered spectra are the clutter suppressed products. Hence thresholding with SSQI can be considered as a sea clutter filtering technique. This section shows that thresholding based on SSQI can distinguish the weather spectrum from noise and sea clutter. This technique is demonstrated using data from SEAPOL, a C-band shipborne dual-polarization weather radar, to remove sea clutter effectively. The existing spectral parameters are the spectral reflectivity ($S(Z_h)$), spectral differential reflectivity ($S(Z_{DR})$), Spectral differential phase ($S(\phi_{DP})$) and the co-pol correlation spectrum ($S(\rho_{HV})$).

In the case of spectral moment calculation, it is recommended to compute the moments from a thresholded spectrum. For fast scanning radars, since the number of pulses is very small, for example, 64 samples, in this case, it cannot be used to obtain a smooth spectrum. In the case of the co-pol correlation spectrum, which largely depends on the expected values of H, V, and the cross-spectrum, the final spectrum has very high variance, and the entire co-pol correlation takes values close to unity. There are various methods to overcome this problem as mentioned below

- spectral-averaging over different data segments.
- spectral-averaging over range or azimuth.

- scan to scan spectral averaging.

Due to extremely less number of samples, spectral averaging over different data segments fails to give good results hence cannot be used for thresholding. In case of averaging over range or azimuth, the range or azimuth resolution will be lost after averaging, hence it not recommended. This chapter shows that Spectral Signal Quality Index ($SSQI$) is an effective solution for spectral thresholding. The motivation comes from the co-pol correlation spectrum. The co-pol correlation spectrum ($S(\rho_{HV})$) can be considered as a spectral domain equivalent of co-pol correlation (ρ_{HV}) which is a time domain parameter. The equivalency is observed if looked into the underlying equations of both the parameters as shown below,

$$\rho_{hv} = \frac{\sum_{m=0}^{N-1} V(m)H^*(m)}{\sqrt{\sum_{m=0}^{N-1} |H(m)|^2 \sum_{m=0}^{N-1} |V(m)|^2}} \tag{4.4}$$

where $H(m)$ and $V(m)$ is the m^{th} sample of a N long time series signals ontained from the Horizontal and Vertical polarization channels, respectively.

$$S(\rho_{hv}) = \frac{\sum_{k=0}^{N-1} S_{hv}(k)}{\sqrt{\sum_{k=0}^{N-1} S_{hh}(k) \sum_{k=0}^{N-1} S_{vv}(k)}} \tag{4.5}$$

where S_{hv} is the cross-spectrum between horizontal and vertical polarization time series signal calculated with FFT length of N.

Eq.4.4 is the correlation coefficient from the time domain while Eq.4.5 is the correlation coefficient derived from the spectral domain. Intuitively, it can be observed that the cross-correlation in the numerator of Eq.4.4 is replaced by cross spectra in Eq.4.5. While H and V auto-correlation in the denominator of Eq.4.4 is replaced by auto-spectra in Eq.4.5. With this similarity, the equation of the time domain SQI is observed as described by Eq.4.6

$$SQI(m) = \frac{|R_1(m)|}{R_0(m)} \tag{4.6}$$

where R_1 is auto-correlation at lag 1 and R_0 is auto-correlation at lag 0. Similarly in the spectral domain, if we define S_0 and S_1 which are auto-correlation spectrum at lag 0 and 1 respectively, then the Spectral Signal Quality Index (SSQI) can be defined as

$$SSQI(f) = \frac{|S_1(f)|}{S_0(f)} \tag{4.7}$$

As mentioned earlier, pulse-pair processing, which is a time-domain auto covariance processing, is generally used for computation of radar moment. However, when signals are contaminated with unwanted echoes from different clutter and interference, the periodogram estimator of the power spectral density (PSD) is seen to be a significant tool of spectral analysis. The drawback of PSD is that it does not convey any phase information. The autocorrelation spectral density (ASD), a generalization of the classical PSD provides explicit phase information and can be used to identify and remove unwanted signals. Warde et al. [34] have used the ASD for spectral analysis of weather radar data in various applications.

The lag-l ASD estimator is defined as a generalization of the PSD estimator based on the modified periodogram. This is given by

$$S_l(f) = \frac{T_s}{N-l} F_0^*(f) F_l(f) \tag{4.8}$$

where,

$$F_l(f) = \sum_{m=0}^{N-l-1} d(m) V(m+l) e^{-j2\pi f T_s m} \tag{4.9}$$

where $V(m)$ is the complex time series, and d is the data window. The data window is real-valued function, symmetric about $(N-l-1)/2$, normalized for average unit power, and takes zero values outside the interval $[0, N-l-1]$.

Thus following Eq. 4.6, Spectral Signal Quality Index can be calculated as

$$SSQI(r,k) = \frac{|S_{HH/l}(r,k)|}{S_{HH}(r,k)} \tag{4.10}$$

where $S_{HH/l}$ is the lag-l ASD calculated for the horizontal channel; similarly, SSQI can be calculated for the vertical channel. In this work, $l = 1$ has been considered such that the SSQI is equivalent to the time domain SQI. To calculate the spectral SQI as the moment we simply just perform spectral averaging, hence

$$SQI(r) = \sum_{k=0}^{N-1} SSQI(r, k) \tag{4.11}$$

Filter mask generation & spectral moments estimation

To filter out clutter, various interferences and to reduce the effect of background noise, a spectral mask is generated from the classification field in Fig. 4.10. The firing strength for a rule in the fuzzy logic classification can be expressed as

$$R_j(v) = w_{1k}\mu_k\{SD[Z_{dr}(v)]\} + w_{2k}\mu_k\{SD[\phi_{dp}(v)]\} + w_{3k}\mu_k\{SD[\rho_{hv}](v)]\} \tag{4.12}$$

Here the subscript j is the feature tag for either precipitation, sea clutter or noise class. The membership functions $\mu_j \in [0, 1], j = 1, 2, 3$.

Let $j \rightarrow k$ denote the rule j votes to class k, then

$$d_k(v) = \max_{j \rightarrow k} R_j(v) \tag{4.13}$$

The precipitation mask m_p is constructed such that it is equal to 1 if the fuzzy logic votes a particular spectral line in favor of precipitation and zero otherwise. The clutter mask m_c is constructed such that it is equal to 1 if the fuzzy logic votes a particular spectral line in favor of clutter and zero otherwise. Next for the moments' calculation, only these spectral lines are used in the computation by the spectral processing algorithm. The spectral processing algorithms, as used by Moisseevet al. [1] for moments calculations, are used here. For a given range gate the H-pol Reflectivity (Z_h) is calculated as a sum of precipitation power spectral lines

$$Z_h = \sum_{k=0}^{N-1} m_p(k)\left[\hat{S}_{hh}(k)\right] \tag{4.14}$$

The mean Doppler velocity ($\hat{v}$) and spectrum width ($\hat{\sigma_v}^2$) which are few of the basic radar moments are computed as follows

$$\hat{v} = \frac{\sum_{k=0}^{N-1} v_k m_p(k)\left[\hat{S}_{hh}(k)\right]}{\sum_{k=0}^{N-1} m_p(k)\left[\hat{S}_{vv}(k)\right]} \tag{4.15}$$

$$\hat{\sigma_v}^2 = \frac{\sum_{k=0}^{N-1} (v_k - \hat{v})^2 m_p(k)\left[\hat{S}_{hh}(k)\right]}{\sum_{k=0}^{N-1} m_p(k)\left[\hat{S}_{vv}(k)\right]} \tag{4.16}$$

Among the polarimetric variables Differential Reflectivity (Z_{dr}) and Co-polar Correlation (ρ_{hv}) can be can be calculated as follows:

$$Z_{dr} = \frac{\sum_{k=0}^{N-1} m_p(k)\left[\hat{S}_{hh}(k)\right]}{\sum_{k=0}^{N-1} m_p(k)\left[\hat{S}_{vv}(k)\right]} \tag{4.17}$$

$$\rho_{hv} = \frac{\sum_{k=0}^{N-1} m_p(k)\left[\hat{S}_{hv}(k)\right]}{\sqrt{\sum_{k=0}^{N-1} m_p(k)\left[\hat{S}_{hh}(k)\right] \sum_{k=0}^{N-1} m_p(k)\left[\hat{S}_{vv}(k)\right]}} \tag{4.18}$$

Fig. 4.11b shows the filtered PPI field obtained after using ASF. Fig. 4.11c shows the residue of the Reflectivity field Z_h.

Fig. 4.11c shows the residue, which ideally should be the estimated sea clutter field. Comparing the residue fields with the clutter map, we see that the ASF has taken out an appreciable sea clutter from the clutter flagged range bins. As seen from Fig.4.12 the filter provides an appreciable amount of suppression. The suppression level provided is around 20-35 dB. Fig. 4.12a shows the histogram of CSR. The occurrence of $CSR = 0$ is the highest because it represents the regions where $Z_{original} = Z_{filtered}$ and as it covers most of the PPI scan hence its probability of occurrence is higher. The other values in the histogram correspond to the clutter suppression provided by the ASF. The maximum suppression provided is 35 dB.

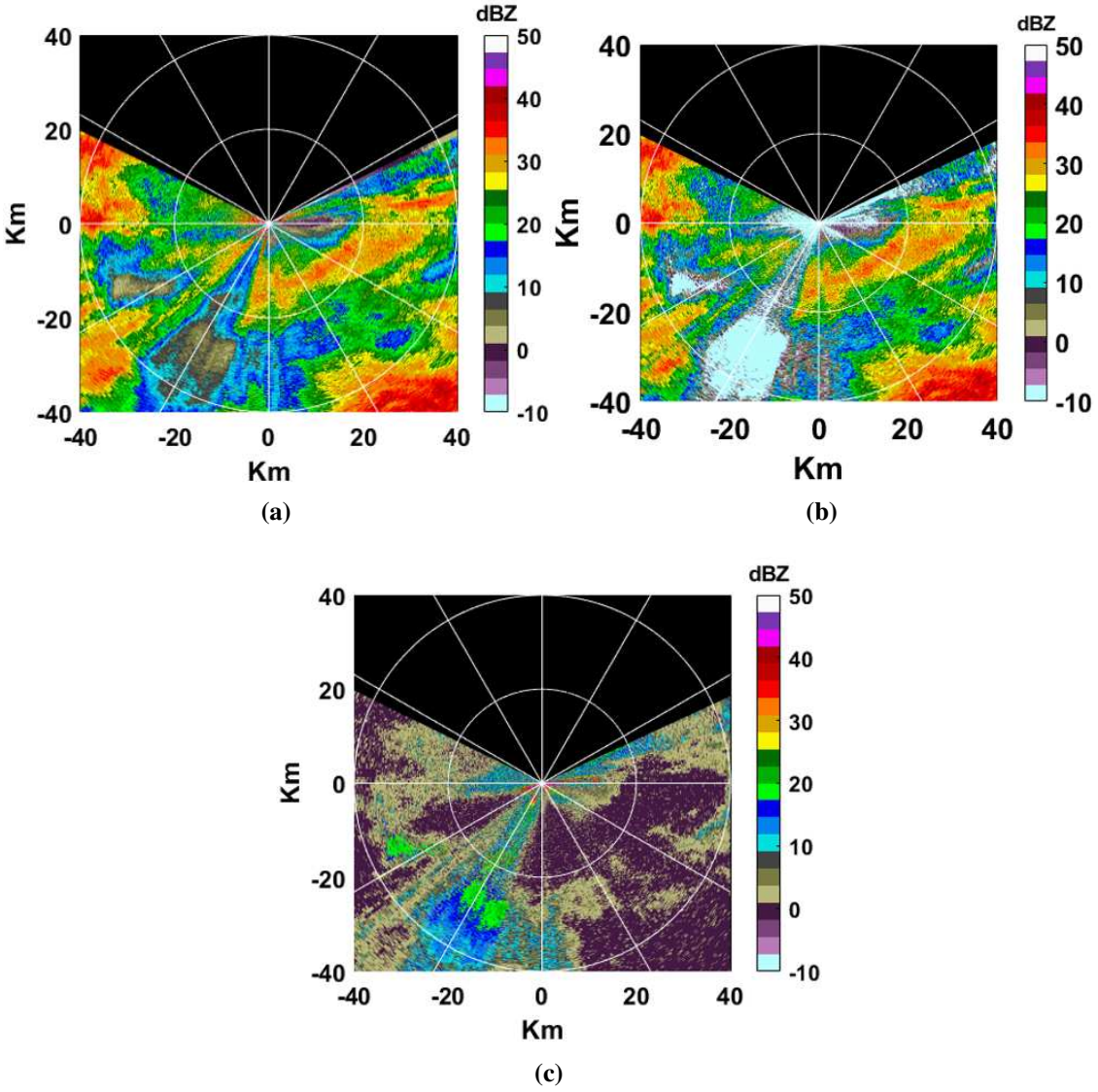

Figure 4.11: Clutter filtered PPI field using the ASF is shown in (B). The residue or the amount of clutter suppressed in the field is shown (C). The original unfiltered field containing both sea clutter and precipitation is shown in (A)

Fig. 4.12b shows the scatter plot between filtered and original reflectivity field. The red line corresponds to the one to one correspondence where both the fields have equal values, i.e., these points represent the regions where no filter has been used. These regions either have precipitation or noise. The points below the one to one line correspond to the regions where the ASF filter has been applied. Since after filtering, the overall calculated reflectivity is lower than the original reflectivity; hence they occur below the line. If the error in the estimation of precipitation leads

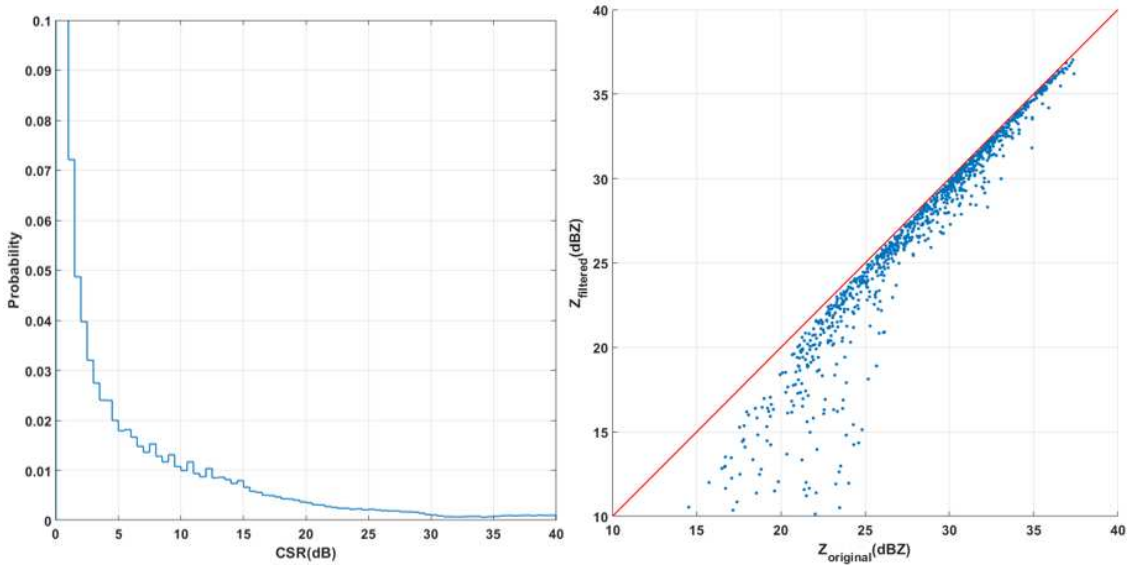

(a) (b)

Figure 4.12: Clutter suppression ratio distribution is shown in (A). The comparison between $Z_{original}$ and $Z_{filtered}$ is shown in the scatter plot in (B).

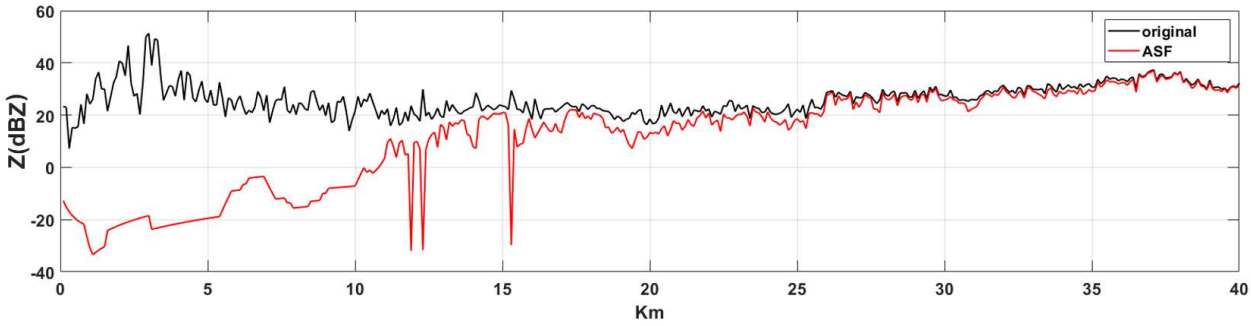

Figure 4.13: Original reflectivity profile and filtered profile using ASF are shown along the range at 268°

to positive bias, then the points occur above the one to one correspondence line. Unlike GMAP, Notch filter, or PTDM, these erroneous points are almost negligible in this case. Fig. 4.13 shows the original (black) and filtered (red) reflectivity range profiles along the 268° azimuth.

4.2 Comparison of Sea clutter mitigation algorithms

While investigating different methods to suppress sea clutter, it is necessary to compare the performances of the algorithms under study and point out that one that has the best performance. Fig 4.14 shows the comparison between the algorithms discussed so far. The ray along 268°

azimuth is chosen for this. The original reflectivity profile is shown in black. The Notch, GMAP, PTDM, and ASF filtered profiles are shown in blue, magenta, green, and red.

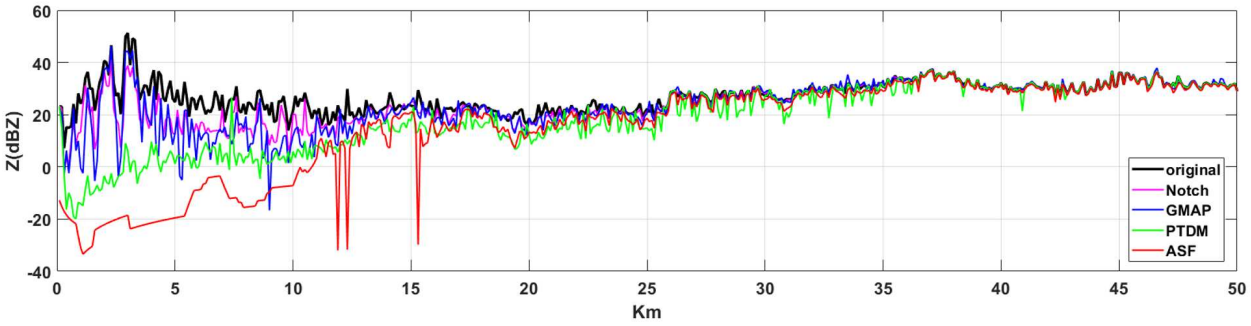

Figure 4.14: Original reflectivity profile (black) and filtered reflectivity profiles are shown along the range at 268°

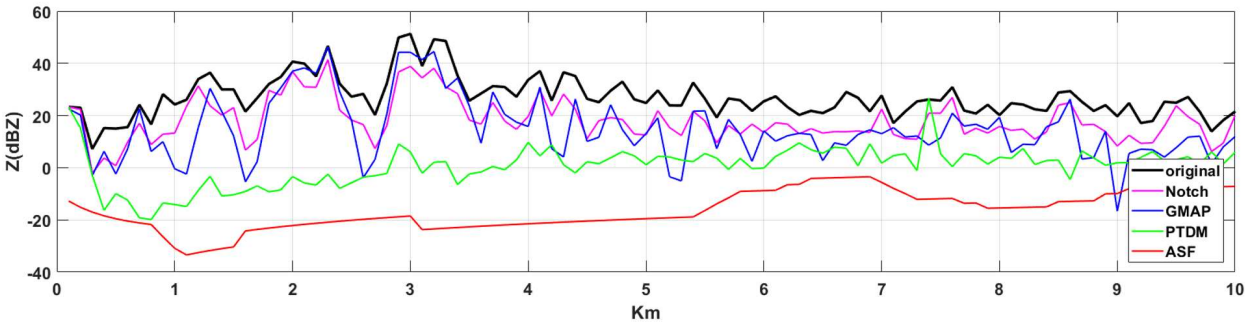

Figure 4.15: Original reflectivity profile (black) and clutter filtered profiles are shown along the range at 268° in first 10 km to observe sea clutter suppression

As seen from Fig. 4.14 the filter performances in the following order

$$CSR_{ASF} > CSR_{PTDM} > CSR_{GMAP} > CSR_{Notch} \tag{4.19}$$

Fig.4.15 shows the filtered profiles in the first 10 km of range. It essentially shows how much the filtering techniques have been able to suppress the sea clutter. Fig.4.16 shows the filtered profile from 30 to 60 km showing the ability of the filters to retain the precipitation signal. The clutter

suppression ratio (CSR) is calculated, which helps determine the performances of the sea clutter filters. The CSR histogram is shown in Fig. 4.17a.

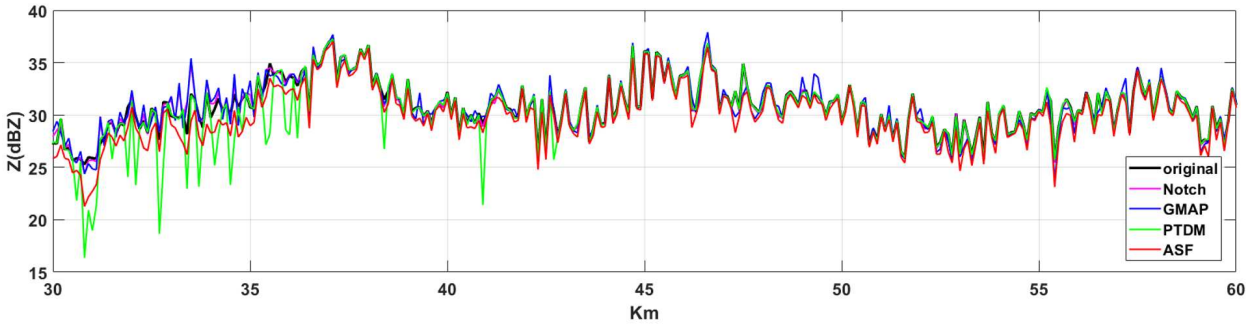

Figure 4.16: Original reflectivity profile (black) and the clutter filtered profile are shown along the range at 268° from 30 to 60 km showing how the precipitation signals are retained

The histogram in Fig. 4.17a shows a very high probability at 0 dB CSR, which means that the occurrence of the unfiltered bins are the highest. This is evident because the number of precipitation bins are higher in the particular PPI scans, as seen in the classification figure shown in Fig.3.5.

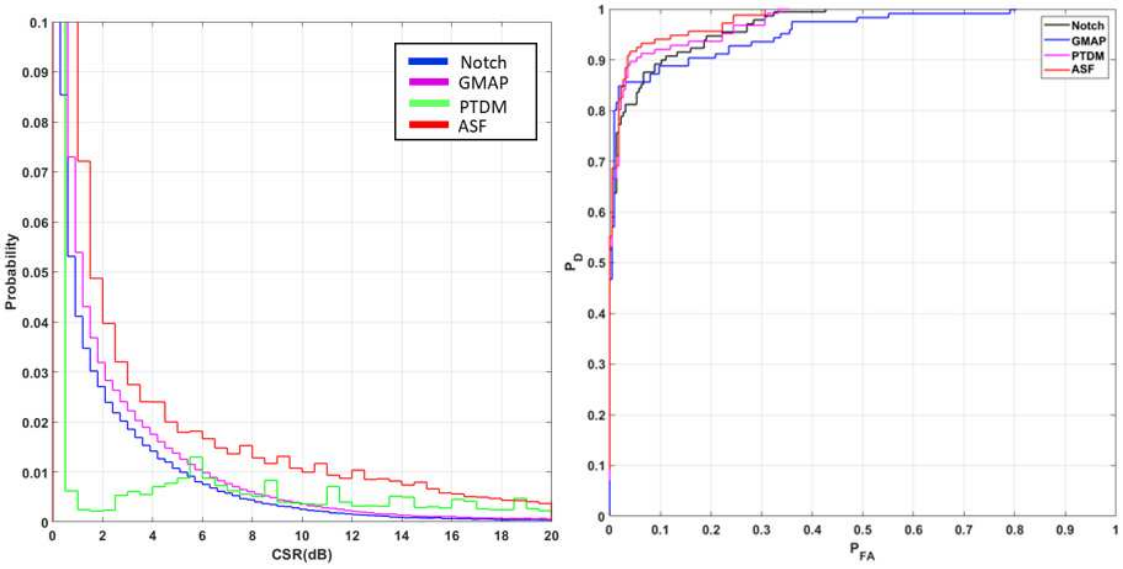

(a) **(b)**

Figure 4.17: Histogram of clutter suppression ratio (CSR) is shown in (A). The ROC curves for the filtering methods shown in (B).

We also observe that the probability of occurrence of the CSR is highest for the ASF followed by GMAP, then PTDM and finally notch filter. This can be interpreted as that the Advanced Spectral Filter can retain most of the precipitation signals. The notch filter has the lowest probability because it places a notch around zero Doppler by default, and since a higher spectral width has been used, it partly takes out the precipitation spectrum as well. Hence it retains the least amount of precipitation. Note that for the notch filter, PTDM or GMAP, there is no precipitation mask used. Also, we have observed that the ASF gives the highest maximum clutter suppression among the four filters.

Chapter 5

Study of rain and hail mixture using spectral polarimetry

Polarimetric measurements from dual-polarization weather radar have given the researchers the tools to determine the size and shape of hydrometeors in a radar resolution volume. Combining Doppler information with the polarimetric measurements allows researchers to do spectral analysis, study, and characterize the microphysics and dynamics of a storm at specific radar resolution volumes. The study of both spectral and polarimetric properties of weather echoes is known as Spectral Polarimetry. Therefore spectral polarimetry has proven to be an essential tool for studying different varieties of storms.

5.1 Introduction

This chapter investigates how storms are characterized using spectral polarimetry. Spectral analysis has been done on real data collected from a field campaign that recorded unique intensive mesoscale convective storms in Argentina. Firstly spectra of rain in a stratiform case have been analyzed. Next, the spectral properties of an intense convective case have been studied and reported. In this case, the dual-polarization spectrum of precipitation with rain and hail mixtures are characterized. The main goal is to incorporate Doppler information with polarimetric measurements in dual-polarization weather radar that will help in unveiling various microphysical properties in relation to the dynamics of the storm in a radar resolution volume. Similar work has been done by Wang et al. [35] for studying hail at low elevation using spectral polarimetry. Phenomena such as size sorting, Zdr column evolution, etc. are observed. Since the interest is in the convective storms hence radar scans along a fixed azimuth covering different elevations, also known as Range Height Indicator (RHI), have been analyzed. Different properties, including multi-modal spectrum, slopes in Zdr spectrum, and lowering of co-pol correlation spectrum, were observed. Study of the general

rain spectrum has been done on the observations recorded during the Intensive Observing Period (IOP) from 1 November – 15 December 2018. The more extreme convective storm properties were studied from the data collected during the Extended Hydrometeorology Observing Period (EHOP) that took place from 1 June 2018 – 30 April 2019.

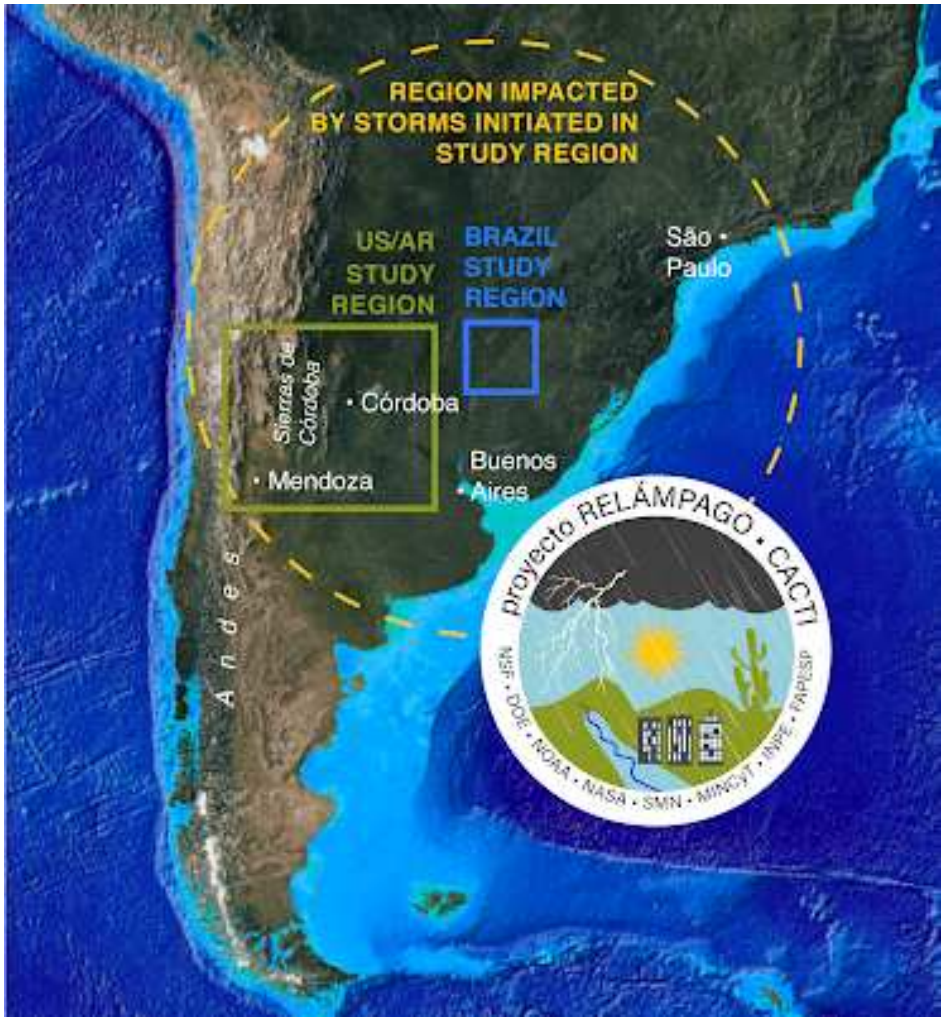

Figure 5.1: The RELAMPAGO campaign location has been shown in the figure. Picture courtesy of Dr. Steve Nesbitt, University of Illinois at Urbana-Champaign [2].

5.2 The Relampago field campaign

The RELAMPAGO campaign was done in the Cordoba region of Argentina. RELAMPAGO or most commonly known as Remote Sensing of Electrification, Lightning, And Mesoscale/Microscale

Processes with Adaptive Ground Observations, had two phases, namely the Extended Hydrometeorology Observing Period (EHOP) and the Intensive Observing Period (IOP). Data sets from both periods have been analyzed in this chapter. In this campaign, a few of the tallest storms in the world were observed extending up to 20 km from the ground. The storms were characterized by very strong updrafts, downdrafts, and vertical wind shear. This campaign's goal was to study the Mesoscale Convective Systems, which are known to be very frequent and most intense in this region than anywhere else. One of the main goals of this campaign was to study the life cycle of these unique storms from the beginning to the end. Numerous organizations came into a collaboration and deployed a large number of sensors to collect data. Since the storms were observed to generally generate along the Andes and the Sierras de Cordoba hills, hence most of the research teams deployed their instruments in this region.

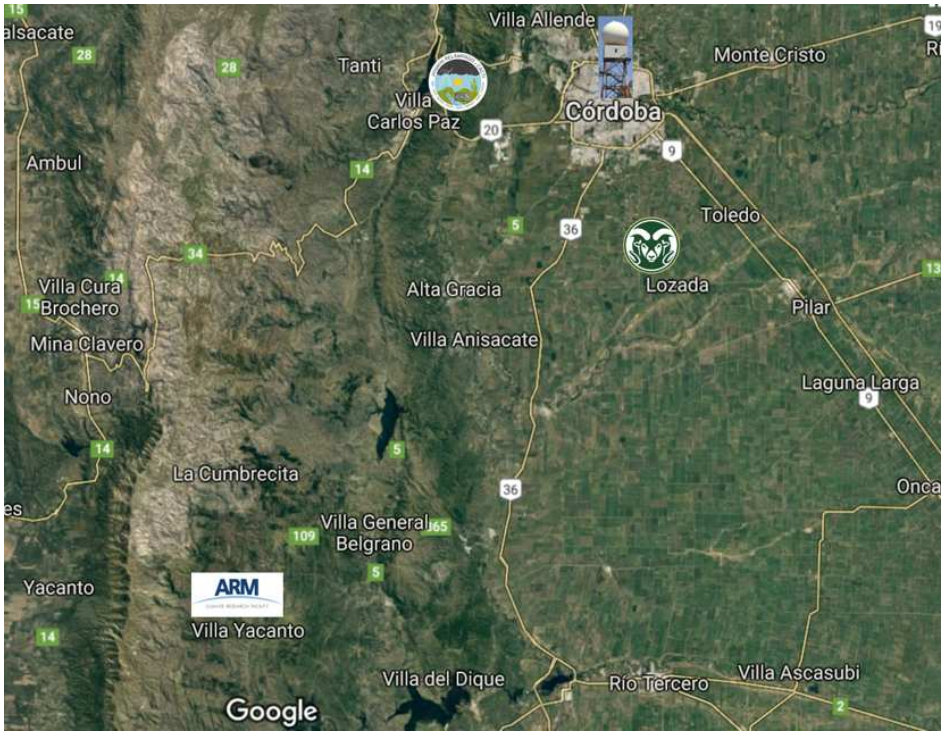

Figure 5.2: The deployment location of CSU-CHIVO radar (Rams logo) during RELAMPAGO as described by Ivan et al. [3].

The campaign was funded by several organizations, including NSF, NOAA and NASA. Research institutes such as the University of Illinois at Urbana-Champaign, National Center for Atmospheric Research (NCAR), University of Buenos Aires, University of Washington, Colorado State University, University of Colorado-Boulder, Penn State University, University of Utah, University of Alabama-Huntsville, Pacific Northwest National Laboratory (PNNL) and Center for Severe Weather Research prepared a large group of researchers which included scientists, students, data managers, forecasters, technicians and pilots who came together and set up a dense network of sensors in the Cordoba region. The sensors collected a large amount of data over a long time span, which helped researchers to study and understand convective initiation, upscale growth, and the severe weather from the mesoscale events. The sensors comprised of lightning networks, stationary radars, hail-pads, disdrometers, and several other mobile instruments. Among the stationary radars, the CSU-CHIVO (Colorado State University-C-band Hydro-meteorological Instrument for Volumetric Observation) or simply CHIVO was deployed in the region during the campaign. The next section includes the description of the CHIVO radar and its contribution in the campaign.

Figure 5.3: The CSU-CHIVO radar during the RELAMPAGO campaign [3].

5.3 The CSU-CHIVO radar

The CSU-CHIVO radar was one of the fixed instruments that were installed to collect data continuously. This mainly helped researchers to study the life-cycle of the storms that developed during the period. Fig.5.2 shows the location of the CSU-CHIVO radar deployed near the Alta Gracia region in Argentina during the Relampago campaign. The CHIVO is a C band weather radar with dual-polarization capability and was originally installed at the CSU's Agricultural Research, Development and Education Center (ARDEC) site. It was packed and shipped to the campaign site for deployment. The radar uses a Sigmet Digital Receiver and Vaisala's Sigmet RVP900 Signal Processor that computes products such as reflectivity, velocity, spectral width, differential reflectivity, differential phase, and co-pol correlation coefficient. Various other fields, including specific differential phase, hydrometeor classification index, and rainfall rate, were obtained using the DROPS2 algorithm [36] after data collection. CHIVO's site was located south of Cordoba city, which is about 30 minutes drive from Alta Gracia and 45 minutes drive from Villa Carlos Paz, where the observation center was located. The picture in Fig.5.2 shows the location of different radars that were deployed in the region during the campaign. The ram logo indicates the location of the CSU-CHIVO. The radar symbol in Cordoba city indicates the location of the First Radar Meteorologico Argentino (RMA1). The Atmospheric Research Measurement C-band Scan Precipitation Radar 2 (ARM-CSPR2) was located near Villa Yacanto shown by the ARM symbol. The observation center was located at Villa Carlos Paz, which has been indicated by the Relampago symbol on the map.

The CHIVO radar uses a coaxial magnetron transmitter tube with a solid-state modulator. It operates within the frequency range of 5.5 to 5.7 GHz with a peak power of 250 kilo Watts. Pulse Repetition Frequencies (PRF) range from 50 to 2400 Hz. It operates both in STAR and LDR modes. In the Relampago campaign, the radar mostly operated in the STAR mode. As mentioned before, it uses Vaisala's RVP900 signal processor, which supports azimuth averaging from 2 to 1024 pulses. IIR, fixed and adaptive width clutter filters, including the Gaussian Model Adaptive

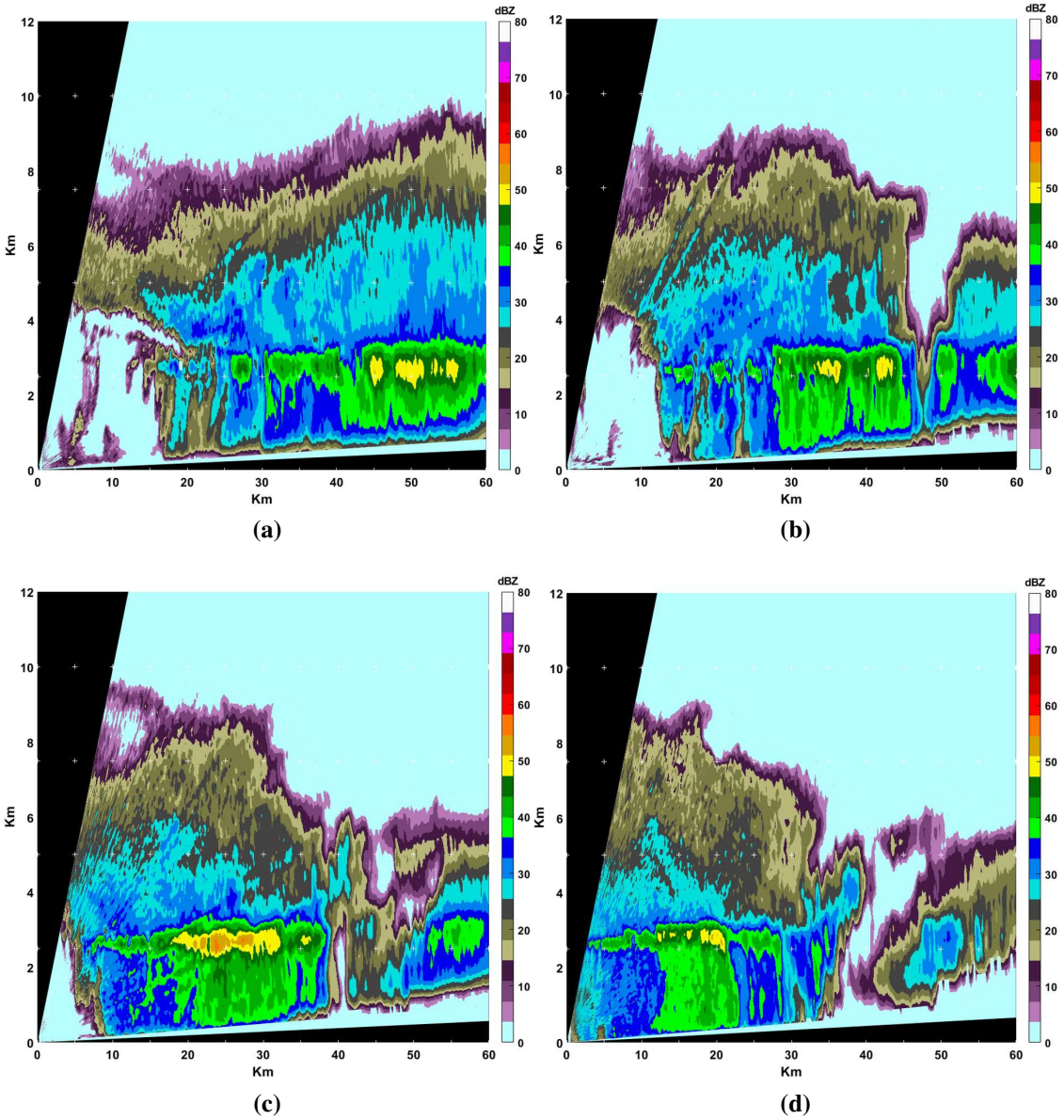

Figure 5.4: Stratiform storms observed by the CSU CHIVO on 30^{th} November 2018 during the IOP in the Relampago campaign.

Processing (GMAP) filter, are also supported by the processor and provide more than 50 dB clutter rejection.

Fig.5.4 shows few of the stratiform storm cases as recorded by the CSU-CHIVO on 30^{th} November 2018. Stratiform conditions are generally steady and are not characterized by turbulent conditions like very strong updrafts and downdrafts. These conditions are close to ideal and nearly follow the theoretical properties of precipitation and can be used to study their general spectral

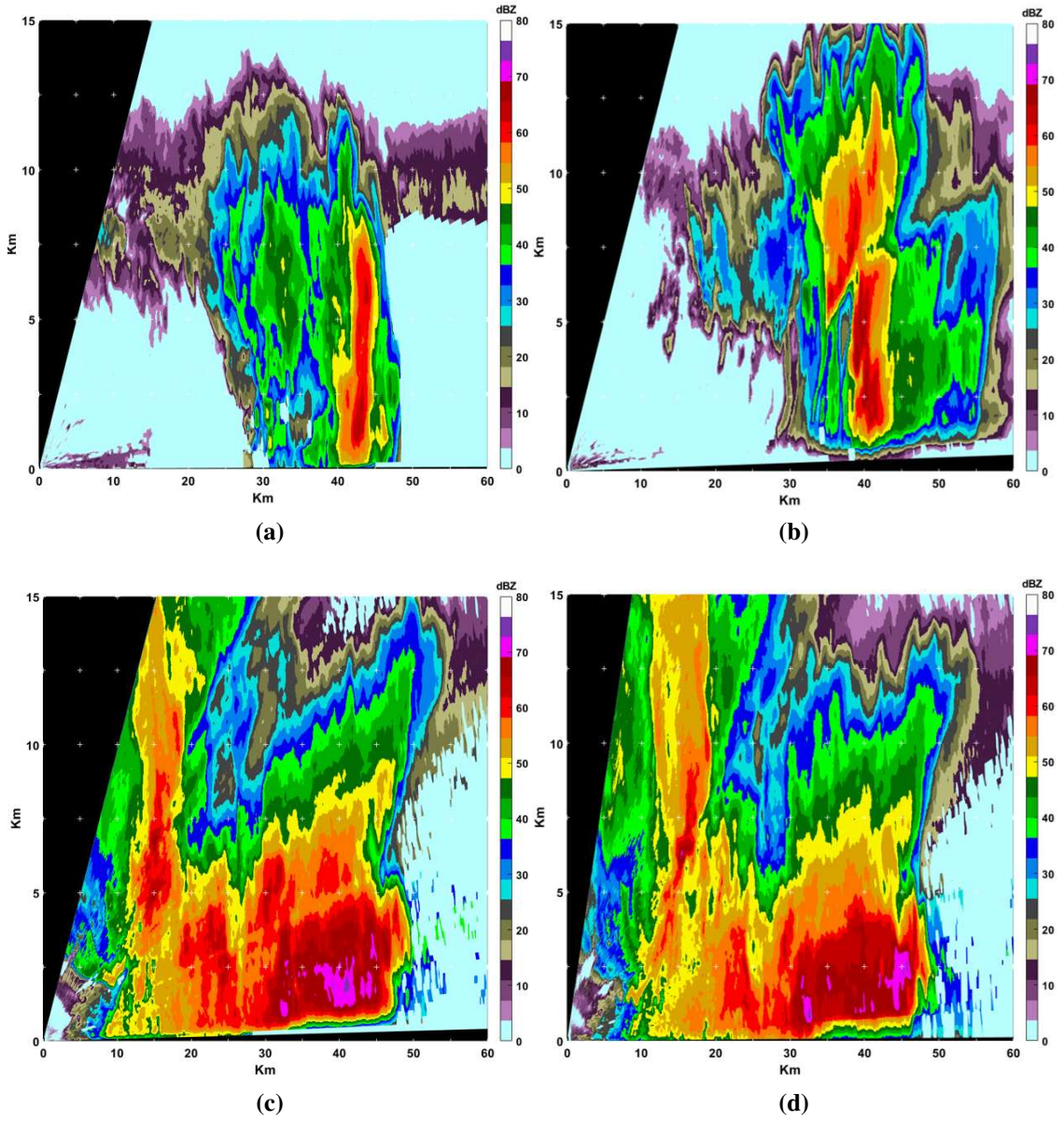

Figure 5.5: Convective storms seen by the CSU CHIVO on 30^{th} November 2018 (A,B) and 25^{th} January 2019 (C,D) during the Relampago campaign.

properties. These properties are studied and reported to provide some basis for comparison when studying the turbulent conditions in convective storms. Fig.5.5 shows a few of the convective storm cases as recorded by the CSU-CHIVO during December 2018 and January 2019. These are convective cells with a very high reflectivity core layer and low co-pol correlation, which indicates hail formation in many cases. They are accompanied by updrafts and downdrafts. Hence, unlike the stratiform cases, they do not have steady conditions, and hence they do not exhibit general spectral

properties. The main goal here is to investigate how the dual-polarization spectral properties in the convective storm cores differ from the steady and ideal conditions.

5.4 Application of Spectral Signal Quality Index

Spectral co-pol correlation spectrum $S(\rho_{hv})$ is generally used for spectral thresholding to suppress background noise and preserve only the precipitation spectrum.

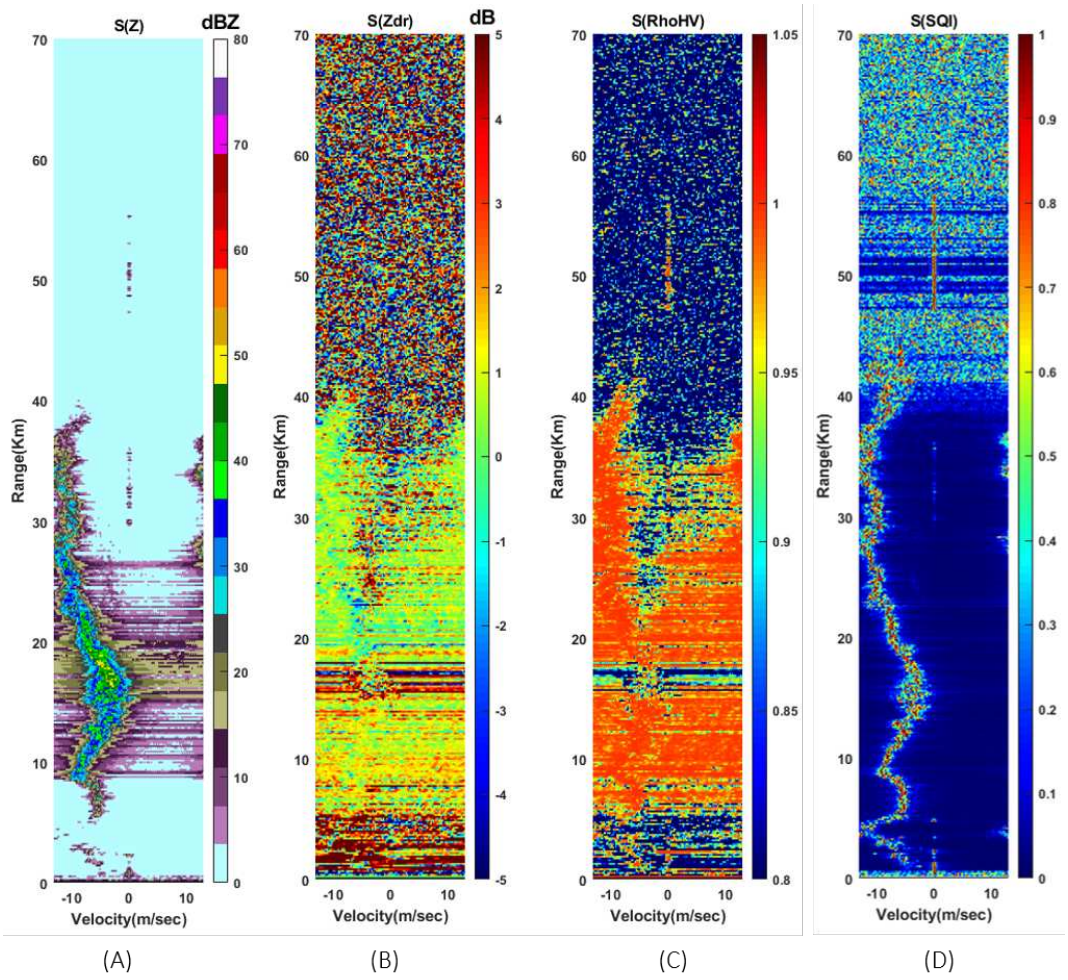

Figure 5.6: Range–Doppler spectrographs of (A) reflectivity $S(Z)$, (B) differential reflectivity $S(Z_{dr})$, (C) Co-pol correlation $S(\rho_{hv})$ and (D) spectral signal quality index $SSQI$ is shown. The spectrographs are calculated from the CSU–CHIVO observations collected on 30^{th} November 2018 during 03:38:33 UTC at an elevation angle of $8.5°$ and at azimuth of $270°$.

Fig.5.6 shows the range-Doppler spectral decomposition of reflectivity, differential reflectivity, and co-pol correlation computed from CSU–CHIVO observations collected on 30^{th} November 2018 at an elevation angle of $8.5°$ and at azimuth of $270°$. As seen from Fig.5.6c it can be observed that the precipitation spectra cannot be distinguished from the background noise. It shows that the spectrum is spread in almost all the Doppler bins. Hence, if this is used for spectral thresholding, the precipitation spectrum cannot be extracted from the background. Fig. 5.7 shows the range-Doppler spectrographs of the dual-polarization variables thresholded using $S(\rho_{hv}) = 0.9$. Therefore this thresholding technique cannot be used in the spectral analysis of precipitation.

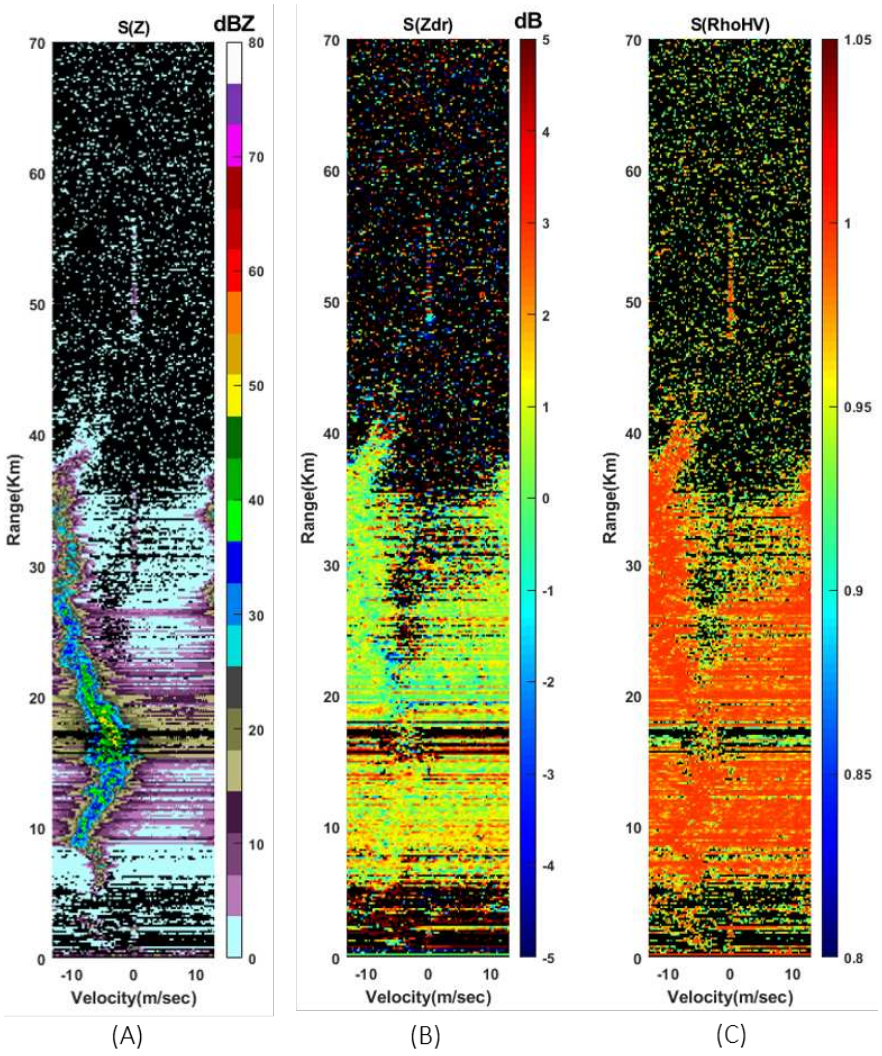

Figure 5.7: Range–Doppler spectrographs of (A) reflectivity $S(Z)$, (B) differential reflectivity $S(Z_{dr})$ and (C) Co-pol correlation $S(\rho_{hv})$ threshold with $S(\rho_{hv}) = 0.9$ done on the same data as shown in Fig. 5.6

The Fig. 5.6c shows the phenomena of spectral leakage and spectral broadening. Generally, $S(\rho_{hv})$ is improved by spectral averaging, which can reduce these effects. Traditionally spectral averaging is done in the following ways:

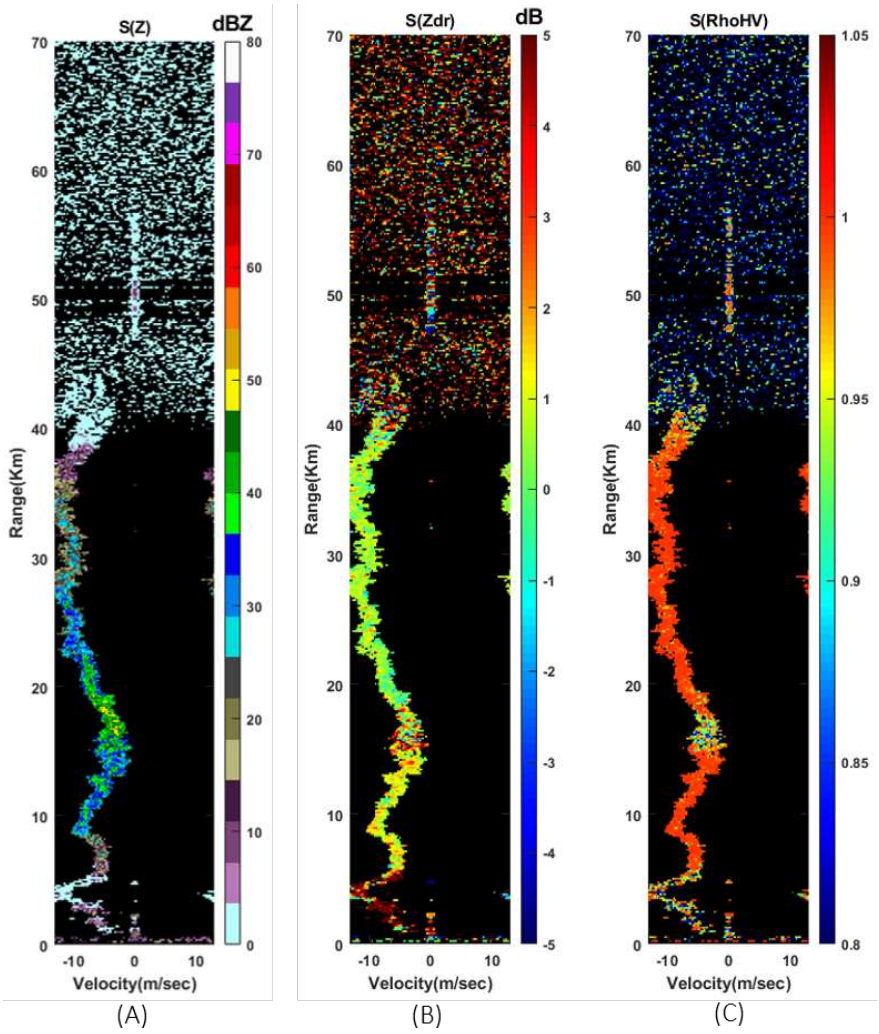

Figure 5.8: Range–Doppler spectrographs of (A) reflectivity $S(Z)$, (B) differential reflectivity $S(Z_{dr})$ and (C) Co-pol correlation $S(\rho_{hv})$ threshold with $SSQI = 0.1$ done on the same data as shown in Fig. 5.6

- Averaging along Doppler bins: If the number of IQ samples is large, then a sliding window of length 64 or 128 can be used to generate multiple spectra and then average them. The resulting spectra are smooth with reduced variance. This is an effective solution for noisy spectra. Generally, for spectral processing and analysis purposes, a 960 or 1024 length IQ

dataset is recorded so that proper spectral averaging can be done. The use of sliding windows is effective on these large datasets so that there is no significant loss in Doppler resolution. However, since the CSU-CHIVO is a fast scanning radar for monitoring rapidly evolving storms, only 64 length data samples were used during observations. Hence this averaging technique cannot be applied on such a small data set.

- Averaging along range: The other option is range averaging along a particular azimuth (in case of PPI scans) or along a particular elevation (in case of RHI scans), but that is avoided as it will reduce the resolution along the range in the spectrographs.

The above two methods will not have a significant improvement on the $S(\rho_{hv})$ field. For these reasons $S(\rho_{hv})$ is not recommended for thresholding. As seen in Fig. 5.6d the Spectral Signal Quality Index presents a clear distinction between the precipitation and the background noise spectrum. Hence this can be used for thresholding. The advantages of using the SSQI field are as follows:

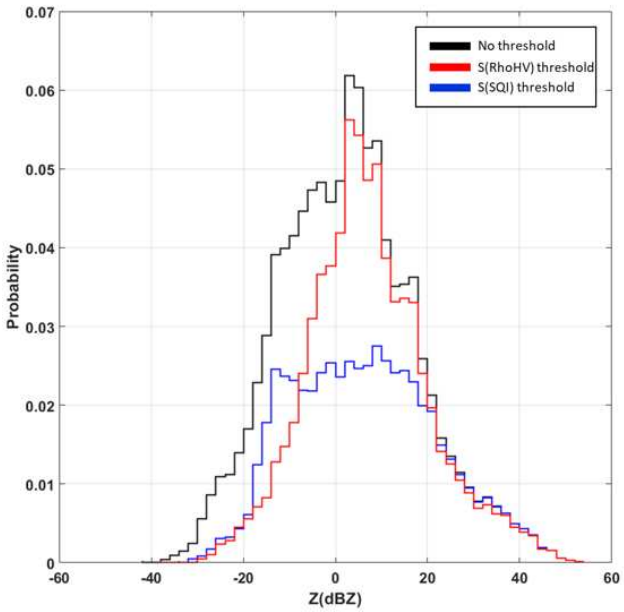

Figure 5.9: Histograms of spectral reflectivity to compare the performances of $S(\rho_{hv})$ and $SSQI$ thresholding based on the spectral decomposition as shown in Fig.5.10

- Data from both H and V polarization channels are not used in the computation of SSQI field. It uses only the ASD computed on the data coming from one of the polarization channels. Hence unlike in the case of $S(\rho_{hv})$ where spectral broadening and leakages are seen, SSQI gives a much clear spectrum.

- In case of melting ice, hail, or mixture of different hydrometeors, the $S(\rho_{hv})$ decreases significantly. Since SSQI depends on signal strength hence its value is consistent.

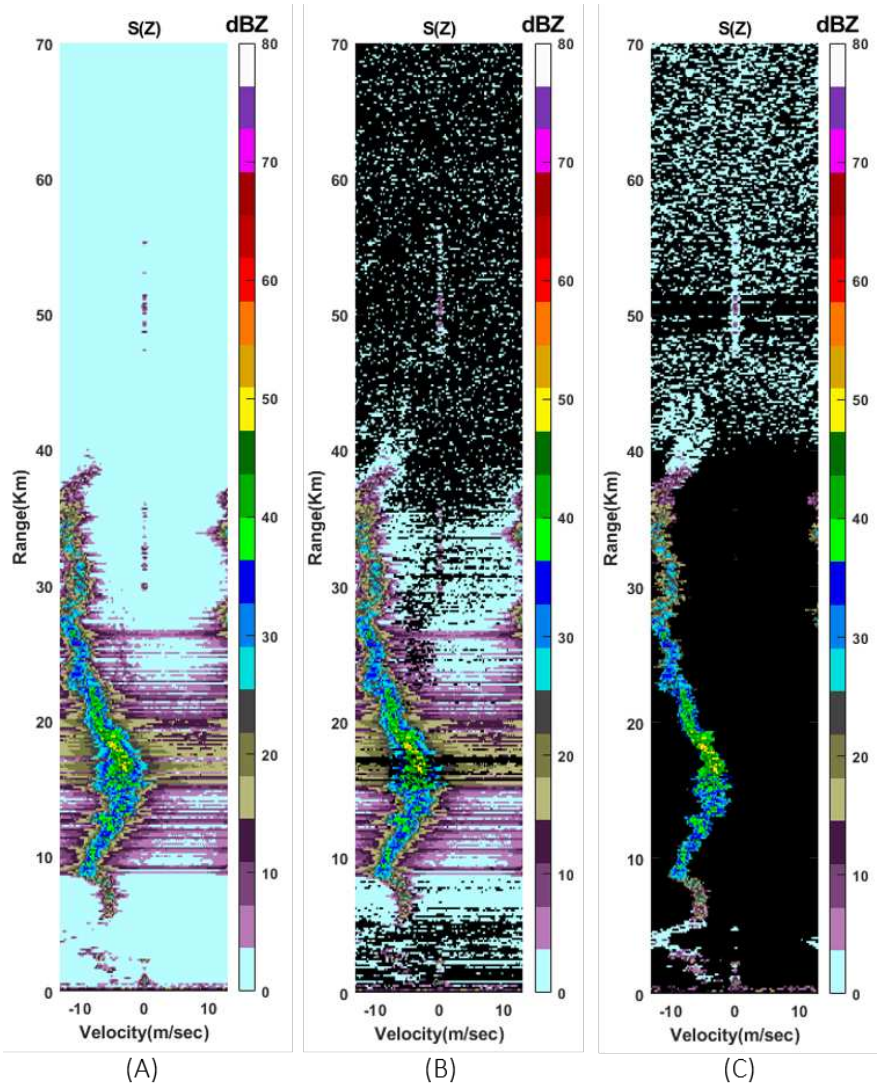

Figure 5.10: The original range-Doppler spectrograph is shown in (A) based on CSU–CHIVO observations collected on 30^{th} November 2018 at an elevation angle of $8.5°$ and at azimuth of $270°$. Comparison of spectral thresholding using $S(\rho_{hv})$ (B) and $SSQI$ (C).

The above two reasons indicate that SSQI can overcome the problem that has been seen in thresholding with $S(\rho_{hv})$. After computation of the SSQI field it has been used for spectral thresholding. Fig. 5.8 shows the range-Doppler spectrographs thresholded with $SSQI = 0.1$. To compare the performances of the thresholding using $S(\rho_{hv})$ and $SSQI$, the histograms of $S(Z_h)$ before and after thresholding are computed and plotted. The background noise or the noise floor mostly contributes towards the values less than 20 dBZ. For a good thresholding parameter the following points are considered:

- The histogram of the thresholded spectrograph with values less than 20 dBZ will have a lower occurrence than the original spectrograph's histogram.
- The higher values which generally are from precipitation spectrum are retained.

5.5 Study of the dual-polarization Doppler spectra from a conventional stratiform rain case

Generally, convective storms are accompanied by significant updraft or downdraft, which causes the mixing of different particles and many other microphysical processes to take place. Hence it is necessary to characterize the dual-polarization spectral properties of these intensive storms. To do this study, we first analyze a stratiform case that exhibits steady rain conditions. This will form a basis for comparing the spectral properties of more complicated phenomena in intensive convective storms. Fig.5.11 shows one of the stratiform cases which was seen during the IOP on 30^{th} November 2018 at 03:37:22 UTC along 223.9° azimuth

Fig. 5.11a shows the H-pol reflectivity of the storm. The maximum reflectivity seen here is around 50 dBZ. The region below 4 km height indicates the occurrence of steady rainfall in this stratiform storm case. These storms move slowly and have an overall steady motion. Fig. 5.11c shows the Co-pol Correlation field for the same scan. The ρ_{HV} values drop below 1 around 2.5 km to 3 km height, which represents the melting layer. The lowering of its value is due to melting ice. This region consists of ice, melting ice, and water. Thus the region is populated with

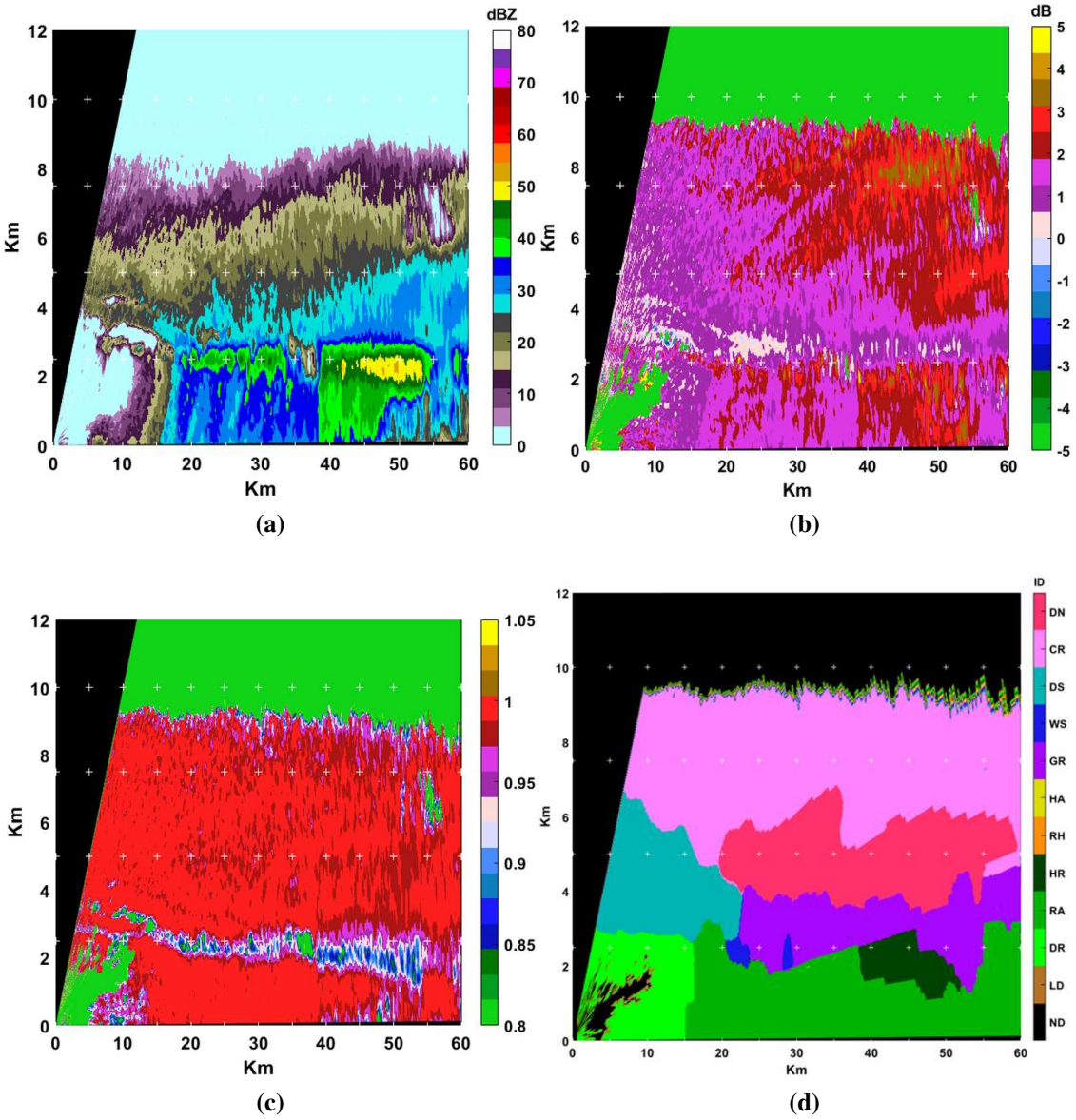

Figure 5.11: Stratiform storm seen by the CSU CHIVO on 30^{th} November 2018 during the IOP in the Relampago campaign recorded at 03:37:22 UTC seen along 223.9° azimuth. The Reflectivity(A), Differential Reflectivity (B), Co-pol Correlation (C) and Hydrometeor Identification Index (D) are shown here.

a mixture of these particles; hence the co-pol correlation coefficient value decreases. Fig. 5.11d shows the hydrometeor classification field, which shows regions with drizzle, rain, heavy rain, and some regions with large drops. Next, the Doppler spectra in these regions are studied, and their properties are observed. The figures are shown in Fig. 5.11 were recorded by the CHIVO on 30^{th} November 2018 at 03:37:22 UTC along 223.9° azimuth. This case will be used to study the

dual-polarization spectra of various rain cases. The case studies done here are all based on this dataset.

- **Rain case**: For the rain case study, we must make sure that we are in the region with steady rain conditions. The HID field in Fig. 5.12b shows the region of interest, which is along $223.9°$ azimuth. The range bin under study is 30 km away from the radar along the ray, which is at $1.3°$ elevation.

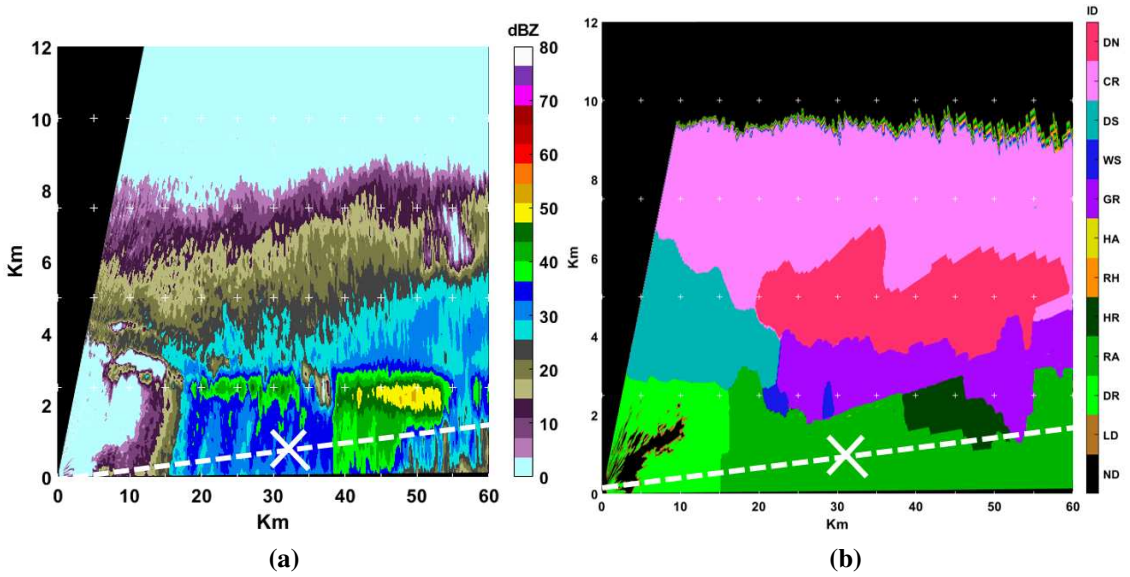

Figure 5.12: RHI scan of a stratiform storm at 03:37:22 UTC seen along $223.9°$ azimuth.(A) and (B) shows Reflectivity and the HID fields respectively. The ray at $1.3°$ elevation is shown in white dotted lines. Spectral analysis is done on the data from the range bin, 30 km away from the radar.

As shown in Fig.5.12 the $1.3°$ elevation ray has been shown in the white dotted line in both the reflectivity and the HID field. The white cross along the ray marks the 30 km range bin from the radar. Spectral decompositions of dual-polarization radar parameters are done on this ray.

This is a uniform region of rain. A narrow $S(Z)$ spectra and an almost uniform $S(\rho_{hv})$ with values close to 1 is expected to be observed in this case. Fig. 5.13 shows the spectral decomposition of reflectivity, differential reflectivity and co-pol correlation. Some ground

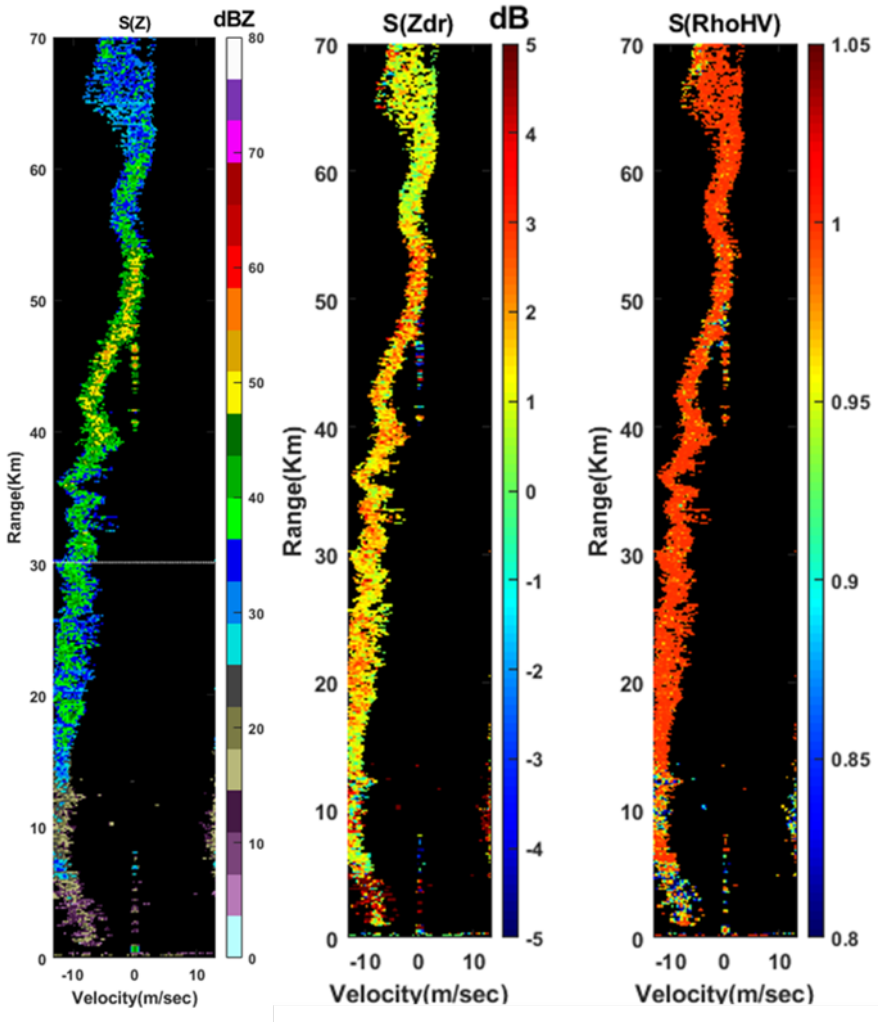

Figure 5.13: Range-Doppler spectral decomposition showing (left to right) $S(Z)$,$S(Z_{dr})$ and $S(\rho_{hv})$ along 1.3° elevation from the data shown in Fig .5.12 for rain case study.

clutter spectrum is observed in the first 10 km from the radar since we are observing the spectra very close to the ground. Some spectra at zero Doppler are also observed in 40 to 50 km away from the radar. This can be due to clutter or stationary particles in the radar resolution volume. The $S(Z)$ ranges from 30 to 50 dBZ . The $S(Z_{dr})$ is close to 0 dB and the $S(\rho_{hv})$ is close to 1 and uniform throughout the ranges except for the first 10 km, which is mostly dominated by clutter. Fig 5.14 shows a cut taken from the spectral decomposition along 30 km from the radar. As seen, the $S(Z)$ spectrum is almost Gaussian, which follows from the fact that in general, the PSD of the weather signal, especially rain, is Gaussian in shape.

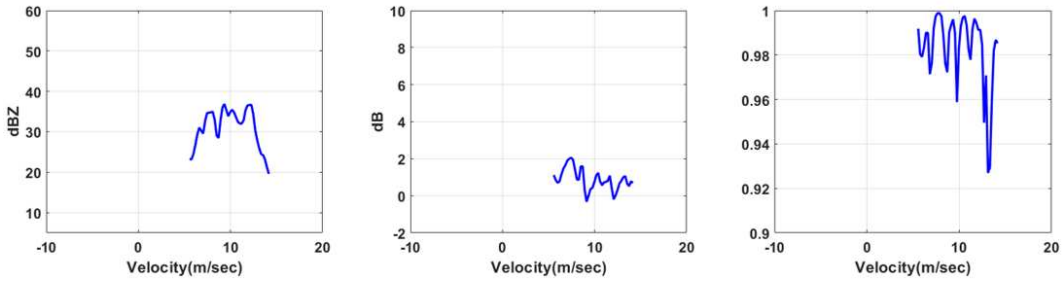

Figure 5.14: Dual polarization spectra as seen at 30 km away from the radar. $S(Z), S(Z_{dr}), S(\rho_{HV})$ are shown from left to right. The location of the spectrums are shown in Fig. 5.13

The $S(Z_{dr})$ is close to 0 with some fluctuations. On average, the Z_{dr} value computed from a resolution volume containing rain is almost 0. This is because rain comprises of almost spherical drops. Since a sphere gives the same power return from both the horizontal and vertical polarization hence the overall Z_{dr} is 0. Also, since the resolution volume contains only rain hence has an overall uniformity of particles therefore the correlation coefficient between the signals from the horizontal and vertical polarization is close to 1. Due to this reason, the $S(\rho_{HV})$ is also high and close to 1 in the region of the rain spectra. All the dual-polarization spectra are computed from 64 sample IQ data collected by the CHIVO radar with 1 ms sampling time period. A Blackman window has been used to reduce spectral leakage and also to obtain a relatively smooth spectrum. A spectral signal quality index ($SSQI$) threshold of 0.1 has been applied on all the dual-polarization spectra to eliminate the noise and preserve the spectra with high precipitation signal content.

- **Heavy rain case**: The region of interest is shown in Fig. 5.15. The HID field in Fig. 5.15b shows that the range bins in the region have been classified as 'HR' or heavy rain by the DROPS2 algorithm [36].

  Fig. 5.15 shows the ray along $2.9°$ elevation with white dotted line. The range gate on which spectral analysis has been done is 45 km away from the radar and marked with the white 'x' mark, as shown in Fig. 5.15b. This range gate is located around 2 km above the ground with a maximum reflectivity close to 50 dBZ. It is located almost near the melting layer. The occurrence of precipitation is directly from the melted ice; thus, the concentration of

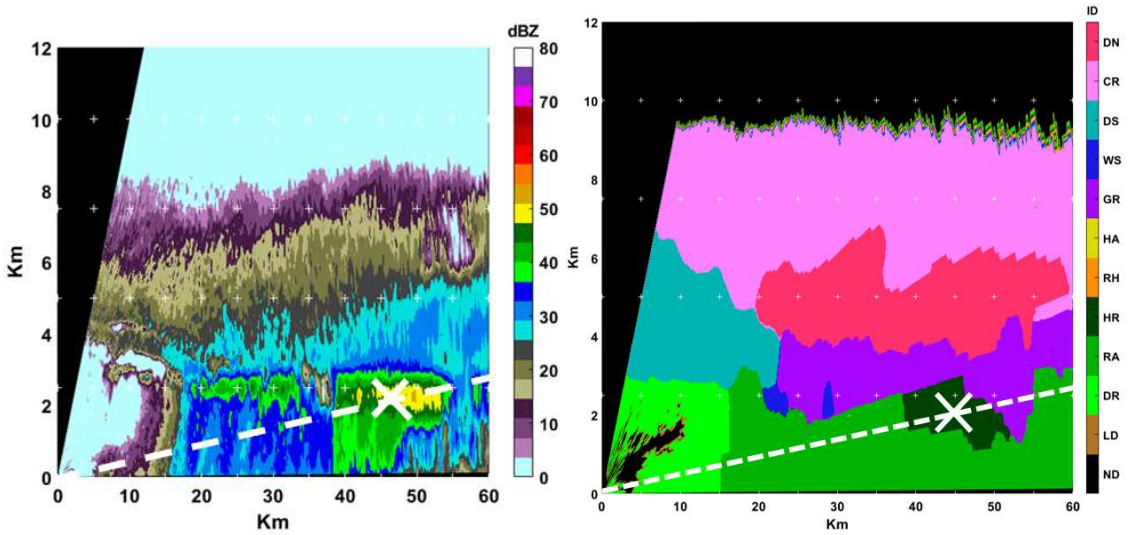

(a) (b)

Figure 5.15: RHI scan of a stratiform storm at 03:37:22 UTC seen along 223.9° azimuth.(A) and (B) shows Reflectivity and the HID fields respectively. The ray at 2.9° elevation is shown in white dotted lines. Spectral analysis is done on the data from the range bin, 45 km away from the radar.

raindrops is very high, and hence the region is classified as heavy rain. Fig. 5.16 shows spectral decomposition at 2.9° elevation. The range gate at 45 km has been shown in the dotted white line in the $S(Z)$ spectrograph. As we go from the rain region (along 12 -40 km) to the heavy rain region (from 40-50 km), we observe an increase of $S(Z)$ values.

The $S(Z)$ has the usual narrow Gaussian characteristics. A trend of negative slope in the $S(Z_{dr})$ is observed. Theoretically, smaller particles have lower differential reflectivity values than larger particles. The heavy rain comprises both very big and small drops, and hence this gives rise to a distribution of $S(Z_{dr})$ values from low to high. Thus in the resolution volume at 45 km range bin consists of both small and big raindrops. This also explains the increase of $S(Z)$ values in the heavy rain region. This non-uniformity of particle size distribution also causes a lowering of the co-pol correlation coefficient, and hence the $S(\rho_{HV})$ spectrum is non-uniform with lower values.

- **Drizzle and rain case**:

  Fig. 5.18 shows the region where spectral analysis has been done in this case.

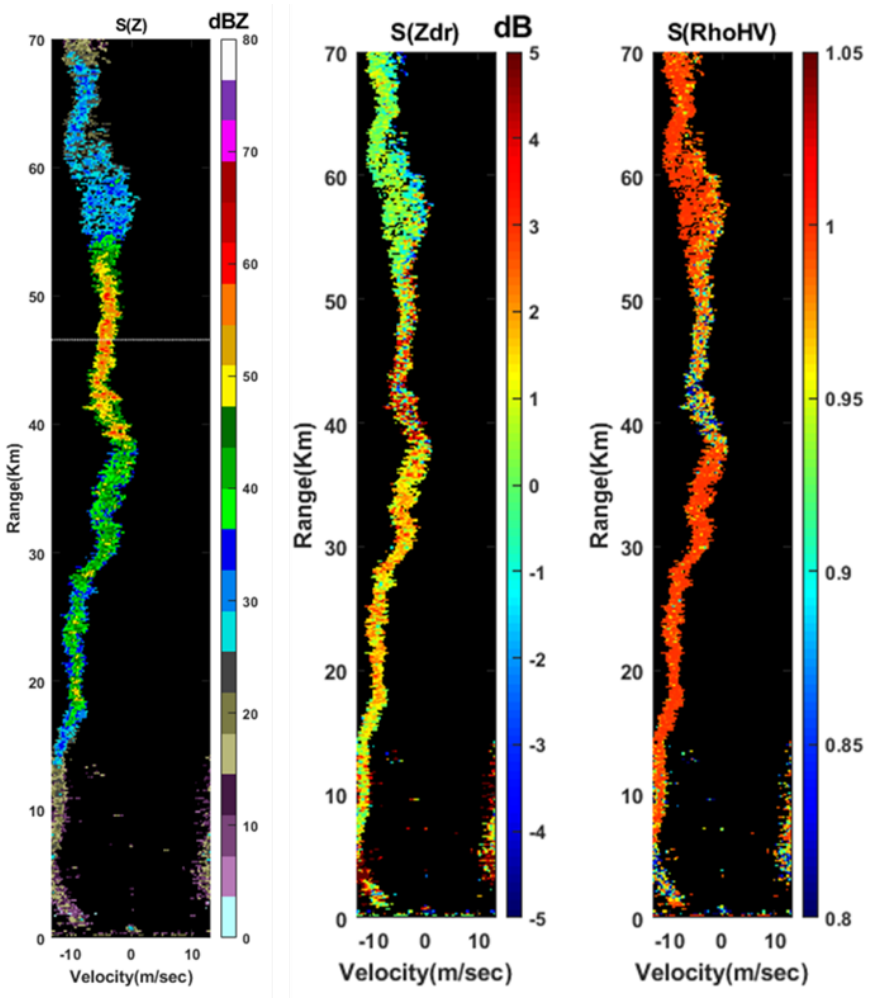

Figure 5.16: Range-Doppler spectral decomposition showing (left to right)$S(Z)$,$S(Z_{dr})$ and $S(\rho_{hv})$ along 2.9° azimuth. The white dotted line shows the 45^{th} km range bin as shown in Fig. 5.15

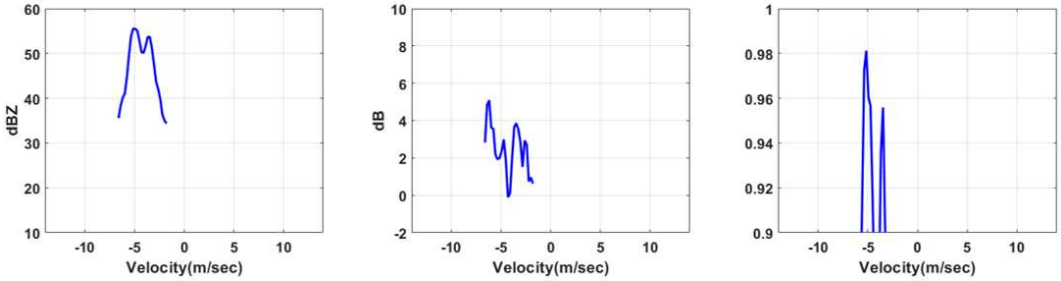

Figure 5.17: (left to right) $S(Z)$,$S(Z_{dr})$ and $S(\rho_{hv})$ at 45 km away from the radar along 2.9° elevation. The location of spectra is as shown in Fig. 5.16

Spectral decomposition is done on the ray along 16.5° elevation shown by the dotted line. The white mark shows the range gate, which is 15 km away from the radar. Fig. 5.19 shows

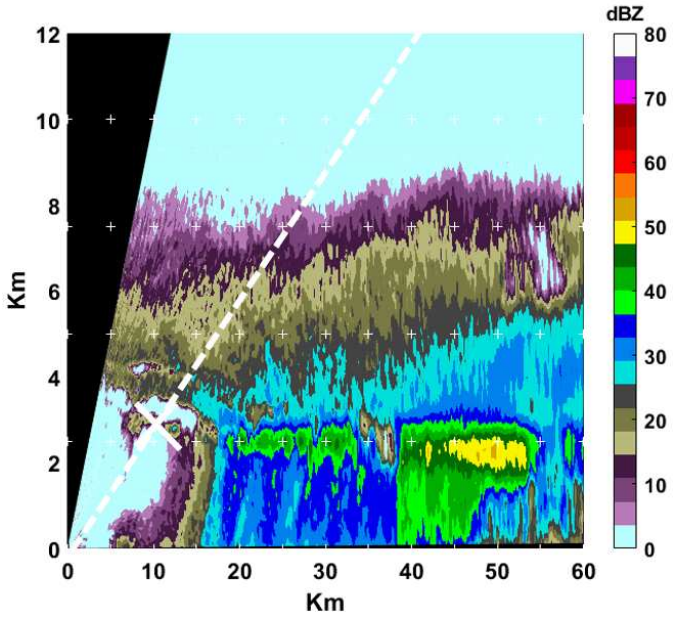

(a) Reflectivity

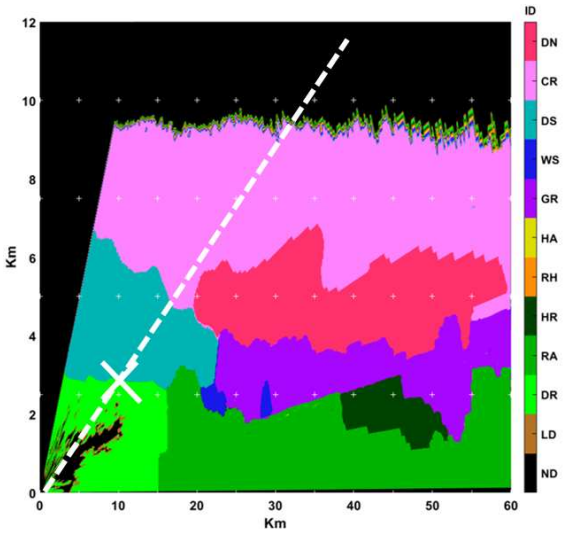

(b) Hydrometeor Classification

Figure 5.18: RHI scan reflectivity showing the area of spectral analysis. The dotted white line shows the $16.5°$ elevation ray and the white mark in the 15 km range bin away from the radar.

spectral decomposition along this ray. Here the region of interest in 15 km away from the radar, which is shown as a white dotted line in the $S(Z)$ spectrograph.

The HID index shows that it is a region of transition from drizzle to rain. The $S(Z)$ spectrograph shows that the spectrum's central Doppler velocity increases from negative to positive as we go along the range from 0 to 15 km. From 15 km it again starts to decrease and takes

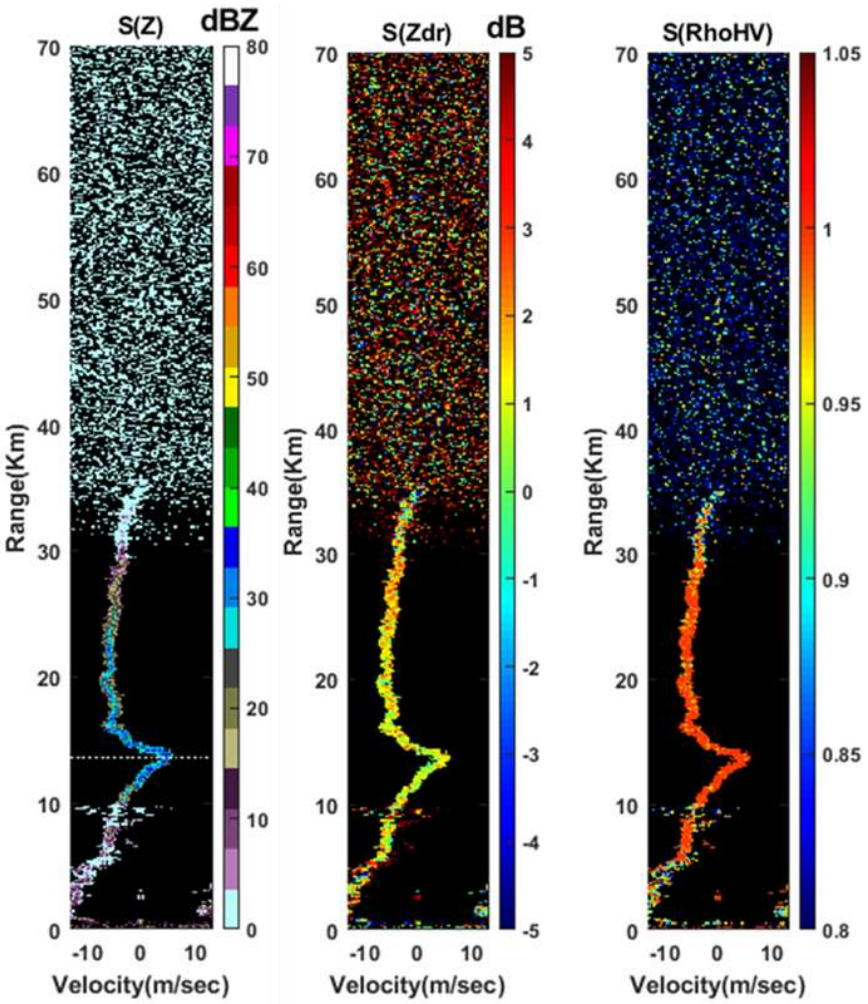

Figure 5.19: Range-Doppler spectral decomposition showing (left to right)$S(Z)$,$S(Z_{dr})$ and $S(\rho_{hv})$ along 16.5° azimuth as shown in Fig.5.18 A

negative value after 17 km. Thus this indicates that the velocity field also changes in this region from negative to positive and then again back to negative. Hence there is a possible movement of the storm towards and away from the radar. At the range gate at 15 km there is a possibility of mixing of drizzle and rain. Thus the resolution volume will be populated with different sizes of raindrops; hence we observe a distribution of values of $S(Z_{dr})$.

The $S(Z)$ has Gaussian characteristics. There is a trend of positive slope in the $S(Z_{dr})$ and is prominent. The slope is because there is a presence of a mixture of rain and drizzle at the boundary. Due to the presence of turbulence, the $S(Z_{dr})$ is spread. The $S(\rho_{hv})$ spectra relatively high. This is due to the presence of the same nature of hydrometeors.

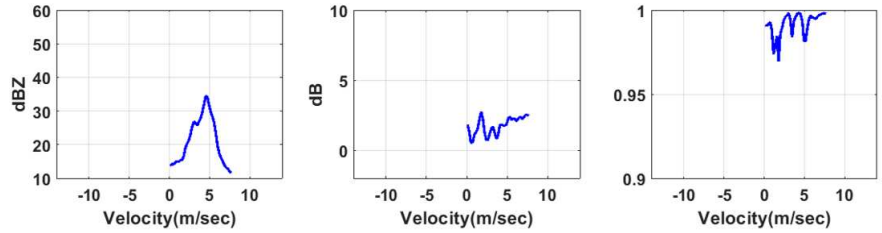

Figure 5.20: left to right) $S(Z)$,$S(Z_{dr})$ and $S(\rho_{hv})$ at 15 km along $23.5°$ azimuth as shown in Fig.5.19

5.6 Study of the dual-polarization Doppler spectra from a turbulent convective storm

In this section, we will analyze different rain and hail cases of convective storms. The data was recorded on 25^{th} January 2019 at 21:09:14 UTC along $282.5°$ azimuth.

- **Rain and Hail case**:

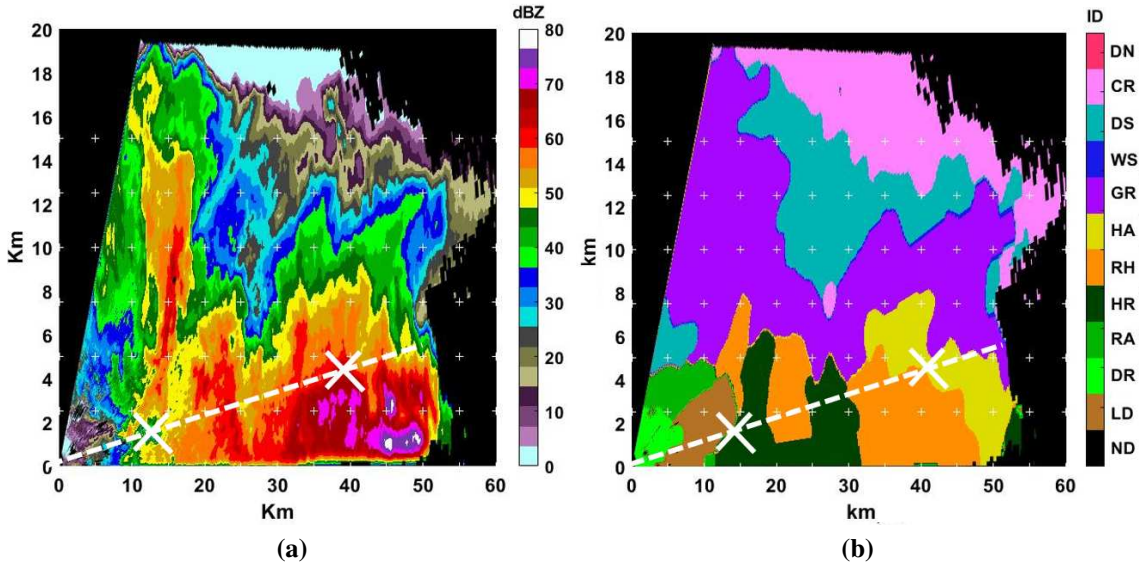

Figure 5.21: RHI scan showing the area of spectral analysis. The dotted white line shows the $6.03°$ elevation ray and the white marks are in the 15 km and 43 km range bins receptively away from the radar.The data was recorded on 25^{th} January 2019 at 21:09:14 UTC along $282.5°$ azimuth.

The analysis is done along $6.03°$ elevation and shown in the white dotted line. The regions for spectral analysis is shown in Fig. 5.21. Here the regions of interest are 15 km and 43

km away from the radar receptively shown in white 'x' marks. The HID index shows that it is a region of heavy rain and hail. The dual-polarization spectra is shown in Fig.5.22. Spectral broadening in $S(Z)$ is observed in both the heavy rain and hail regions. The $S(Z_{dr})$ spectra in hail case shows a negative slope indicating the presence of different hail sizes in the resolution volume.

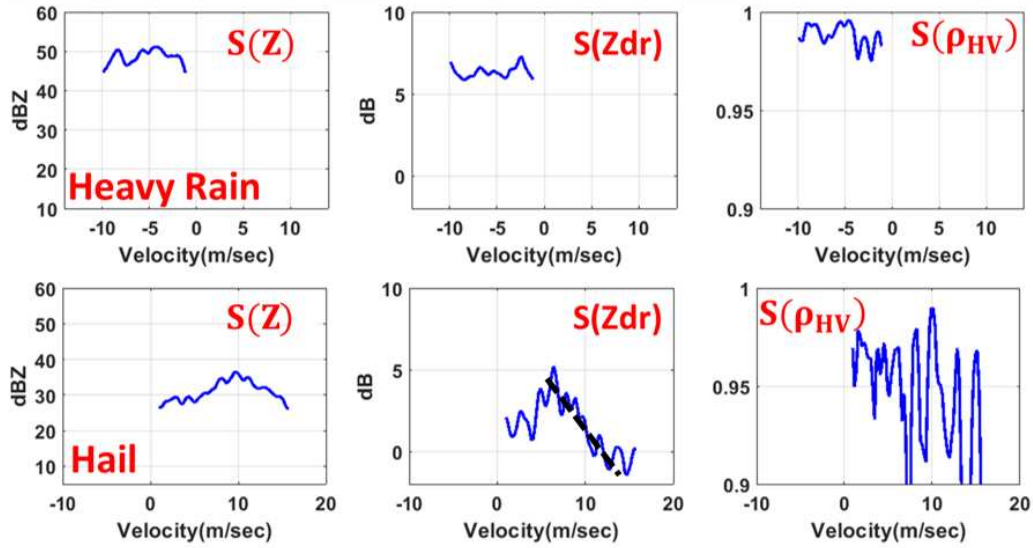

Figure 5.22: Dual-polarization spectra (top left to right) $S(Z)$,$S(Z_{dr})$ and $S(\rho_{hv})$ at 15 km is shown.Bottom left to right) shows $S(Z)$,$S(Z_{dr})$ and $S(\rho_{hv})$ spectra at 43 km along 6.03° elevation

It has a very broad $S(Z)$, unlike the spectra observed in stratiform rain cases. $S(\rho_{hv})$ has low values, which may be due to melting hail or due to the non-uniformity of particle size distribution.

Next, the storm core is studied. It is observed to have a very high reflectivity. The HID field shows that this is a hail core. The white box shows the region of study shown in Fig. 5.23 (A). The core is zoomed in and is shown in Fig. 5.23 (B). Spectral analysis is done on the range gates above the core, at the core, and below the core. The range bins are marked as 1,2, and 3, respectively.

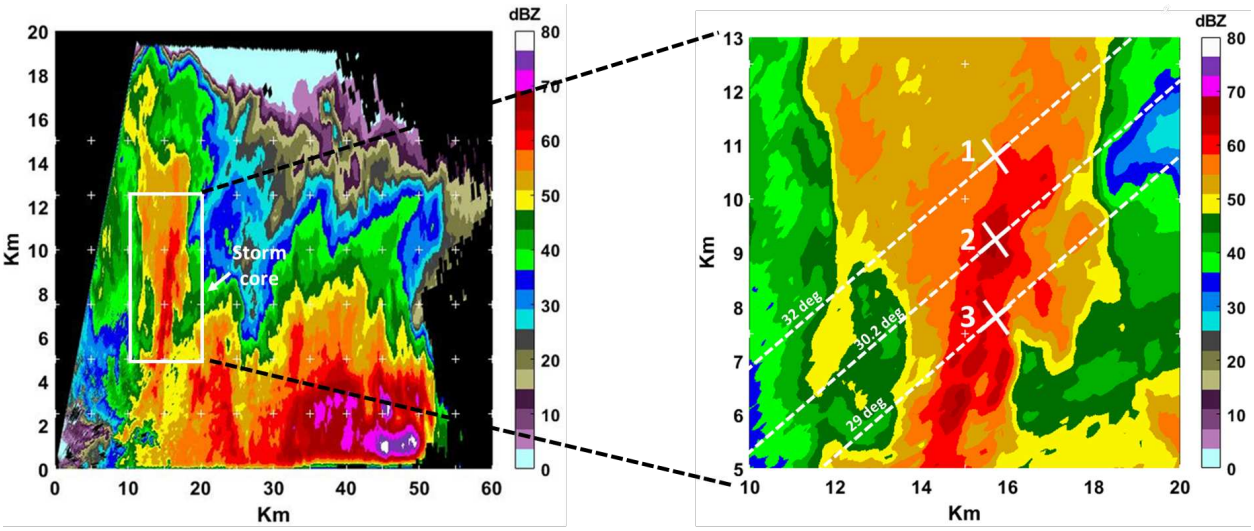

Figure 5.23: RHI scan of convective storm at 21:09:14 UTC seen along 282.5° azimuth recorded on 25^{th} January 2019.(A) and (B) shows Reflectivity and the zoomed in Reflectivity of the storm core respectively.

- **Study above storm core**: Here the region of interest in 18 km away from the radar, as shown by the white dotted lines. The HID index shows that it is a region of snow just above the hail region.

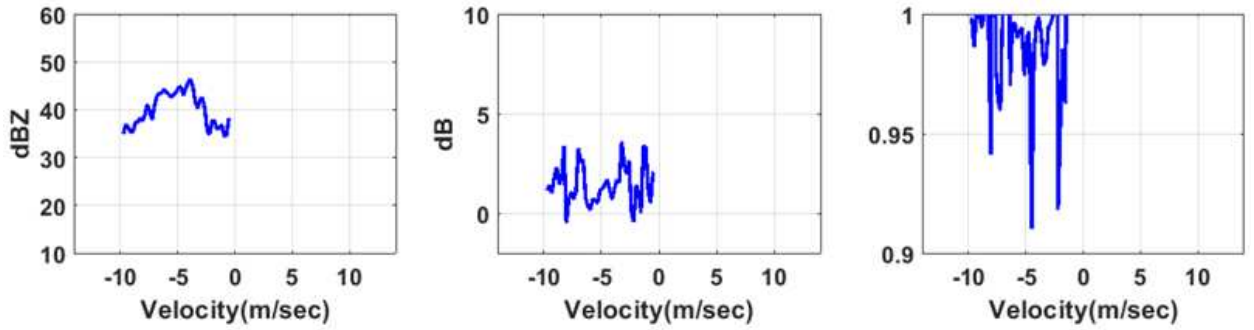

Figure 5.24: (left to right) $S(Z)$,$S(Z_{dr})$ and $S(\rho_{hv})$ at 18 km away from the radar km along 32° azimuth. The location of the spectra are shown in Fig.5.23 (B) marked as region '1'.

As seen, the $S(Z)$ spectrum has a broad spectral width. The $S(Z_{dr})$ is almost all positive, and the $S(\rho_{HV})$ is high, close to 1 in the region indicating the presence of a uniform distribution of particles.

- **Study at storm core**:

  Next, the hail core region is shown. The region for spectral analysis in shown in Fig. 5.23 (B) marked as region '2'. Here the region of interest in 17.5 km away from the radar. The HID index shows that it is a region of hail.

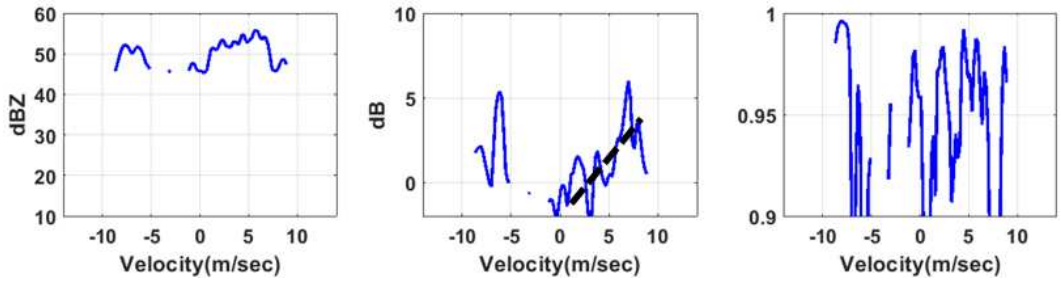

Figure 5.25: Dual-polarization spectra seen at 17.5 km away from the radar.(left to right) $S(Z)$,$S(Z_{dr})$ and $S(\rho_{hv})$ along 30.2° azimuth. The location of the spectra are shown in Fig.5.23 (B) marked as region '2'.

The dual-polarization spectra in Fig.5.25 shows the presence of dual spectra in $S(Z)$. The $S(Z_{dr})$ spectrum shows a positive slope. This is because the updraft pushes liquid or rain from lower elevation upwards, mixing with the hail in this region. Also, due to the strong wind, size sorting occurs; hence we see bi-modality in $S(Z)$ and the slope in the $S(Z_{dr})$ spectrum. The $S(\rho_{HV})$ is low in the region, indicating a non-uniform distribution of particles. This is evident due to the presence of a mixture of rain and hail.

- **Study below storm core**:

  Next, the region just below the hail core is shown. The region for spectral analysis is shown in Fig. 5.23 (B) marked as region '3'. The HID index shows that it is a region of hail. The dual-polarization spectra is shown in Fig.5.26. Spectral broadening is observed in $S(Z)$. The $S(Z_{dr})$ spectrum shows a positive slope. This is because hail from higher elevation falls and mixes with the liquid or rain. Also, due to the strong wind, size sorting occurs; hence we see the slope in the $S(Z_{dr})$ spectrum.

  The $S(\rho_{HV})$ is low in the region, indicating a non-uniform distribution of particles. This is evident due to the presence of a mixture of rain and hail.

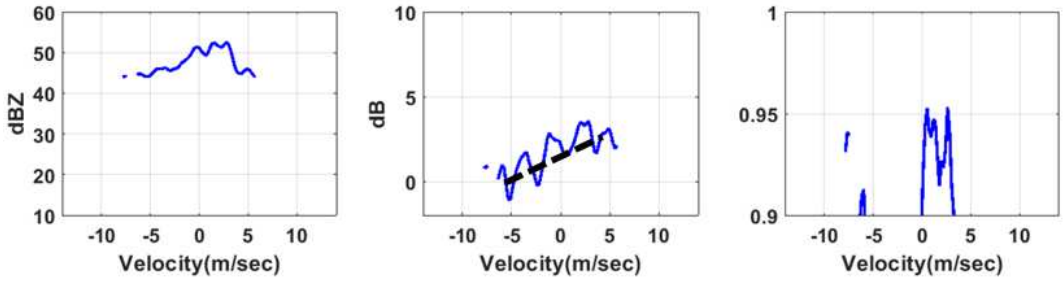

Figure 5.26: Dual-polarization Doppler spectra (left to right) $S(Z)$,$S(Z_{dr})$ and $S(\rho_{hv})$ at 16.5 km along 29° azimuth. The location of the spectra are shown in Fig.5.23 (B) marked as region '3'.

5.7 Conclusion

Hydrometeor classification algorithm performed on the radar data showed the presence of different types of hydrometeors, including rain, hail, large drops, mixture of rain and hail, snow, graupel, and dendrites. Spectral analysis was done at different range bins, and the properties are reported. Spectral broadening and bi-modal spectra are observed in $S(Z)$. Slopes in $S(Z_{DR})$ indicates size sorting, which occurs due to strong vertical wind motion. Hence, spectral polarimetry can be used to characterize the dynamics of a storm at a particular radar resolution volume. Spectral properties reveal essential information about the microphysics of a storm observed by dual-polarization weather radar.

Chapter 6

Summary

6.1 Discussion

This research's primary focus is to mitigate sea clutter using spectral filtering and study rain and hail from intense storms using spectral polarimetry. The CSU-SEAPOL radar is a dual-polarized parametric Doppler radar that was developed to be deployed on ships in different campaigns on different water bodies in various parts of the world. The main goal of the radar is to provide precipitation observations to the researcher onboard the vessel. Once they find their region of interest, the vessel is guided in those locations where they carry out their experiments. Radar observations have errors and biases, which may lead to wrong decisions by meteorologists and forecasters; hence it is imperative to reduce them. When the radar scans at low elevation to observe rain at the sea surface, the reflections from the sea surface, also known as sea clutter, produce bias in the radar moments and dual-pol variables. Hence sea clutter mitigation is a significant problem.

Traditionally, in filtering methods like standard notch filters, GMAP and PTDM, the filtered time series is estimated from the filtered spectra, which is used in estimating radar moments using the pulse-pair processing. The moments can also be directly computed from the filtered spectra; this is regarded as spectral processing. Precipitation spectrum can be obtained by applying spectral filters, which can suppress clutter and noise components. Next, the radar moments and variables are estimated directly from the filtered and thresholded spectra using spectral processing. Hence spectral processing has become an essential algorithm in the weather radar community.

In Chapter 2 the pulse-pair processing and the spectral processing algorithms are discussed. In Chapter 3, the existing spectral filtering algorithms are implemented for sea clutter mitigation. Firstly the standard notch filter has been implemented. Traditionally this filter has been used by the WSR-88D operational radars for ground clutter mitigation with a fixed clutter map. Three different clutter widths are used depending on the strength of the clutter. Since, in the case of sea

clutter, it is impossible to construct a fixed clutter map due to its uncertain nature, hence for every scan, the sea clutter contaminated ranges bins are identified using fuzzy logic approach. Now since sea clutter spectra may not occur precisely at zero Doppler unlike ground clutter, hence once the filters are applied, they do not successfully suppress sea clutter from all the contaminated range bins. Next, the Gaussian Model Adaptive Processing (GMAP) is implemented. It this case, we do not require any clutter map since the decision of filtering is made from the Clutter to Signal Ratio value computed from the spectrum at each range bin. This filter also was initially used for ground clutter mitigation where the central five Doppler bins are removed, and a Gaussian spectrum is fitted to retrieve the missing values in the spectra. Since there is no limit to the notch width, a wider width can be used where the clutter occurs very close to the zero Doppler. Hence GMAP performs better than the notch filter due to its adaptive nature of identifying clutter bins. Next, a Parametric Time Domain Model is implemented to estimate the mean power, velocity, and spectral width of precipitation and clutter. In the original PDTM algorithm, the mean Doppler velocity for the initialization of the parameter estimation process was assumed to be zero since it was designed for ground clutter. In this case, we do not make such assumptions and directly perform a two echo test and separately estimate the precipitation and sea clutter parameters. This is observed to have the best performance among all the three filtering algorithms.

In Chapter 4 using the Auto-Correlation Spectral Density, a thresholding quantity known as Spectral Signal Quality Index, which is the Fourier domain equivalent of the Spectral Quality Index in the time domain has been discussed. Using the clutter spectral parameters estimated from the PTDM algorithm along with the SSQI threshold, precipitation, sea clutter, and noise Doppler bins are identified. This combined filtering methodology is regarded as Advanced Spectral Filter (ASF). Next, a precipitation mask is constructed, which is used to estimate radar moments and variables from the dual-polarization spectra. Following this, the performances of all the filtering algorithms are compared. ASF is observed to have the best performance among all the clutter filters implemented.

In Chapter 5, the CSU-CHIVO radar and its contribution to the Relampago campaign has been

discussed. This chapter's primary focus is to study the dual-polarization spectra of rain and hail in intense convective storms. Firstly, the general properties of rain spectra in steady conditions i.e., stratiform cases, are studied. Next, a convective case with a hail core is studied. Different dual-polarization spectral properties like bi-modal power spectra, slope in differential reflectivity spectra, lowering of co-pol correlation spectra, etc. helped in the conclusion of different storm dynamics and micro-physics in a particular radar resolution volume. It is finally concluded that intense micro-physical properties of storms can be characterized using spectral polarimetry.

6.2 Suggestions for future work

In the case of the SEAPOL radar, it is essential to find a method for automatic detection of sea clutter, which can be implemented in real-time. The main challenge here is that since it is a fast scanning radar, it collects very few samples at a particular time instance, which is not enough for the automatic detection process. This problem needs to be addressed in future work. It has been concluded in the thesis that the adaptive spectral filter has the best performance in the sea-clutter mitigation, but in this case, the filtered time-series signal cannot be obtained because, after thresholding, we lose parts of irrelevant data hence the reconstruction from the spectral domain was not done. This is another problem that needs to be addressed in future research.

In the case of the Relampago data set, it has been established that spectral polarimetry can be used to characterize intense convective storms and characterize different micro-physical properties of the events associated with them. The next step is to study the complete life cycle of different storms and investigate if some new physical properties can be derived from the study. This will help researchers understand the factors and properties of a storm to develop, grow, and finally decay.

Bibliography

[1] Dmitri N. Moisseev and V. Chandrasekar. Polarimetric spectral filter for adaptive clutter and noise suppression. *Journal of Atmospheric and Oceanic Technology*, 26(2):215–228, 2009.

[2] Adam Varble. Relampago-cacti workshop all about the data, November 2019. https://www.arm.gov/news/blog/post/59580.

[3] I. Arias, V. Chandrasekar, and S. S. Joshil. Cross-validation of csu-chivo radar and gpm during relampago. In *IGARSS 2019 - 2019 IEEE International Geoscience and Remote Sensing Symposium*, pages 7586–7589, 2019.

[4] AD Siggia and RE Passarelli. Gaussian model adaptive processing (gmap) for improved ground clutter cancellation and moment calculation. In *Proc. European Conf. on Radar in Meteorology and Hydrology, ERAD*, volume 2, pages 421–424, 2004.

[5] Yadong Wang, Tian-You Yu, Alexander V. Ryzhkov, and Matthew R. Kumjian. Application of spectral polarimetry to a hailstorm at low elevation angle. *Journal of Atmospheric and Oceanic Technology*, 36(4):567–583, 2019.

[6] L. Pfitzenmaier, C. M. H. Unal, Y. Dufournet, and H. W. J. Russchenberg. Observing ice particle growth along fall streaks in mixed-phase clouds using spectral polarimetric radar data. *Atmospheric Chemistry and Physics*, 18(11):7843–7862, 2018.

[7] Cuong M. Nguyen, Dmitri N. Moisseev, and V. Chandrasekar. A parametric time domain method for spectral moment estimation and clutter mitigation for weather radars. *Journal of Atmospheric and Oceanic Technology*, 25(1):83–92, 2008.

[8] Dmitri N. Moisseev and V. Chandrasekar. Polarimetric spectral filter for adaptive clutter and noise suppression. *Journal of Atmospheric and Oceanic Technology*, 26(2):215–228, 2009.

[9] Vaisala, RVP900 Digital Receiver and Signal Processor. User's Manual, M211322EN-D,Vaisala Oyj, 2017. ftp://ftp.sigmet.com/outgoing/manuals/RVP900_Users_Manual.pdf.

[10] V. N. Bringi and V. Chandrasekar. *Polarimetric Doppler Weather Radar: Principles and Applications*. Cambridge University Press, 2001.

[11] Richard J. Doviak and Dušan S. Zrnić. 5 - doppler spectra of weather signals. In Richard J. Doviak and Dušan S. Zrnić, editors, *Doppler Radar and Weather Observations (Second Edition)*, pages 87 – 121. Academic Press, San Diego, second edition edition, 1993.

[12] Alan Bole, Alan Wall, and Andy Norris. Chapter 3 - target detection. In Alan Bole, Alan Wall, and Andy Norris, editors, *Radar and ARPA Manual (Third Edition)*, pages 139 – 213. Butterworth-Heinemann, Oxford, third edition edition, 2014.

[13] M. I. Skolnik. *Introduction to Radar Systems /2nd Edition/*. McGraw Hill Book Co., New York, 2 edition, 1980.

[14] S. Watts, K. D. Ward, and R. J. A. Tough. The physics and modelling of discrete spikes in radar sea clutter. In *IEEE International Radar Conference, 2005.*, pages 72–77, 2005.

[15] K. D. Ward, C. J. Baker, and S. Watts. Maritime surveillance radar. i. radar scattering from the ocean surface. *IEE Proceedings F - Radar and Signal Processing*, 137(2):51–62, 1990.

[16] S. Haykin, R. Bakker, and B. W. Currie. Uncovering nonlinear dynamics-the case study of sea clutter. *Proceedings of the IEEE*, 90(5):860–881, 2002.

[17] S. P. Sira, D. Cochran, A. Papandreou-Suppappola, D. Morrell, W. Moran, S. D. Howard, and R. Calderbank. Adaptive waveform design for improved detection of low-rcs targets in heavy sea clutter. *IEEE Journal of Selected Topics in Signal Processing*, 1(1):56–66, 2007.

[18] K. D. Ward, R. J. A. Tough, and S. Watts. Sea clutter: Scattering, the k distribution and radar performance. *Waves in Random and Complex Media*, 17(2):233–234, 2007.

[19] D. Walker. Doppler modelling of radar sea clutter. *IEE Proceedings - Radar, Sonar and Navigation*, 148(2):73–80, 2001.

[20] D. Walker. Experimentally motivated model for low grazing angle radar doppler spectra of the sea surface. *IEE Proceedings - Radar, Sonar and Navigation*, 147(3):114–120, 2000.

[21] Vinnie Chanthavong, Joe Holmes, Reino Keränen, Doug Paris, Jason Selzler, Alan Siggia, Toni Stordell, and Reino Keränen. Mitigation of sea clutter and other non-stationary echoes based on general purpose polarimetric echo identification. In *Sixth European Conf. on Radar in Meteorology and Hydrology, ERAD, Sibiu, Romania*, 2010.

[22] K. Hannesen and A. Weipert. A probability-based sea clutter suppression method for polarimetrie weather radar systems. *IAHS-AISH Publication*, 351:52–57, 01 2012.

[23] J. George, V. Chandrasekar, F. Junyent, S. A. Rutledge, A. Morin, R. Bowie, and P. Kennedy. Salient features of the csu sea-pol radar. In *2018 IEEE Radar Conference (RadarConf18)*, pages 1307–1310, April 2018.

[24] Steven A. Rutledge, V. Chandrasekar, Brody Fuchs, Jim George, Francesc Junyent, Patrick Kennedy, and Brenda Dolan. Deployment of the sea-pol c-band polarimetric radar to spurs-2. *Oceanography*, 32, June 2019.

[25] Alexander Ryzhkov, Pengfei Zhang, Richard Doviak, and Cathy Kessinger. Discrimination between weather and sea clutter using doppler and dual-polarization weather radars. *Proc. 27th General Assembly of the International Union of Radio Science*, 3, 2002.

[26] W. Hailong, D. Shouyuan, W. Xu, and S. Zhao. Sea clutter recognition based on dual-polarization weather radar. In *2019 International Conference on Meteorology Observations (ICMO)*, pages 1–3, 2019.

[27] T. W. Parks and C. S. Burrus. *Digital Filter Design*. Wiley-Interscience, USA, 1987.

[28] Ann Marie Raynal and Armin Walter Doerry. Doppler characteristics of sea clutter. *Sandia Report (SAND2010-3828); Sandia National Laboratories: Alburquerque, NM, USA*, June 2010.

[29] Christine Unal. Spectral polarimetric radar clutter suppression to enhance atmospheric echoes. *Journal of Atmospheric and Oceanic Technology*, 26(9):1781–1797, 2009.

[30] J. Yin, C. M. H. Unal, and H. W. J. Russchenberg. Narrow-band clutter mitigation in spectral polarimetric weather radar. *IEEE Transactions on Geoscience and Remote Sensing*, 55(8):4655–4667, Aug 2017.

[31] L. Alku, D. Moisseev, T. Aittomäki, and V. Chandrasekar. Identification and suppression of nonmeteorological echoes using spectral polarimetric processing. *IEEE Transactions on Geoscience and Remote Sensing*, 53(7):3628–3638, July 2015.

[32] Hongping Liu and V. Chandrasekar. Classification of hydrometeors based on polarimetric radar measurements: Development of fuzzy logic and neuro-fuzzy systems, and in situ verification. *Journal of Atmospheric and Oceanic Technology*, 17(2):140–164, 2000.

[33] S. Lim, V. Chandrasekar, and V. N. Bringi. Hydrometeor classification system using dual-polarization radar measurements: model improvements and in situ verification. *IEEE Transactions on Geoscience and Remote Sensing*, 43(4):792–801, April 2005.

[34] D. A. Warde and S. M. Torres. The autocorrelation spectral density for doppler-weather-radar signal analysis. *IEEE Transactions on Geoscience and Remote Sensing*, 52(1):508–518, 2014.

[35] Yadong Wang, Tian-You Yu, Alexander V. Ryzhkov, and Matthew R. Kumjian. Application of Spectral Polarimetry to a Hailstorm at Low Elevation Angle. *Journal of Atmospheric and Oceanic Technology*, 36(4):567–583, 04 2019.

[36] Renzo Bechini and V. Chandrasekar. A semisupervised robust hydrometeor classification method for dual-polarization radar applications. *Journal of Atmospheric and Oceanic Technology*, 32(1):22–47, 2015.

Appendix A

List of Abbreviations

Z - Reflectivity; Unit - dBZ (decibel relative to Z)

Z_{DR} - Differntial Reflectivity; Unit- dB (decibel)

ρ_{HV} - Copol Correlation

ϕ_{DP} - Differential Phase; Unit- degree

IFDR - Intermediate Frequency Digital Receiver

SEAPOL - SEA-going POL-arimetric

SPURS - Salinity Processes in the Upper Ocean Regional Study

STSR - Simultaneous Transmit Simultaneous Receive

CSU-CHILL - Colorado State University-Chicago Illinois

PPI - Plan Position Indicator

RHI - Range Height Indicator

PTDMParametric Time-Domain Method

SQI - Signal Quality Index

SSQI - Spectral Signal Quality Index

GMAP - Gaussian Model Adaptive Processing

ASF - Advanced Spectral Filter

RFI - Radio Frequency Interference

I,Q - In-phase, Quadrature-phase

DFT - Discrete Fourier Transform

H-pol - Horizontal polarization

V-pol - Vertical polarization

PSD - Power Spectral Density

ASD - Auto Spectral Density

C - Radar Constant

WSR-88D - Weather Surveillance Radar, 1988, Doppler

CSR - Clutter to Signal Ratio

SNR - Signal to Noise Ratio

MLE - Minimum Likelihood Estimate

IOP - Intensive Observing Period

EHOP - Extended Hydro-meteorology Observing Period

DROPS - Dual-Polarization Radar Operational Processing System

RELAMPAGO - Remote Sensing Of Electrification, Lightning, And Mesoscale/Microscale Processes With Adaptive Ground Observations

HID - Hydrometeor Identification Index